Analysis of W and Z Production at $\sqrt{s} = 7$ TeV with the CMS Detector

von

Andreas Güth

Diplomarbeit in Physik

vorgelegt der

Fakultät für Mathematik, Informatik und Naturwissenschaften
der Rheinisch-Westfälischen Technischen Hochschule Aachen

im Mai 2011

angefertigt im

III. Physikalischen Institut A
Prof. Dr. Thomas Hebbeker

Zweitgutachter

Prof. Dr. Christopher Wiebusch

Zusammenfassung

Das Verständnis der Produktion von W und Z Bosonen ist ein wichtiger Prüfstein während der Inbetriebnahme eines Hadronenbeschleunigers. Aufgrund ihrer großen Produktionswirkungsquerschnitte und klaren Signaturen dienen Ereignisse mit W und Z Bosonen einerseits als Test des Standard-Modells in einer frühen Phase der Datennahme. Andererseits können sie zur Untersuchung von Detektorfunktionen und der Simulation herangezogen werden.
Diese Arbeit befasst sich mit der inklusiven Produktion von W und Z Bosonen im myonischen Zerfallskanal mit einen Datenmenge von 36 pb^{-1}, die 2010 mit dem CMS Detektor am LHC in Proton-Proton Kollisionen bei einer Schwerpunktsenergie von $\sqrt{s} = 7$ TeV aufgezeichnet worden ist. Für die Bestimmung von Myoneffizienzen, Untergründen und der hadronischen Energie in W und Z Ereignissen werden datengestützte Analysetechniken genutzt. Die Messung des inklusiven Produktionswirkungsquerschnitts für W Bosonen im myonischen Zerfallskanal ergibt
9.97 ± 0.03 (stat) ± 0.28 (syst) ± 0.40 (lumi) nb und das Verhältnis der Wirkungsquerschnitte in Abhängigkeit von der elektrischen Ladung W^+/W^- beträgt 1.44 ± 0.01 (stat) ± 0.03 (syst). Das Resultat für den inklusiven Produktionswirkungsquerschnitt für Z/γ^* Bosonen im myonischen Zerfallskanal, eingeschränkt auf eine invarinate Masse von 60 GeV $< M_{\mu\mu} <$ 120 GeV, lautet
0.955 ± 0.009 (stat) ± 0.023 (syst) ± 0.038 (lumi) nb. Es folgt ein Verhältnis der Wirkungsquerschnitte für W und Z/γ^* Produktion von 10.44 ± 0.10 (stat) ± 0.30 (syst). Die Resultate stimmen mit theoretischen Berechnungen im Rahmen des Standard-Modells überein.
Die Masse des W Bosons ist ein wichtiger Parameter für Konsistenztests des Standard-Modells. Sie wird in dieser Arbeit zu 80.43 ± 0.05 (stat) $\pm$ 0.13 (syst) GeV bestimmt, in Übereinstimmung mit präziseren Messungen, welche den Weltmittelwert festlegen.

Abstract

The production of W and Z bosons is a benchmark at the startup of a high-energy hadron collider. With their sizable cross sections and clean signatures they can be utilized to test the Standard Model at an early stage of data-taking and also test the performance of the detector and the simulation.
In this thesis the inclusive production of W and Z bosons in the muon channel is studied with 36 pb^{-1} of data collected with the CMS detector in 2010 in proton-proton collisions at a center-of-mass energy of $\sqrt{s} = 7$ TeV. In order to measure the production cross sections and their ratios, data-driven analysis techniques are applied for the determination of single-muon efficiencies, the estimation of backgrounds and an evaluation of the hadronic energy in W and Z events. The inclusive cross section for W production in the muon channel is measured to be 9.97 ± 0.03 (stat) ± 0.28 (syst) ± 0.40 (lumi) nb and the ratio of the inclusive cross sections for W^+ and W^- is determined to 1.44 ± 0.01 (stat) ± 0.03 (syst). The inclusive cross section for Z/γ^* production in the muon channel in the invariant mass range 60 GeV $< M_{\mu\mu} <$ 120 GeV is determined to 0.955 ± 0.009 (stat) ± 0.023 (syst) ± 0.038 (lumi) nb, leading to a ratio of the W and Z/γ^* cross sections of 10.44 ± 0.10 (stat) ± 0.30 (syst). The results are in agreement with the theoretical predictions of the Standard Model.
The W boson mass is an important parameter for tests of the consistency of the Standard Model. It is determined to 80.43 ± 0.05 (stat) $\pm$ 0.13 (syst) GeV in agreement with the more precise measurements that dominate the world average.

Contents

Chapter 1

The Standard Model of Particle Physics

1.1 Introduction

The Standard Model of Particle Physics (SM) is a local, relativistic gauge theory describing two out of three known fundamental interactions, the strong [1] and electroweak forces [2–5]. This introduction to the SM is based on [1, 6].
The theory's structure can be decomposed into three parts:

1. **The Symmetry Group** $SU(3)_C \otimes SU(2)_L \otimes U(1)_Y$
   The postulate of local gauge invariance of the theory's Lagrangian under the given set of transformations gives rise to spin-1 gauge fields. Interactions between particles are described as an exchange of these vector bosons: eight massless gluons g corresponding to the eight generators of $SU(3)$ mediate the strong interactions, the weak vector bosons $W^{\pm}$ and Z plus the photon γ correspond to the four generators of the $SU(2)_L \otimes U(1)_Y$ subgroup, which encodes the electroweak interactions. Quantum numbers are associated with each subgroup: color q^i with $SU(3)_C$, weak isospin T^j with $SU(2)_L$, hypercharge Y with $U(1)_Y$. Fermions couple to the gauge bosons according to combinations of these charges. The concept of local gauge invariance is explained in Section 1.2.
   Processes dominated by $W^{\pm}$- or Z- exchange are referred to as weak processes whereas interactions dominated by γ- exchange are called electromagnetic interactions.

2. **The Flavor Content**
   The fermionic matter content is organized in three generations or families. Each family can be split into multiplets of leptons and quarks according to the particles' behaviour under rotations in weak isospin space. The resulting structure reads:

$$\begin{pmatrix} \nu_e & u \\ e^- & d' \end{pmatrix} \quad , \quad \begin{pmatrix} \nu_\mu & c \\ \mu^- & s' \end{pmatrix} \quad , \quad \begin{pmatrix} \nu_\tau & t \\ \tau^- & b' \end{pmatrix}$$

$$\begin{pmatrix} \nu_l & q_u \\ l^- & q'_d \end{pmatrix} \equiv \begin{pmatrix} \nu_l \\ l^- \end{pmatrix} \quad , \quad \begin{pmatrix} q_u \\ q'_d \end{pmatrix} \quad , \quad l^-_R \quad , \quad q_{uR} \quad , \quad q'_{dR}$$

   Corresponding particles in the three families differ in mass and the flavor quantum number, however they couple in the same way to the gauge bosons. All particles are accompanied by antiparticles of opposite electric charge, which is a fundamental consequence when combining principles from quantum mechanics and special relativity [7]. Uncharged particles can be

their own antiparticles (such as the photon).
The leptons come in two species: charged leptons (l^-, $Q_e = -1$) which carry mass and uncharged neutrinos (ν_l, $Q_e = 0$) which are assumed to be massless in the SM[1]. All leptons couple to the weak vector bosons $W^\pm$ and Z but do not carry color.
The quarks q carry color and couple to all the gauge bosons, including gluons. In contrast to the leptons, they carry fractional electric charge. Due to confinement the asymptotic states in quantum chromodynamics (QCD) are colorless, i.e. bound states of quarks and gluons, called hadrons. The quantum numbers of all hadrons unambiguously identified to date can be explained in a twofold sorting pattern: hadrons with three (valence-) quarks of color (rgb), the baryons, and hadrons with one quark and one antiquark of color ($q\bar{q}$), the mesons. Basic properties of QCD are introduced in section 1.2.2.

3. **Spontaneous Symmetry Breaking**

   While the gluons and the photon are massless particles, the weak gauge bosons $W^\pm$ and Z are two orders of magnitude heavier than the proton ($m_W = 80.399 \pm 0.023$ GeV, $m_Z = 91.1876 \pm 0.0021$ GeV [8]). An ad hoc implementation of boson-mass terms in the Lagrangian spoils its local gauge invariance, which is crucial for the renormalizability of the theory. Thus the symmetry must be broken in such a way as to preserve the invariance of the Lagrangian under gauge transformations. This is realized by a spontaneous symmetry breaking of the Lagrangian's electroweak part, which yields a non-symmetric vacuum while keeping the symmetry of the Lagrangian intact:

$$SU(2)_L \otimes U(1)_Y \rightarrow U(1)_{QED} \ .$$

   The electromagnetic symmetry $U(1)_{QED}$ still holds for the ground state of the theory. According to the Goldstone theorem [9], the three broken generators result in three massless spin-0 fields, i.e. three degrees of freedom. In a gauge theory these can be absorbed as the longitudinal, third degree of freedom associated with the $W^\pm$ and Z bosons. Thus the weak gauge bosons acquire a mass in the process of spontaneous symmetry breaking. Spontaneous symmetry breaking is further dicussed in the framework of the electroweak theory in Section 1.3.

1.2 Local Gauge Symmetry

In the SM, the interactions are introduced by demanding invariance under local gauge symmetries. Tracing down the origin of interactions to fundamental symmetry principles does not only lead to an elegant formulation of the theory but is also helpful for solving the theory and moreover crucial for the proof of renormalizability [5], i.e. the theory's mathematical consistency.
The following brief overview starts with the abelian part of the standard model's symmetry group, QED, followed by a brief summary of QCD phenomenology. The more complex construction of the electroweak Lagrangian is presented in Section 1.3.

1.2.1 Quantum Electrodynamics

The Lagrangian of a free Dirac fermion, described by the spinor $\psi(x)$, is given by a kinetic part plus a mass term:

$$\mathcal{L}_0 = i\overline{\psi}(x)\gamma^\mu\partial_\mu\psi(x) - m\overline{\psi}(x)\psi(x) \ , \tag{1.1}$$

yielding the free Dirac equations as the corresponding Lagrangian equations. This free Lagrangian is invariant under global U(1) gauge transformations

$$\psi(x) \rightarrow \psi'(x) = e^{iQ_e\theta}\psi(x) \ . \tag{1.2}$$

[1] Observations of neutrino oscillations prove that neutrinos do have a mass. However, the neutrino masses are small, $m_\nu < 2$ eV [8].

According to Noether's theorem, every continuous symmetry leads to a conserved current and a conserved charge, in this case the electromagnetic current $j^\mu = eQ_e\overline{\psi}\gamma^\mu\psi$ and the electric charge. Under local gauge transformations the kinetic part in Equation 1.1 picks up an extra term, which spoils the gauge invariance:

$$\partial_\mu \to e^{iQ_e\theta(x)}(\partial_\mu + iQ_e\partial_\mu\theta(x))\psi(x) \ . \tag{1.3}$$

The easiest way to introduce local gauge invariance, is to substitute the derivative ∂_μ by the covariant derivative (principle of minimal coupling)

$$D_\mu = \partial_\mu + ieQ_eA_\mu(x) \tag{1.4}$$

with a spin-1 field A_μ transforming as

$$A_\mu(x) \to A'_\mu(x) = A_\mu(x) - \frac{1}{e}\partial_\mu\theta(x) \ . \tag{1.5}$$

The resulting Lagrangian including a gauge-invariant kinetic term for the boson is given by:

$$\mathcal{L} = i\overline{\psi}(x)\gamma^\mu D_\mu\psi(x) - m\overline{\psi}(x)\psi(x) - \frac{1}{4}F_{\mu\nu}(x)F^{\mu\nu}(x) \tag{1.6}$$

$$= i\overline{\psi}(x)\gamma^\mu\partial_\mu\psi(x) - eQ_e\overline{\psi}(x)\gamma^\mu A_\mu\psi(x) - m\overline{\psi}(x)\psi(x) - \frac{1}{4}F_{\mu\nu}(x)F^{\mu\nu}(x) \ , \tag{1.7}$$

including a coupling between the fermion and the boson field proportional to the electric charge, the fermion-photon-vertex of QED. Thus requiring a local gauge symmetry has introduced an interaction to the theory, mediated by a spin-1 particle. The photon is assumed to be massless in the SM (experiment: $m_\gamma < 1 \cdot 10^{-18}$ eV [8]). Since U(1) is abelian, i.e. the transformations commutate, there is no photon self-coupling reflecting the fact that the photon does not carry electric charge.

1.2.2 QCD Phenomenology

The concept of local gauge invariance can be extended to non-abelian groups. Since the absolute value of any quantum field must be conserved in gauge transformations, only unitary groups can play a rôle. The Lie-group $SU(N)$, the group of unitary $N \times N$ matrices U with $\det U = 1$, fulfills that reqirement. $SU(N)$ transformations U are generated by $N^2 - 1$ generators T^a:

$$U = e^{i\theta_a T^a} \tag{1.8}$$

with continuous parameters θ_a. The Lie-algebra is given by the generator's commutation relations

$$\left[T^a, T^b\right] = if^{abc}T^c \tag{1.9}$$

with the structure constants f^{abc}. The strong interactions are based on the $SU(3)_C$ gauge group. Som key features of QCD are:

- The gauge bosons are eight gluons that exhibit self-interactions because $SU(3)$ is a non-abelian group. These self-interactions lead to a decrease of the strong coupling constant α_s with increasing momentum transfer.
- In interactions with high momentum transfer Q^2, quarks and gluons behave as free particles, i.e. the strong coupling constant α_s is small.
- At low energy scales ($\sqrt{Q^2} \lesssim \Lambda_{QCD} \sim 200$ MeV), the strong coupling is large ($\alpha_s \gg 1$) and perturbation theory breaks down. At long distances, $r \gg 1/\Lambda_{QCD}$, quarks and gluons do not appear as single particles carrying color charge, but as QCD bound states that are singlets in color space:

$$B = \frac{1}{\sqrt{6}}\,\epsilon^{\alpha\beta\gamma}|q_\alpha q_\beta q_\gamma\rangle\ , \quad M = \frac{1}{\sqrt{3}}\,\delta^{\alpha\beta}|q_\alpha \bar{q}_\beta\rangle\ . \tag{1.10}$$

The running of α_s makes this confinement hypothesis plausible, although a proof from first principles of QCD is beyond the scope of the current understanding of QCD at low momentum transfer.

At hadron colliders, the initial state consists of colorless bound states ($M_p \sim 1$ GeV) which fall into the energy regime of non-perturbative QCD. The valence quarks determine the quantum numbers of the hadrons. They are embedded in a so-called sea of gluons and $q\bar{q}$ pairs, which, among other properties, account for the better part of the hadron masses. The constituents of hadrons are known as partons. At high enough energies ($Q \gg \Lambda_{\mathrm{QCD}}$, hard scattering), the parton structure of the hadrons can be resolved experimentally, and perturbative calculations of interactions between (asymptotically free) partons are possible. However, the composite structure of the hadron has to be taken into account by parton distribution functions $f_p(x)$ (PDFs), which yield the probability of finding the hard scatter initial state partons in a hadron-hadron interaction.
In this parton picture, the contributions of QCD phenomena at different energy scales are factorized into individual contributions: the perturbative calculation and the PDFs, which at present cannot be calculated from first principle. According to the factorization assumption, the cross section of a hadronic process can be decomposed as:

$$d\sigma(P_i) = \int \left(\prod dx_i f_i(x_i)\right) d\sigma^{parton}(p_i) \tag{1.11}$$

with the hadron momenta P_i and parton momenta $p_i = x_i P_i$. This pattern can be followed both ways, i.e. a process with color-charged objects in the final state is described by a perturbative calculation of the process involving partons and decay functions which describe the subsequent hadronization and are theoretically unknown. This factorization is depicted in Figure 1.1.

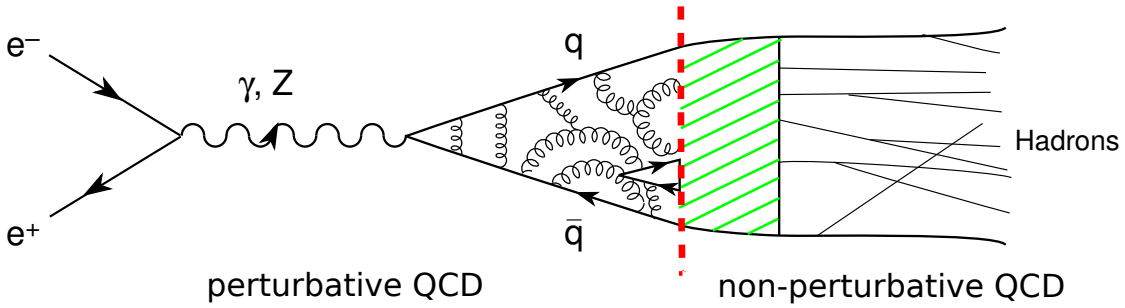

Figure 1.1: An example process with a hadronic final state [1].

The naive factorization sketched above does not lead to physical results due to divergencies which arise in the computation of QCD Feynman diagrams.

- Infrared divergencies occur, when the soft limit of certain parton four-vectors are considered, $p \to 0$. Soft gluon radiation is an example.
- Collinear divergencies stem from QCD radiation with four-momenta parallel or antiparallel to the original parton.

In analogy to divergencies, which are absorbed in renormalization procedures, these divergencies can be absorbed in a redefinition of the naive PDFs $f_i(x_i)$ in Equation 1.11 at an energy scale μ_F, called the factorization scale. This is shown in the factorization theorem of QCD as discussed in [10]. The dependence of the PDFs on the factorization scale can be calculated perturbatively (DGLAP equations [11–13]), whereas the dependence on the momentum fraction x has to be inferred from experiment.

1.3 Electroweak Theory

1.3.1 The $SU(2)_L \otimes U(1)$ Gauge Group

The construction of the electroweak standard model is based on the study of the weak interactions at low momentum transfer. At such energies, weak interaction phenomena can be described by a current-current interaction (Fermi theory), with the following Hamiltonian [14]:

$$\mathcal{H} = \frac{G_F}{\sqrt{2}} J_\mu^\dagger J^\mu \tag{1.12}$$

$$J_\mu = \overline{\psi}_p \gamma_\mu (1-\gamma_5)\psi_n + \overline{\psi}_\nu \gamma_\mu (1-\gamma_5)\psi_e + \dots \,. \tag{1.13}$$

In this low-energy approximation, the Fermi constant $G_F = 1.16637(1) \cdot 10^{-5}$ GeV^{-2} [8] is the only coupling and the currents J_μ are charged, i.e. they connect particles with $|\Delta Q| = 1$. The theory accounts for the observed maximal violation of parity $\mathcal{P}$ and charge conjugation C in charged current reactions by demanding a $(V-A)$ structure of the currents. Only the left-handed components of the fermion fields in Equation 1.13 take part in the interaction. The Fermi constant has negative dimension of mass and thus the theory is not renormalizable. The unphysical high-energy behaviour of the theory is manifest in the antineutrino-electron scattering with leading-order cross-section $\sigma \sim s$ (including higher orders in the coupling G_F does not cure this behaviour). The charged currents exhibit a weak isospin structure based on the group $SU(2)$. In analogy to QCD, another $U(1)$ quantum number, the weak hypercharge Y, can be introduced, fulfilling the Gell-Mann-Nishijima relation:

$$Q = T_3 + \frac{Y}{2} \,. \tag{1.14}$$

The Fermi theory is not a gauge theory and does not provide field-mediating particles. However, the mentioned features of the weak interactions point to the group structure $SU(2)_L \otimes U(1)_Y$ and massive gauge bosons, which allow for a four-point interaction, such as the Fermi theory, as a low-energy approximation.

For simplicity, the following discussion of the electroweak Lagrangian is carried out only with the electron pair of weak isospin multiplets:

$$\mathbf{L} \equiv \begin{pmatrix} \nu_e \\ e^- \end{pmatrix}_L \quad , \quad \mathbf{R} \equiv e_R^- \,. \tag{1.15}$$

The transformations of the fields under the $G = SU(2)_L \otimes U(1)_Y$ gauge group are given by

$$\mathbf{L} \underset{G}{\rightarrow} \mathbf{L'} = e^{i\frac{y_L^l}{2}\beta(x)}\, U_L\, \mathbf{L} \quad , \quad U_L = \exp\left(i\,\frac{\sigma_j}{2}\,\alpha^j(x)\right) \tag{1.16}$$

$$\mathbf{R} \underset{G}{\rightarrow} \mathbf{R'} = e^{i\frac{y_R^l}{2}\beta(x)}\, \mathbf{R} \tag{1.17}$$

with the generators of $SU(2)$, the Pauli matrices σ_j, and four continuous gauge parameters $\beta(x), \alpha^j(x)$. The four gauge bosons enter via minimal coupling in the covariant derivative

$$D_\mu^L \mathbf{L} \equiv \left(\partial_\mu + ig\frac{\sigma_j}{2}W_\mu^j(x) + ig'\frac{Y_L^l}{2}B_\mu(x)\right)\mathbf{L} \tag{1.18}$$

$$D_\mu^R \mathbf{R} \equiv \left(\partial_\mu + ig'\frac{Y_R^l}{2}B_\mu(x)\right)\mathbf{R} \tag{1.19}$$

and demanding gauge invariance fixes their transformation properties

$$\frac{\sigma_j}{2}W_\mu^j \underset{G}{\rightarrow} \frac{\sigma_j}{2}W_\mu'^j = U_L(x)\frac{\sigma_j}{2}W_\mu^j U_L^\dagger(x) + \frac{i}{g}\partial_\mu U_L(x)U_L^\dagger \tag{1.20}$$

$$B_\mu(x) \underset{G}{\rightarrow} B'_\mu(x) = B_\mu(x) - \frac{1}{g'}\partial_\mu\beta(x)\ . \tag{1.21}$$

Due to the non-vanishing structure constants of $SU(2)$, the kinetic term for the gauge fields includes vector boson self-couplings:

$$\mathcal{L}_{kin} = -\frac{1}{4}B_{\mu\nu}B^{\mu\nu} - \frac{1}{4}W^j_{\mu\nu}W_j^{\mu\nu} \tag{1.22}$$

$$B_{\mu\nu} = \partial_\mu B_\nu - \partial_\nu B_\mu \quad , \quad W^j_{\mu\nu} = \partial_\mu W^j_\nu - \partial_\nu W^j_\mu - g\epsilon^{jkl}W^k_\mu W^l_\nu\ . \tag{1.23}$$

The part of the electroweak Lagrangian that arises from the gauge symmetry includes kinetic terms for the fermion and the gauge fields, couplings of both fermion chiralities to the $U(1)_Y$ gauge field $B_\mu(x)$ and the coupling of the fermion doublet with left chirality to the three gauge fields W^j_μ associated with the group $SU(2)_L$:

$$\mathcal{L}_W \sim -\frac{g}{2}\overline{\mathbf{L}}\begin{pmatrix} W^3_\mu & W^1_\mu - iW^2_\mu \\ W^1_\mu + iW^2_\mu & -W^3_\mu \end{pmatrix}\mathbf{L} \equiv -\frac{g}{2}\overline{\mathbf{L}}\begin{pmatrix} W^3_\mu & \sqrt{2}W^\dagger_\mu \\ \sqrt{2}W_\mu & -W^3_\mu \end{pmatrix}\mathbf{L}\ . \tag{1.24}$$

The field $W^3_\mu(x)$ thus contributes to neutral current interactions, such as the field $B_\mu(x)$. The off-diagonal part in Equation 1.24 involves charged gauge bosons $W_\mu = 1/\sqrt{2}(W^1_\mu + iW^2_\mu)$ and $W^\dagger_\mu = 1/\sqrt{2}(W^1_\mu - iW^2_\mu)$, representing the charged current interactions that are mediated by W^+ and W^-, respectively. Since the group $SU(2)_L$ is non-abelian, the coupling of the charged current is fixed by one constant g and all leptons and quarks couple with the same strength to W^+ and W^-, i.e. the coupling is universal [2].

The construction of the part describing neutral current interactions is constrained by QED, which has to be reproduced. Since both fields $W^3_\mu(x)$ and $B_\mu(x)$ couple differently to the left and right fermion chiralities, none of them can be identified with the photon. A combination of the neutral fields leads to the fields observed in nature:

$$\begin{pmatrix} W^3_\mu \\ B_\mu \end{pmatrix} \equiv \begin{pmatrix} \cos\theta_W & \sin\theta_W \\ -\sin\theta_W & \cos\theta_W \end{pmatrix}\begin{pmatrix} Z_\mu \\ A_\mu \end{pmatrix}\ . \tag{1.25}$$

QED imposes the conditions:

$$g\sin\theta_W = g'\cos\theta_W = e \quad , \quad Q = T_3 + \frac{Y}{2}\ . \tag{1.26}$$

As a result of the electroweak unification, the couplings and each particle's electroweak charges are related. Assuming that the electromagnetic coupling e is known, the values of the three parameters g, g', θ_W are fixed by determining one of them experimentally.

The Z has the most complex structure with different vector and axial couplings:

$$\mathcal{L}_Z = -\frac{e}{2\sin\theta_W\cos\theta_W}J^\mu_Z Z_\mu \tag{1.27}$$

$$J^\mu_Z = -\overline{\psi}\gamma_\mu(g_V - g_A\gamma_5)\psi\ . \tag{1.28}$$

The coupling constants are linked to the electric charge, the third component of the weak isospin, and the Weinberg angle:

$$g_V = T_3^f - 2Q_f\sin^2\theta_W \tag{1.29}$$

$$g_A = T_3^f\ . \tag{1.30}$$

For neutrinos, Equation 1.28 has a $(V-A)$ structure and neutrinos of right chirality would not couple.

[2] This statement refers to the weak eigenstates of the fermion fields.

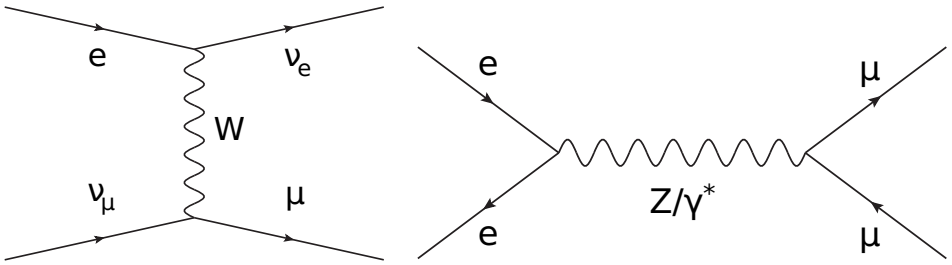

Figure 1.2: Left: Charged current interaction. Right: Neutral Current interaction.

1.3.2 Spontaneous Symmetry Breaking

The electroweak Lagrangian considered so far does not include the necessary mass terms for fermions and the intermediate gauge bosons W^+, W^-, Z.

- Mass terms for the gauge bosons with transformation properties such as reported in Equation 1.20 spoil gauge symmetry:

$$\frac{m^2_{boson}}{2} A_\mu A^\mu \quad , \quad \frac{m^2_{boson}}{2} W^j_\mu W^{\mu j} \ . \tag{1.31}$$

- Fermion mass terms $-m_f \overline{\psi}\psi$ are invariant under the QED $U(1)$ symmetry but mix both chiralities.

$$\mathcal{L}_{m_f} = -m\overline{\psi}\psi = -m\left(\overline{\psi}_R\psi_L + \overline{\psi}_L\psi_R\right) \tag{1.32}$$

  Thus they spoil gauge invariance in theories which do not treat both fermion chiralities on an equal footing, such as the electroweak SM (Equation 1.16).

In both cases, the gauge symmetry is explicitly broken, i.e. the Lagrangian is not symmetric. The so-called Higgs-Kibble [15, 16] mechanism avoids the problem by employing a sponataneous symmetry breaking (SSB).

- The gauge symmetry of the Lagrangian remains intact.
- The Lagrangian has a set of states with minimal energy. Chosing one of these states as the vacuum breaks the symmetry.

In the electroweak SM, the spontaneous symmetry breaking is implemented using a weak isospin doublet of complex scalar fields of weak hypercharge $Y = 1$. The neutral field has a finite vacuum expectation value v. In the context of spontaneous symmetry breaking, three out of the four degrees of freedom are absorbed by the $W^\pm$ and Z vector bosons as longitudinal degrees of freedom. Thus, these spin-1 bosons have acquired a mass. The remaining degree of freedom corresponds to a scalar spin-0 boson, the so-called Higgs field $H(x)$. The $W^\pm$ and Z masses are related at tree-level by:

$$m_W = m_Z \cos\theta_W = \frac{1}{2} v g \ . \tag{1.33}$$

The QED gauge symmetry remains intact after spontaneous symmetry breaking:

$$SU(2)_L \otimes U(1)_Y \xrightarrow[SSB]{} U(1)_{QED} \ . \tag{1.34}$$

1.4 Cross Sections in Theory and Experiment

The basics on how cross sections are determined in theory and experiment are reviewed.

1.4.1 Theoretical Expectation for W/Z Production

At hadron colliders, the leading order process for W/Z boson production is quark/antiquark annihilation (Figure 1.3). At a proton-proton (pp) collider such as the LHC, at least the antiquarks have to be sea quarks. The vector bosons decaying into a quark-antiquark pair cannot be used for analysis because the background from dijet events produced in QCD processes is to high. Therefore, the focus is on the leptonic final state (Drell-Yan process). The description of W/Z production given here is based on [17].

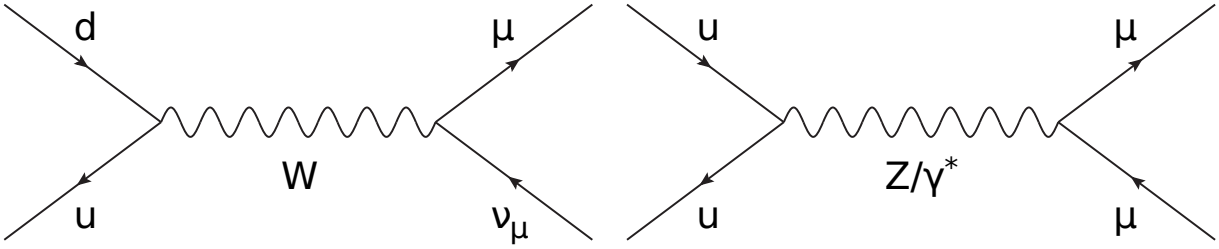

Figure 1.3: Example processes for intermediate vector boson production in leading order at hadron colliders. Left: W^- production. Right: Z production.

The cross sections are given by

$$\sigma_Z = \sum_{q,\bar{q}} \int dx_1 dx_2 \, f_q\left(x_1, \mu_F^2\right) f_{\bar{q}}\left(x_2, \mu_F^2\right) \times \left[\hat{\sigma}_0(\hat{s}) + a\,\hat{\sigma}_1(\hat{s}) + a^2\,\hat{\sigma}_2(\hat{s}) + ...\right]_{q\bar{q}\to ll} \quad (1.35)$$

$$\sigma_W = \sum_{q,\bar{q}'} \int dx_1 dx_2 \, f_q\left(x_1, \mu_F^2\right) f_{\bar{q}'}\left(x_2, \mu_F^2\right) \times \left[\hat{\sigma}_0(\hat{s}) + a\,\hat{\sigma}_1(\hat{s}) + a^2\,\hat{\sigma}_2(\hat{s}) + ...\right]_{q\bar{q}'\to l\nu} \quad (1.36)$$

with the parton-parton center-of-mass energy $\sqrt{\hat{s}} = \sqrt{x_1 x_2}\sqrt{s}$, the perturbative series expressed in terms of $a = \frac{\alpha_s(\mu_R)}{2\pi}$ and the factorization and renormalization scales μ_F and μ_R. In leading order, the production cross sections at parton level are given by [17]:

$$\hat{\sigma}_{q\bar{q}'\to W\to l\nu} = \frac{\sqrt{2}}{N_C} G_F M_W^2 |V_{q\bar{q}'}|^2 \frac{M_W \Gamma_W}{\left(\hat{s} - M_W^2\right)^2 + M_W^2 \Gamma_W^2} \cdot BR(W \to l\nu) \quad (1.37)$$

$$\hat{\sigma}_{q\bar{q}\to Z\to ll} = \frac{\sqrt{2}}{N_C} G_F M_Z^2 \left(g_{V,q}^2 + g_{A,q}^2\right) \frac{M_Z \Gamma_Z}{\left(\hat{s} - M_Z^2\right)^2 + M_Z^2 \Gamma_Z^2} \cdot BR(Z \to ll)\ , \quad (1.38)$$

with the CKM matrix element $V_{q\bar{q}'}$ and the branching ratios of the vector boson decays into leptons $BR(V \to l_1 l_2)$. In case of the Z, the formula above has to be extended for photon exchange, since both processes cannot be distinguished experimentally. The structure of the formula reads:

$$\hat{\sigma}\left(q\bar{q} \to l^+ l^-\right) = \frac{4\pi\alpha^2}{3\hat{s}} \frac{1}{N_C} \left(Q_q^2 - 2Q_q\, g_{V,l}\, g_{V,q}\, \chi_1(\hat{s}) + \left(g_{A,l}^2 + g_{V,l}^2\right)\left(g_{A,q}^2 + g_{V,q}^2\right) \chi_2\left(\hat{s}\right)\right)\ . \quad (1.39)$$

The first term represents the QED contribution, dominant for $\sqrt{s} \ll M_Z$, followed by the interference term and the pure Z exchange.
For simplicity, the general characteristics of the lepton production in $W \to \mu\nu$ events are given averaging over an equal number of W^+ and W^- events. Assuming vanishing transverse momentum of the vector boson, the transverse momentum of the lepton in the lab frame p_T^l is the same as in

the W rest frame. In the case of these simplifications, the transverse momentum distribution of the produced charged lepton is given by [17]:

$$\frac{1}{\sigma_W}\frac{d\sigma_W}{d\left(p_T^l\right)^2} = \frac{3}{M_W^2}\left(1-\frac{4\left(p_T^l\right)^2}{M_W^2}\right)^{-\frac{1}{2}}\left(1-\frac{2\left(p_T^l\right)^2}{M_W^2}\right) . \tag{1.40}$$

The divergence at $p_T^l \to M_W/2$ is washed out by the finite width and finite transverse momentum

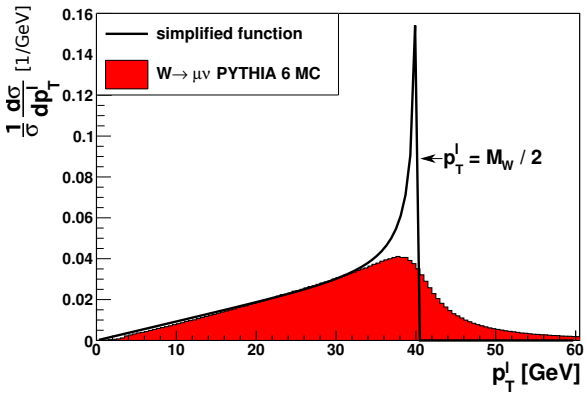

Figure 1.4: Comparison of the lepton p_T spectrum from Equation 1.40 (black) with the simulation ($pp \to W + X \to \mu\nu + X$) at generator level (red). The simulated distribution is scaled to the same area as the simplified function.

of the W (Figure 1.4). However, the characteristic edge, called the Jacobian peak, remains. The dependence of the edge on the W transverse momentum is reduced, when the transverse mass distribution is considered instead of p_T^l. The transverse mass M_T is defined as:

$$M_T \equiv \sqrt{2p_T^l p_T^\nu \left(1-\cos\Delta\phi_{l\nu}\right)} , \tag{1.41}$$

where $\Delta\phi_{l\nu}$ denotes the angle between the lepton and the neutrino in the transverse plane. In the W rest frame, the transverse mass is given by $M_T = 2p_T^l$, and the differential cross section shows a pronounced edge at $M_T = M_W$. The transverse mass is the most characteristic variable for the W at hadron colliders because the full invariant mass cannot in general be reconstructed in the detectors. The QCD backgrounds only allow for a selection of W events with high purity in the leptonic final states $W \to e\nu$ and $W \to \mu\nu$. The neutrino cannot be detected and it has to be approximated by the missing energy in the detector. Since the kinematics of the initial parton-parton interaction are not known, total momentum conservation cannot be applied to determine all three momentum components of the neutrino. However, the transverse momentum in the parton-parton interaction is known to be (almost) negligible. Therefore the missing transverse momentum can be determined, allowing for a definition of the transverse mass which is useful also from the experimental point of view:

$$M_T \equiv \sqrt{2p_T^l \not{E}_T \left(1-\cos\Delta\phi_{l\not{E}_T}\right)} , \tag{1.42}$$

with the missing transverse energy $\not{E}_T$.
The assumption of zero transverse momentum of the vector boson made above is spoiled in practice by two effects.

- The partons in the proton carry an intrinsic transverse momentum, the resulting contribution to the vector boson transverse momentum is denoted k_T.
- Initial state QCD radiation can give the initial partons significant transverse momentum, which is propagated to the vector boson.

The latter effect dominates the vector boson p_T distribution and the vector boson p_T can be regarded as a higher-order QCD effect.

Predicting distributions of kinematic variables is in general more complex than the total cross section determination where these variables are integrated out. In a fixed order calculation, integrable singularities occur and the massive vector boson p_T spectra diverges for $p_T \to 0$ [18], [19]. The singularities take the form of large logarithms:

$$\alpha_s^n \delta\left(p_T\right) \quad , \quad \alpha_s^n \left(\frac{1}{p_T^2} \ln^m \frac{M_{ll}^2}{p_T^2}\right) \quad , n = 1, ..., \infty \quad , \quad m = 0, ..., 2n-1 \tag{1.43}$$

and can be resummed to all-orders, yielding a finite result. The shape of the distribution at low vector boson p_T is severely altered by this resummation compared to the fixed order calculation. Figure 1.5 shows the influence of the resummation in the low p_T region where most vector bosons are produced. For high vector boson p_T, the impact of the large logarithms ceases and the result is dominated by the accuracy of the fixed order calculation.

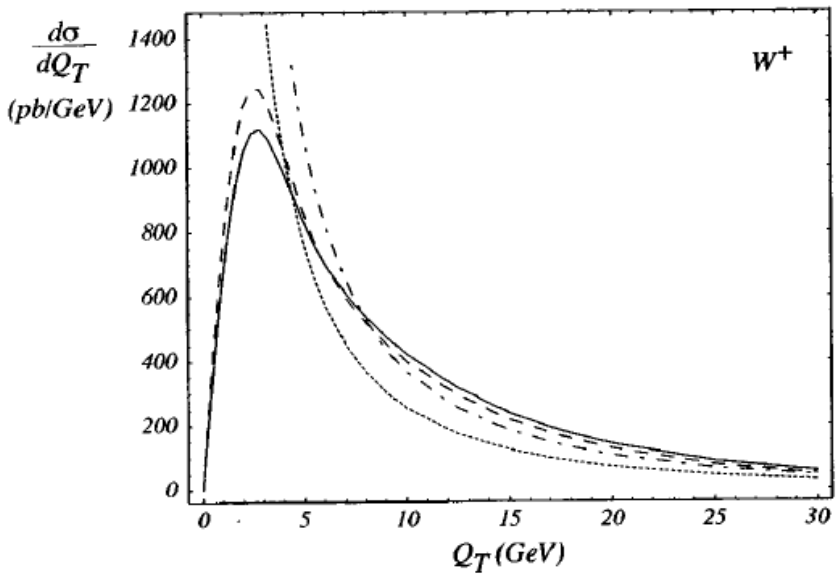

Figure 1.5: Different calculations of the differential W^+ cross section ($Q_T \cong p_T$) [19]. The fixed-order calculations ($\mathcal{O}(\alpha_s)$ (dotted) $\mathcal{O}(\alpha_s^2)$ (dash-dotted)) diverge for vanishing transverse momentum of the vector boson. Two different resummed calculations are shown (dashed and solid).

The PDFs of the individual partons in the proton are shown in Figure 1.6. The valence quark distributions of the proton, $f_u(x)$ and $f_d(x)$, differ in both the integral ($|p\rangle \sim |uud\rangle$) and the shape. Since $u(x)$ is larger than $d(x)$, more W^+ bosons than W^- bosons are produced at proton-proton colliders such as the LHC ($\sigma_W^+/\sigma_W^- > 1$). The result of a measurement of the inclusive cross section ratio is given in Chapter 8.

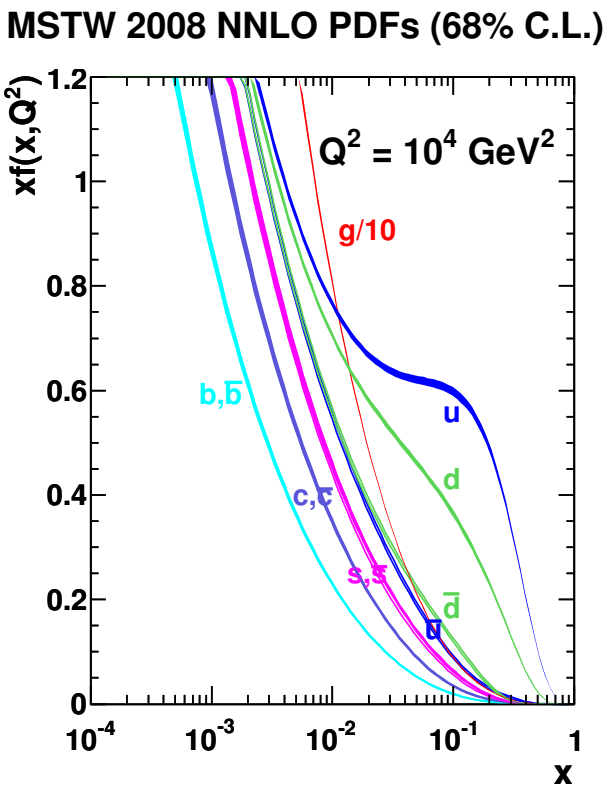

Figure 1.6: Proton PDFs of the individual partons for the MSTW 2008 PDF set (NNLO QCD) [20], [21]. Q^2 denotes the energy scale at which the PDFs are evaluated, i.e. $Q^2 = \mu_F^2$ in Equation 1.35.

1.4.2 Monte Carlo Event Generation

Monte Carlo (MC) event generators interfaced with programs for detector simulation serve as a link between precise theoretical calculations of the processes under study and the full event topology observed within a detector.
The process of event generation involves several steps, which are related to different aspects of the interaction and (especially at hadron colliders) different aspects of QCD [22].

- The **hard process** under study: At large momentum transfer, the parton-parton interaction can be factorized from the rest of the hadron-hadron collision and it can be calculated perturbatively. The simulated samples used within the context of this thesis are based on leading order (LO) and next-to-leading order (NLO) calculations (Chapter 4).

- The **parton shower (PS)**: Coloured particles in the initial and final state are a source of QCD radiation. The radiated gluons carry colour charge as well and give rise to subsequent radiation. The result is a partonic shower which dies off as the momentum transfer in the individual splittings reaches Λ_{QCD} . Before hadronization sets in, the parton shower is like the hard process part of the perturbative component of the simulation.

- **Soft processes and multiparton interactions**: In interactions with low momentum transfer, the partons cannot be treated as free particles. Such processes have to be modeled and tuned. Even if there is a hard interaction in the hadron-hadron collision, the hadron remnants can be subject to soft, secondary interactions. This non-perturbative part of the process is summarized in the term underlying event (UE).

- **Hadronization**: The non-perturbative process(es) converting the parton shower into colorless hadrons. MC generators employ different hadronization models, which are all based

on QCD but cannot be derived from first principle. These models introduce free parameters that have to be tuned on the data.

- The **decay of unstable particles** has to be included in order to give the full picture of the event.

1.4.3 Fundamentals on Cross Section Measurements

From the experimental point of view, a cross section σ is determined by counting the number of events in the final state, N_{tot}, after a set of cuts that selects the process under study. Furthermore, a variable associated with the flux of the colliding partons in the initial state, the luminosity $\mathcal{L}$, has to be measured. In the following $\mathcal{L}$ denotes the instantaneous luminosity and L the integrated luminosity. Apart from this basic input, three further quantities have to be taken into account:

- The number of background events N_{bkg}. It can be estimated from the simulation or determined on the data itself.
- The full detector acceptance $A \cdot \epsilon$. Detectors do not have a 4π coverage in the solid angle. Therefore a fraction of the produced signal events is lost. The full detector acceptance can be split into two parts.
  - The acceptance A includes the effect associated with the reduced geometric coverage and further kinematic cuts. It is determined on MC generated samples and is therefore a theoretical input of the experimental cross section determination.
  - The efficiency ϵ. Several (in)efficiencies of the detector can be determined on the data itself without input from the simulation.

  Acceptances and efficiencies are treated in detail in Chapter 5.

With these definitions the experimental cross section formula reads:

$$\sigma = \frac{N_{tot} - N_{bkg}}{A \cdot \epsilon \cdot L} \ . \tag{1.44}$$

The event selection of the signal processes $W \to \mu\nu$ and $Z/\gamma^* \to \mu\mu$ that are studied in this thesis is described in Chapter 4, leading to the total number of events N_{tot} in Equation 1.44. The determination of the number of background events N_{bkg} is explained in Chapters 7 and 8. The acceptances A and efficiencies ϵ are studied in Chapter 5. The luminosity L and its uncertainty of 4% are external input from [23], [24]. A summary of the luminosity measurement in CMS is given is Appendix A.

Chapter 2

The LHC and the CMS Detector

2.1 The LHC Accelerator

The LHC [25] is a hadron collider designed to accelerate protons and lead ions. The design beam energy for protons is 7 TeV (2.76 TeV per nucleon for lead ions), i.e. 14 TeV center-of-mass energy in the proton-proton interaction. Since March 30, 2010 the LHC operates at a beam energy of 3.5 TeV. The design luminosity, delivered to the high-luminosity experiments CMS [26] and ATLAS [27], is 10^{34} cm^{-2}s^{-1} for proton collisions (10^{27} cm^{-2}s^{-1} for lead ions). At design luminosity about 20 overlapping proton collisions per bunch crossing take place at the interaction points (IP) of CMS and ATLAS. The design luminosity is two orders of magnitude above the luminosity achieved at the proton-antiproton machine TEVATRON and excludes the use of antiprotons. Some design parameters of the LHC are summarized in Table 2.1.
As a hadron accelerator, the LHC mainly serves as a discovery machine. Some key features of hadron colliders are [28]:

- The maximal energy of a proton storage ring is limited by the radius of the ring and the magnetic field in the superconductiong bending dipole magnets. With design parameters, the synchrotron radiation at the LHC amounts to 3.6 kW per beam, which is absorbed by the cryogenic system.

- A monoenergetic proton beam is a wide-band parton beam. Wide ranges of energies can be probed for new phenomena simultaneously rather than measuring at one well-defined energy.

- Different initial states of the hard interaction are possible. This allows for a wide range of interactions to be studied. In particular, the initial state is not restricted to fermion-fermion interactions. The high center-of-mass energy at the LHC gives access to the low-x region of the proton PDF which is dominated by the gluon component.

The LHC was installed in the 26.7 km tunnel constructed for the LEP experiment. The ring comprises eight arcs equipped with the bending dipole magnets and eight streight sections, four of which house the different experiments ALICE [29], ATLAS [27], CMS [26] and LHCb [30]. The complete accelerator complex at CERN and a schematic drawing of the LHC ring are shown in Figure 2.1.
At design luminosity the acceleration process is as follows: The proton beam starts by ionizing hydrogen and is accelerated in the linear accelerator Linac2 to an energy of 50 MeV. The first circular accelerator in the chain is the four-beam pipe Proton Synchrotron Booster (PSB) which emits protons of 1.4 GeV. In the Proton Synchrotron (PS), the protons are accelerated to 25 GeV and the bunch spacing (25 ns, 72 bunches in the PS at design luminosity) is established. Three PS fills are collected and accelerated in the Super Proton Synchrotron (SPS) to 450 GeV and the 2808 bunches of 13 SPS fills are injected in the LHC. The ramp from 450 GeV to 7 TeV per proton corresponds to an increase of the magnetic field in the bending dipoles from 0.54 T to 8.33 T.

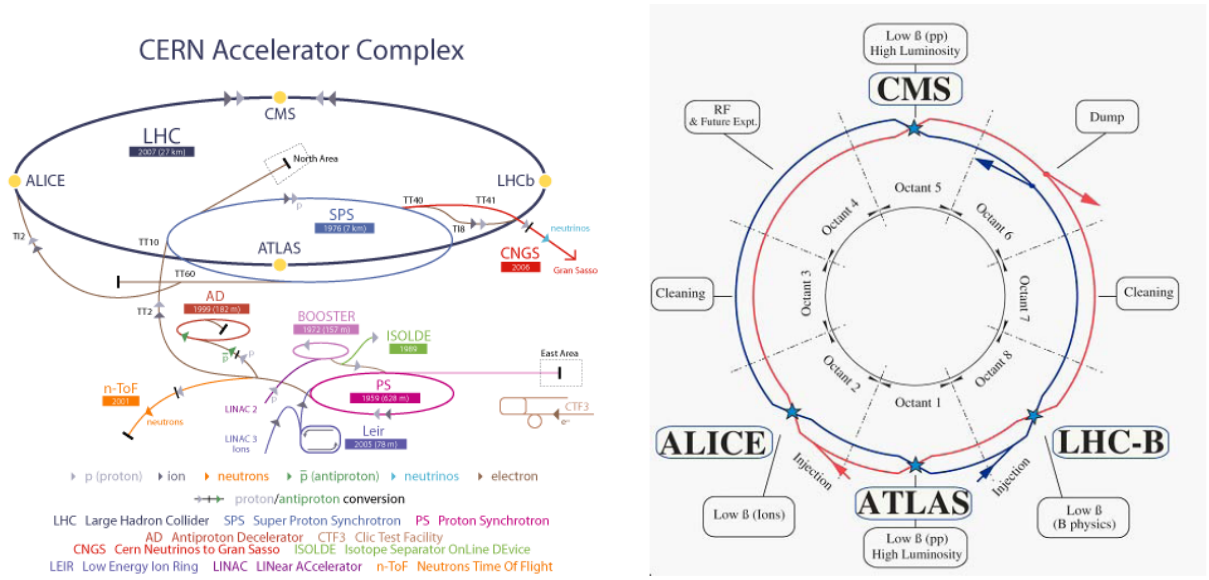

Figure 2.1: Left: The CERN accelerator complex including the pre-acceleration chain for the LHC [31]. Right: Overview of the LHC [25].

At a particle-particle collider such as the LHC, the two beams cannot share a common beam pipe with one magnetic field configuration in the entire ring. Due to the limited ring cross section (3.7 m in diameter) and financial considerations, a two-in-one ring design was chosen instead of two separate rings. The resulting two-bore structure of the magnets with two beam pipes sharing a mechanical structure and the cryogenic system is depicted in Figure 2.2 for the bending dipoles. In order to achieve the high magnetic fields needed, the bending dipoles are superconducting magnets.

2.1.1 Dipole Magnets

The 1232 superconducting, 15 m-long dipoles at the LHC operate at a temperature of the cold mass of 1.9 K, which is achieved by cooling with superfluid helium [25]. Superfluid helium is chosen due to its very high thermal conductivity. The vertical, homogeneous magnetic field in the bores of the dipole is produced by superconducting coils formed by 160 Rutherford-type cables, which run along the beam pipe and carry a current of 11.7 kA at the maximum magnetic field of 8.33 T. Each cable consists of 28(36) strands in the inner(outer) cable-layer of the coil. Each strand is made up of 6300 superconducting filaments of the type-II superconductor Niobium-titanium (NbTi). The filaments have a diameter of 7(6) μm and are surrounded by a thin layer of copper. The coils are held in place by non-magnetic stainless steel structures called collars, that withstand the strong magnetic forces (approximately 400 tons per one meter of dipole). This structure is surrounded by an iron return yoke which is responsible for the better part of the 27.5 t cold mass per dipole. The currents in the coils are applied such that the vertical magnetic fields in the two bores are antiparallel. Variations of the integrated magnetic field from dipole to dipole and field shape imperfections must not exceed 10^{-4}, ensuring a sufficient quality of the beam and low beam loss.

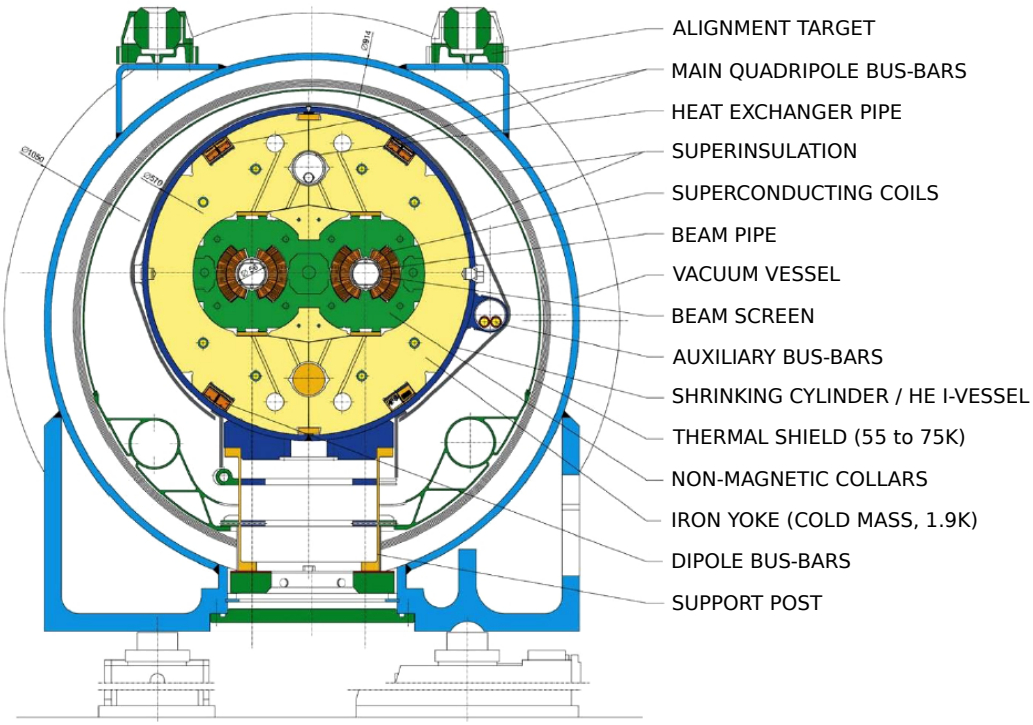

Figure 2.2: The superconducting dipole design [25].

	Design
Proton energy [TeV]	7.0
$\mathcal{L}$ [cm^{-2}s^{-1}]	$1 \cdot 10^{34}$
Protons per bunch	$1.15 \cdot 10^{11}$
Number of bunches	2808
Beam current [A]	0.582
Stored energy per beam [MJ]	362
β Function at IP β^* [m]	0.55
Normalized emittance ϵ_n [μm]	3.75
Bunch spacing Δt [ns]	25

Table 2.1: Design values of the LHC.

2.2 The CMS Detector

This introduction to the main features of the CMS detector is based on [26].
The general concept behind the design of the CMS detector can be motivated by the following consideration: One (of many) major challenge(s) to be met by an LHC multi-purpose detector is the measurement of muons in the outermost subdetector, the muon system, with energies of the order of 100 GeV - 1 TeV with a precision of $\Delta p/p \sim 10\%$. Due to their minimal-ionizing nature in a wide energy range (350 MeV $\lesssim p_T^{\mu} \lesssim$ 100 GeV), muon detection is based on tracking detectors for which the relative transverse momentum resolution is roughly proportional to $\frac{1}{BL^2}$, with the magnetic field B and the radial dimension of the muon system in the transverse plane L. Thus, for a given resolution there are two general concepts: A strong average magnetic field and a compact detector or a smaller average magnetic field and a bigger detector volume. The CMS design is driven by the first approach, ATLAS adopts the latter.
The CMS detector is depicted in Figure 2.3. The main detector components which are described in the following are (inside-out): Silicon pixel detector, silicon strip detector, electromagnetic calorimeter (ECAL), hadronic calorimeter (HCAL), solenoid coil and the iron return yoke equipped with the muon system. The solenoid and iron return yoke form both the mechanical structure of

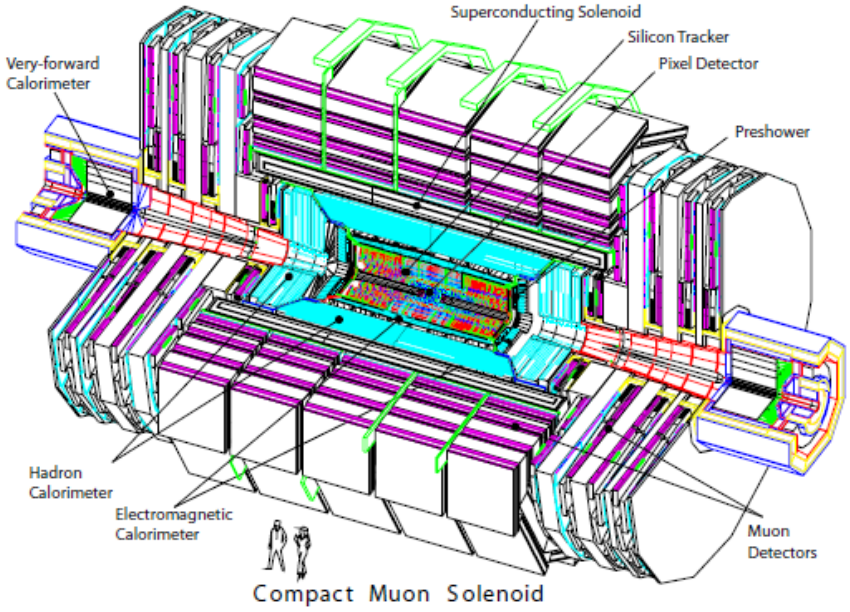

Figure 2.3: The CMS detector with its different subsystems [26].

the experiment and the magnetic field configuration. The magnetic field amounts to 3.8 T within the solenoid and saturates the iron with a magnetic field of about 2 T. The iron yoke is divided into five wheels and two endcaps and is responsible for the better part of the overall detector weight of approximately 14000 tons. The CMS coordinate system is shown in Figure 2.4.

2.2.1 The Solenoid

The superconducting solenoid produces a homogeneous magnetic field of 3.8 T along the beam pipe within its 12.5 m length and 6 m diameter free bore. Both the overall stored energy of 2.6 GJ and the stored energy per cold mass of 11.6 kJ/kg are unprecedented. The magnet operates at a temperature of 4.45 K and with a current of 19.14 kA, within the superconducting regime of the NbTi conductor. The windings are made of four layers, which comprise Rutherford-type cables within an aluminium alloy structure. The overall cold mass is 220 t.

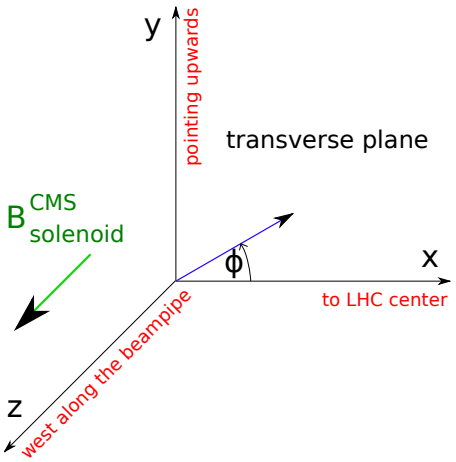

Figure 2.4: The CMS coordinates. The angle ϕ is defined in the transverse plane spanned by the x and y coordinates.

2.2.2 Silicon-based Tracking Detectors

A comprehensive description of the CMS inner tracking system can be found in [32].
The inner tracking system of CMS operates in the solenoid field and is designed for the accurate detection of $\sim$ 1000 charged particles from 20 overlapping collisions which occur every 25 ns at design luminosity. It measures 5.8 m in length and has a diameter of 2.5 m with a geometrical coverage within $|\eta| < 2.5$. The inner tracking system is divided into a silicon pixel detector comprising three barrel detector layers between 4.4 cm and 10.2 cm away from the center of the detector and a silicon strip detector of 10 barrel layers. The cylindrical design of the barrel detectors is closed by tracker endcaps (Figure 2.5).
As the innermost detector component, the tracking system has to cope with highest hit rates ranging from $\sim$ 1 MHz/mm^2 at the inner radius of the pixel detector to $\sim$ 3 kHz/mm^2 at the outer strip detector surface. The main goals to be achieved are:

- High granularity and thus a high number of read-out channels to be able to resolve single tracks.
- Fast detectors assigning the high number of tracks to the right bunch crossing.
- Radiation hard material ensuring a lifetime of $\approx$ 10 years (except for the pixel detector).

This leads to the choice of silicon-based detectors.
The leakage current of the silicon sensors increases with time due to radiation. This leads to higher temperatures of the detector material and in turn to even higher leakage currents. In order to avoid strongly increasing leakage currents and the influence of lattice defects, the tracker volume is cooled to below -10°C at design luminosity. With its active detector area of about 200 m^2, the structures needed to hold it in place and the cooling system, the tracker necessarily comprises more material than previous tracking detectors. This causes multiple scattering, bremsstrahlung and photon conversion within the tracker, which have to be considered at the reconstruction stage. The material budget varies between 0.4 X_0 and 1.8 X_0 in units of radiation length.
A cross-section of both tracking detectors is shown in Figure 2.5.

Pixel Detector

The pixel detector is built from 1440 pixel modules with a total of 66 million pixels on an area of 1 m^2. The modules are assembled in three layers at a distance of 4.4, 7.3, and 10.2 cm from the center of CMS and two discs at each side of the pixel detector. The area of a pixel cell is 100 μm $\times$ 150 μm. In contrast to the long strips, a three-dimensional reconstruction is

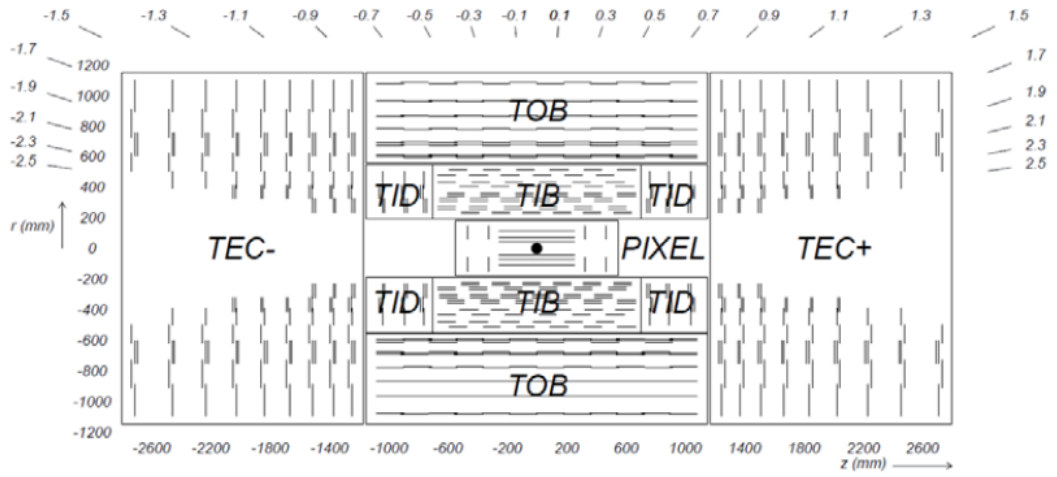

Figure 2.5: Cross section of the inner tracking detectors [26].

possible which allows for a precise vertex reconstruction with a resolution of about 10 μm. This precision is crucial for the tagging of heavy flavor decays (B physics) and τ leptons as well as the distinction between the vertex of interest and overlapping pileup. Due to the analog read out, a charge interpolation between neighbouring pixels is possible and a spatial resolution of $10-15$ μm can be achieved.

Micro-Strip Detector

The layers of the silicon strip detector extend from an inner radius of 20 cm to an outer radius of 116 cm. As depicted in Figure 2.5, the silicon strip detector is divided into a central barrel and an endcaps.
The Tracker Inner Barrel (TIB) consists of four layers of strip modules aligned in parallel with the beam pipe, all of which provide measurements of the r-ϕ coordinate. The two inner layers employ double sided modules with an additional strip that is oriented with a 100 mrad stereo angle. This allows for measurements of the z coordinate. The Tracker Outer Barrel (TOB) starts at a radius of $r > 55$ cm and consists of six layers. The cell size increases towards the outer regions of the tracker barrel due to the decreasing flux from 10 cm $\times$ 80 μm to 25 cm $\times$ 180 μm. In the inner part of the silicon strip detector, the single point spatial resolution is about 20 μm, in the outer part it is about 40 μm. In the region $|z| > 118$ cm the tracker consists of two Tracker End Caps (TEC) of nine disks each. In total 9.3 million strips form an active silicon area of 198 m^2.
The resolution of the tracker for muon tracks with 20 GeV $< p_T <$ 100 GeV relevant for this thesis is of the order of 1%. The geometrical coverage of the tracker is $|\eta| < 2.5$.

2.2.3 Electromagnetic Calorimeter

The electromagnetic calorimeter (ECAL) [33] is responsible for the detection of photons and electrons. Moreover the electromagnetic component of hadronic jets ($\pi^0 \to \gamma\gamma$) has to be measured with a good response. The size of the calorimetry in CMS is severely constrained by the compact design of the detector and the huge silicon tracker. Therefore lead tungstate ($PbWO_4$) is used as a scintillator, providing a high density of 8.28 g/cm^3, short radiation length of 0.89 cm and a small Molière radius of 2.2 cm. These features of the scintillator allow for a homogeneous calorimeter[1] with both a compact design and high granularity. Furthermore, the scintillation decay time of the crystals is of the same order as the bunch spacing of 25 ns at design luminosity. The main challenges associated with $PbWO_4$ are the low light output and its sensitivity to variations in temperature. At a temperature of 18°C, which is controlled to stay constant at the level of

[1]The crystals act as both absorber and scintillator.

0.05°C, about 4.5 photoelectrons per MeV reach the photomultipliers. The scintillation light has a maximum at a wavelength of 420-430 nm.

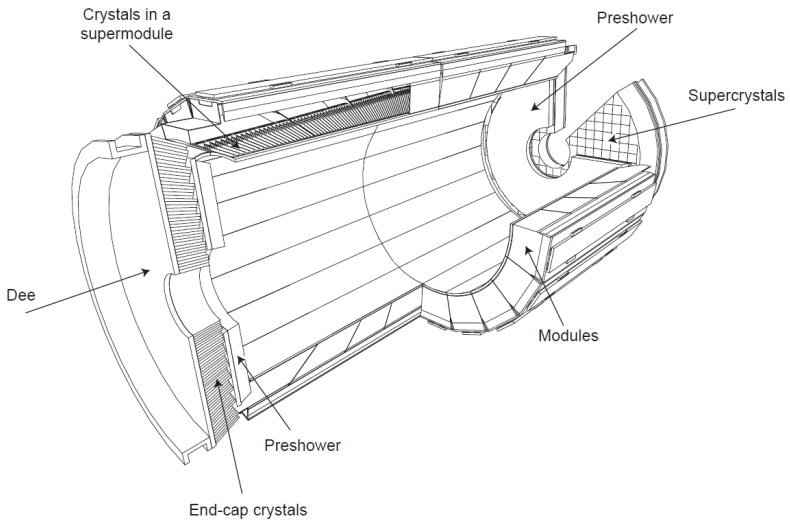

Figure 2.6: The CMS electromagnetic calorimeter [26].

The structure of the ECAL is shown in Figure 2.6. The barrel part (EB) within $|\eta| < 1.479$ is equipped with 61200 crystals measuring 23.0 cm corresponding to 25.8 X_0 in units of radiation length. The crystals' truncated pyramid geometry provides a segmentation of 0.0174×0.0174 in η-ϕ. The outer surface of each crystal is equipped with avalanche photodiodes (APDs). At the scintillation light maximum of about 430 nm, the APDs provide a quantum efficiency of 75 %.
The endcap regions (EE) consist of two disks with 7324 crystals each and extend from $|\eta| = 1.479$ to $|\eta| = 3.0$. Due to the higher fluxes in the endcap, the scintillation light is amplified by very radiation-hard vacuum phototriodes (VPTs).
In the forward region boosted neutral pions are likely to fake a single photon signature in the ECAL crystals. This is avoided by a 20 cm thin preshower detector installed in front of the crystals in the region $1.653 < |\eta| < 2.6$. It is built from two layers of lead absorber and silicon strip sensors forming a disk. The strips in the two layers are perpendicular to each other. The pitch of the strips is about 2 mm and allows for the separation of the two photon induced showers to be resolved.
For energies below 500 GeV the resolution of the ECAL can be decomposed in three terms (statistical, noise, constant [26]):

$$\left(\frac{\Delta E}{E}\right)^2 = \left(\frac{2.8\%}{\sqrt{E/\mathrm{GeV}}}\right)^2 + \left(\frac{12\%}{E/\mathrm{GeV}}\right)^2 + (0.3\%)^2 \ . \tag{2.1}$$

The geometrical coverage of the ECAL extends to $|\eta| = 3$.

2.2.4 Hadron Calorimeter

The main task of the hadron calorimeter (HCAL) [34] is the measurement of hadron jets and other hadronic fragments from the proton-proton interaction. The need for detecting as much of the energy contained in an event and an evaluation of the transverse momentum balance implies a large coverage of the hadron calorimeter as close to the beam pipe as possible, including special forward detectors extending to $|\eta| < 5.2$. As for the ECAL, the total amount of energy must be contained in a small volume.
As shown in Figure 2.7, the HCAL consists of four parts, the hadron barrel (HB), the hadron endcap (HE), hadron outer (HO) and the hadron forward (HF) calorimeters. It is a sampling

calorimeter with absorber plates made of brass and steel for showering and plastic scintillator as the active material.

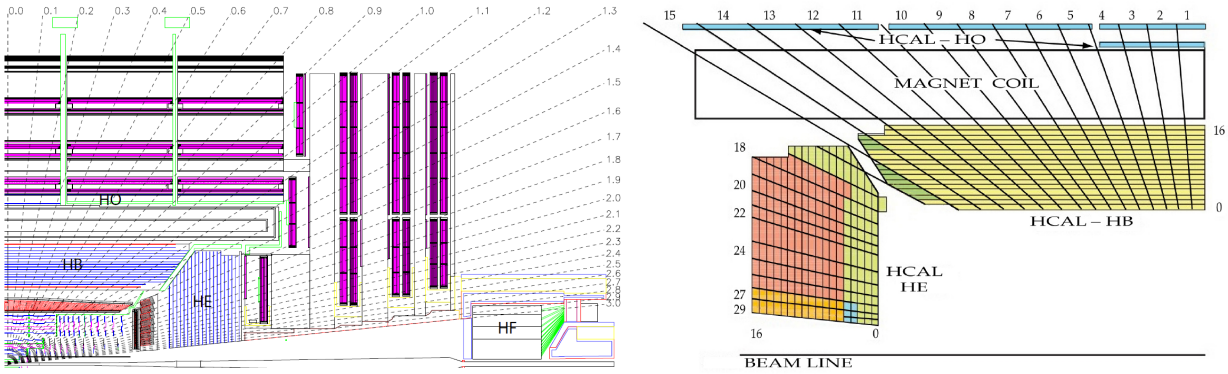

Figure 2.7: Left: The different HCAL components in the CMS detector. Right: Longitudinal segmentation of the HCAL towers in the central part of the detector. [26]

The HB calorimeter is mounted between the outer surface of the ECAL (r=1.77 m) and the inner surface of the solenoid coil (r=2.95 m) and covers the region within $|\eta| < 1.3$. The absorber provides 5.82 interaction lengths (λ_I) of material for $\eta = 0$ increasing to 10.6 λ_I at $|\eta| = 1.3$. An additional 1.1 interactions lengths are provided by the ECAL. The segmentation of the plastic scintillator tiles in η-ϕ towers is 0.087×0.087 , corresponding to about 5×5 ECAL crystals. About 70000 scintillator tiles have to be read out in the HB. The scintillation light is collected by wavelength-shifting fibres and guided by optical cables to hybrid photodiodes (HPDs), which can operate in high magnetic fields. Before read out, signals from subsequent tiles are added optically to form a tower. The towers are further segmented longitudinally as depicted in Figure 2.7.
The detection mechanism in the hadron endcap calorimeter (HE), covering the rapidity range $1.3 < |\eta| < 3$, is similar to the above. The absorption thickness (including the ECAL endcaps) amounts to about 10 λ_I.
The spatial constraints for the HCAL limit the absorber thickness in the barrel region. In order to reduce undetected shower leakage, a so-called tail catcher (or hadron outer, HO) is installed behind the solenoid coil. Every wheel in the iron return yoke is equipped with a layer of scintillator behind the solenoid coil, which is used as an absorber. Since the absorption thickness has its minimum at $\eta = 0$, the central wheel has an extra 19.5 cm layer of iron behind the solenoid coil with scintillator tiles on both sides. The total absorption thickness is increased by the HO to about 11.8 λ_I in the barrel region.
The forward region of the detector is exposed to very strong radiation that makes a different choice of technology for the forward hadron calorimeter (HF) necessary. Radiation hard quartz fibres are used as the active medium. The HF is cylindrical in shape, starts 11.2 m from the interaction point and measures about 3.5 m in length. The absorber structure is 165 cm thick, corresponding to 10 λ_I and built from 5-mm-thick grooved steel absorber plates. The quartz fibres are inserted in the groves and detect the Cherenkov light emmited by charged particles above the Cherenkov threshold which is minimal for electrons ($E \geq 190$ keV). Therefore, the HF has a better response to the electromagnetic shower components than to the hadronic part. The fibres are divided into two sets: The first set runs over the full absorber thickness and the other starts 22 cm behind the front of the HF. Both sets are read out separately, allowing for the distinction of electromagnetic showers which deposit a large energy fraction within the first 22 cm of the detector and hadronic showers. The fibres are bundled into towers of 0.175×0.175 in η-ϕ. The HF coverage extends to $|\eta| = 5.2$.
Apart from the energy dependence, the resolution depends on the physics object under study and the η region. For jets in the range 20 GeV $< E_T^{jet} <$ 1 TeV, the resolution (HCAL and ECAL

combined) can be approximated by [35]:

$$\left(\frac{\Delta E}{E}\right)^2 = \left(\frac{1.25}{\sqrt{E/\mathrm{GeV}}}\right)^2 + \left(\frac{5.6}{E/\mathrm{GeV}}\right)^2 + (0.03)^2 \ . \tag{2.2}$$

2.2.5 Muon System

Since muons are the only particles likely to pass through the inner detector parts and propagate further through the iron return joke, the muon system of CMS [36] is the outermost subdetector installed in the yoke. Muons are produced in many important physics channels from precision tests of the standard model to the search for the Higgs boson and models of new physics. The unique minimal-ionizing nature of muons within the energy range 350 MeV $\lesssim E_\mu \lesssim$ 100 GeV offers low fake rates and the low probability of bremsstrahlung for muons with $E_\mu \lesssim 200$ GeV allows for a clean signature and a momentum measurement with high resolution. The exploitation of these features calls for a muon system with wide angular coverage and thus, given the distance to the interaction point, a huge detector area. It has to provide muon identification, momentum and charge measurement and triggering. CMS meets these challenges with a multi-layer muon system extending to $|\eta| = 2.4$ with 3 different types of gaseous detectors covering an area of 25000 m^2.

- In the barrel region ($|\eta| < 1.2$) with its low rate of muons and its relatively homogeneous magnetic field mainly contained in the iron return yoke, **drift tubes (DT)** are installed.
- In the endcap region ($0.9 < |\eta| < 2.4$) both the muon rate and the background level are higher than in the center of the detector. The magnetic field is large close to the edges of the solenoid and not uniform over the radius of the endcaps. **Cathode strip chambers (CSC)** which provide a higher granularity and radiation hardness than DTs are used in the iron return yoke endcaps.
  The DTs and CSCs are used for all the muon system's tasks mentioned above. They are different types of multiwire proportional chambers.
- **Resistive plate chambers (RPC)** with their fast response are used for fast pattern recognition and provide additional information for triggering. They also ensure redundancy in the muon identification and help to resolve ambiguities in the fitting of tracks to the hits in a chamber.

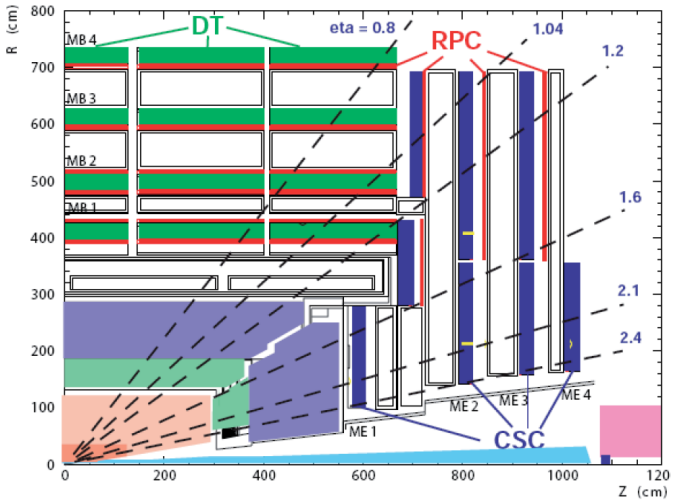

Figure 2.8: The CMS muon system [37].

Drift-Tube Chambers

The smallest unit of the muon chambers in the barrel is the drift cell with an anode wire at a voltage of +3600 V, 2 cathodes at a voltage of -1200 V and 2 field forming electrodes at a voltage of +1800 V. The 13 mm × 42 mm cross section of a drift cell is depicted in Figure 2.9. A muon passing the gas volume ionizes the gas, the initial electrons (ions) drift to the anode (cathodes) and the electrons lead to further ionization in the proximity of the anode wire. The electric signal is proportional to the initial ionization. The cells are filled with a 85% Ar + 15% CO_2 gas mixture that ensures a sufficient linearity of the space-drift-time relation and drift velocities of about 55 μm/ns. The maximal drift time is 380 ns for a distance of 21 mm. The time tagging resolution is of the order of a few nanoseconds and with the precise knowledge of the drift time and linearity of the drift-time-space relation, a single wire spatial resolution of 250 μm is achieved.

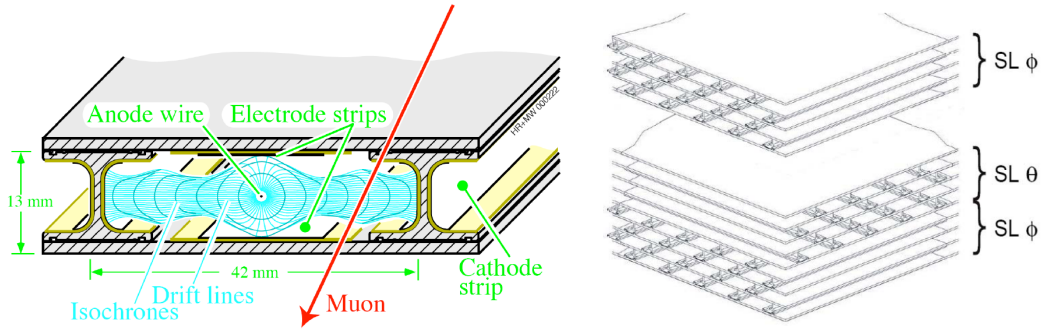

(a) Cross section drift cell with electric field configuration. (b) Superlayers in a chamber.

Figure 2.9: Illustration of a drift cell [26] and the configuration of superlayers in a DT chamber.

Four rings of muon chambers equipped with drift tubes, called stations, find place in the iron return yoke of the CMS barrel. The first station (MB1) is placed right behind the tail catcher of the HCAL, two stations (MB2, MB3) are mounted between the three rings of the iron return yoke and another station (MB4) forms the outer layer of the CMS detector. The 3 × 60 chambers in stations 1 to 3 house three so-called superlayers made of four layers of drift tubes, while the 70 chambers in station 4 only contain two superlayers. The tubes within successive layers are staggered by half a tube to eliminate cracks in the detector coverage and allow for the good time-tagging resolution with meantimer circuits. The design with separated layers of drift cells allows for a differentiation of correlated cell hits as produced by a muon and uncorrelated hits by neutrons, photons or noise. In the chambers of stations 1 to 3, the two outer superlayers have anode wires parallel to the beam pipe and measure the r-ϕ coordinate, whereas the superlayer in the middle is mounted with its wires perpendicular to the beam for measuring the z coordinate. The two r-ϕ superlayers are installed at the bounds of the chamber to ensure maximal angular resolution of the track stubs reconstructed in the chamber. With 2 × 4 cell hits per chamber a spatial resolution of 100 μm in r-ϕ is achieved by a chamber. The layout of the chambers in stations 1 to 3 is shown in Figure 2.9. The chambers in station 4 only measure the r-ϕ coordinate. About 172000 sensitive wires are used in total, most of them 2.4 m long.

Cathode-Strip Chambers

As shown in Figure 2.8, the CSCs are organized in four endcap sections, ME1 to ME4, each of which is divided into rings. Each ring consists of chambers covering an azimuthal angle of 10° or 20°. As in the case of the barrel muon system, the chambers overlap and cover the entire azimuthal angle. The rapidity range covered is $0.9 < |\eta| < 2.4$. Within $0.9 < |\eta| < 1.2$ the CSC and DT systems overlap.
The detection principle is shown in Figure 2.10. Each CSCs consist of 7 cathode panels with

radially oriented strips, which enable a measurement of the ϕ coordinate. Six anode wires are spanned in the gas-filled gaps between the cathode panels. The wires run perpendicular to the cathode strips and provide measurements of the radial coordinate r. A charged particle traversing the gaseous volume ionizes the gas, electrons are detected by the anodes and ions by the cathodes. The small spacing between the electrodes ensures fast readout of the order of some nanoseconds and acceptable occupancy.

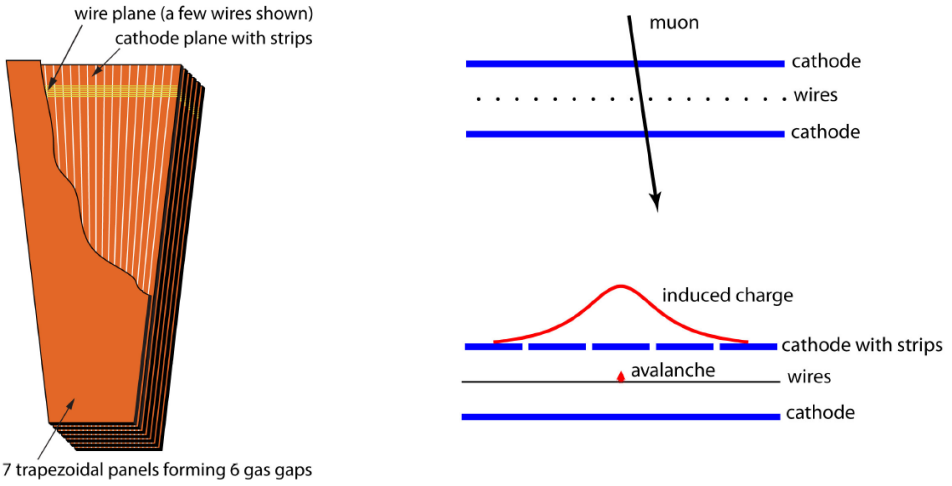

(a) Structure of a CSC.

(b) Detection principle for the cathode signal.

Figure 2.10: Layout and detection principle in the CSCs.

Due to the different fluxes and the varying magnetic field, the CSCs closest to the solenoid coil (72 ME1/1 chambers) have a different design than the other 396 chambers. The latter have gaseous volumes between two cathode panels that are 9.5 mm thick and the gold-plated tungsten wires at a HV of $\sim$ 3.6 kV are 3.2 mm apart. Each of the wires is 50 μm thick. 16 wires are combined to one readout channel. The gas mixture used is 40% Ar+50% CO_2+10% CF_4. The spatial resolution in ϕ of six-plane chamber varies due to differences in the design between $\sim$ 40 μm ($\sim$ 100 μm) for the innermost chambers to $\sim$ 80 μm ($\sim$ 200 μm). The sensitive plates cover 5000 m^2 and the number of wires contained in the 50 m^3 of gas is about 2 million.

Resistive Plate Chambers

The resistive plate chambers (RPCs) employed by CMS consist of two parallel plates which enclose a gaseous volume with a thickness of a few millimeters. A high voltage is applied between the plates, which are coated with conducting graphite paint. The electrodes are transparent to the field of the electrons from ionization. They induce charge on metallic strips on top of the anode, insulated from the graphite coating. This induced 'fast' charge is the useful signal of the RPC rather than the drifting electrons. The RPCs are able to tag the time of a hit faster than the 25 ns bunch spacing, allowing for an unambiguous assignment of a BX to a track candidate. The barrel comprises 480 RPC chambers with 80640 strips and a surface area of 2400 m^2. In the endcaps, 3 RPC stations are installed at startup. They cover a pseudorapidity range up to $|\eta| = 1.6$ [2]. With their excellent time resolution and sufficient spatial resolution of $\sim$ 1 cm, the RPCs are used as an independent trigger system that matches the hit distribution in the RPC stations from hits with time coincidence to predefined hit patterns. This way, both time and momentum information are obtained.

[2]Another station of RPCs will be added and the pseudorapidity coverage of the RPC system will be extended when the LHC reaches design luminosity.

In order to exploit the spatial resolution of the individual chambers for the momentum resolution, all the chambers in the muon system have to be aligned with a precision of some hundered microns with respect to each other and the inner tracker. This is achieved and monitored by a special muon alignement system. Studies of the muon momentum resolution have been carried out on simulation [26,36,38] and muons from cosmic rays [39]. The results derived from the simulation are depicted in Figure 2.11. The resolution for the muons with 20 GeV $< p_T^{\mu} <$ 100 GeV, which are relevant for this thesis, is of the order of 1% or better due to the resolution of the tracker.

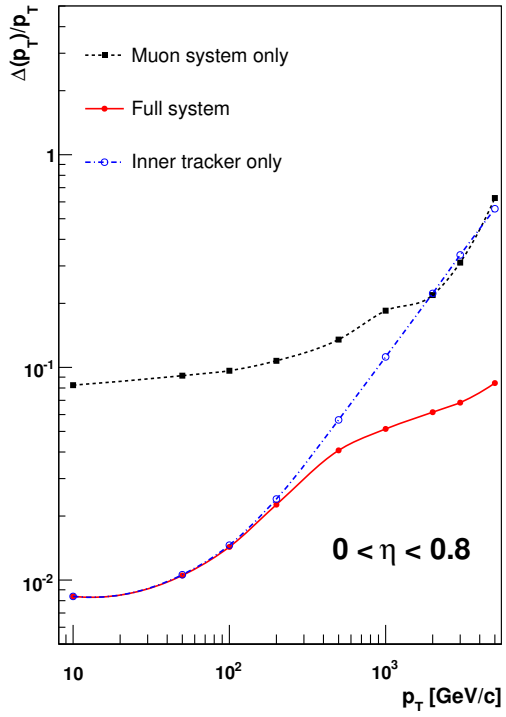

Figure 2.11: Simulated muon transverse momentum resolution as a function of the muon transverse momentum in the central detector region [26].

Chapter 3

Triggering and Reconstruction

3.1 Trigger

The CMS trigger is described in detail in [40]. The following summary is based on [26].
At design luminosity the event rate including pileup events is of the order 10^9 Hz. The corresponding data is too much to be stored and the potentially interesting physics has to be filtered online before analyzing the data. The event rate has to be reduced by the trigger by a factor of 10^7. A rate of 10^2 Hz after triggering can be stored on tape and can be distributed via the LHC Computing Grid [28, 41]. The data to be stored amounts to about 1 MB per event at design luminosity. CMS reduces the rate by a two-level trigger system, depicted in Figure 3.1.

- A Level-1 (L1) trigger made up of custom-designed and largely programmable electronics uses information from the calorimeters and the muon system (plus so-called technical trigger bits from different subdetectors) to provide a reduction down to a rate of about 30 kHz (design limit 100 kHz). The L1 trigger has to check every event and thus has to be fast. The latency time between the bunch crossing and the propagation of the L1 trigger decision to the front-end electronics is 3.2 μs which only allows for a fraction of the event's total information to be included in the L1 triggering process.

- A high-level trigger (HLT) which is a software system running on a processor farm of about one thousand CPUs. In contrast to the L1 trigger, the HLT algorithms are entirely software-based and they can access the full digitized data. The HLT reduces the accept rate of $\mathcal{O}(100$ kHz) to 10^2 Hz (up to 300 Hz). The HLT decision(s) takes $\mathcal{O}(1$ s).

3.1.1 Data Acquisition and Storage

The CMS Data Acquisition (DAQ) system [26] has to cope with the input rate of 100 kHz accepted by the L1 trigger. This corresponds to a data flow of 1 GByte/s. A simplified model of the architecture of the CMS DAQ system is shown in Figure 3.2. After a L1 trigger has fired, the associated data that has been stored in the buffers of the front-end-systems (FES) of the subdetectors is forwarded to the DAQ system. The event builder network collects the data which is associated with the L1 trigger from the different subdetectors. The resulting event is forwarded to the filter system where the HLT algorithms run on the data. After the HLT decision the remaining data is stored on tape. One copy of the data remains at CERN and further copies are distributed to computing resources worldwide. The computing network called the LHC Computing Grid [28, 41] exhibits a hierarchical structure. It starts from the *Tier-0* at CERN that processes and stores the original data and produces reconstructed datasets, followed by *Tier-1* centers, which hold copies of the data, carry out second-pass reconstructions of the original raw data and provide computing resources for large-scale analyses. At the *Tier-2* centers storage and CPU resources for regular analysis activities and the production of simulated Monte Carlo samples are provided.

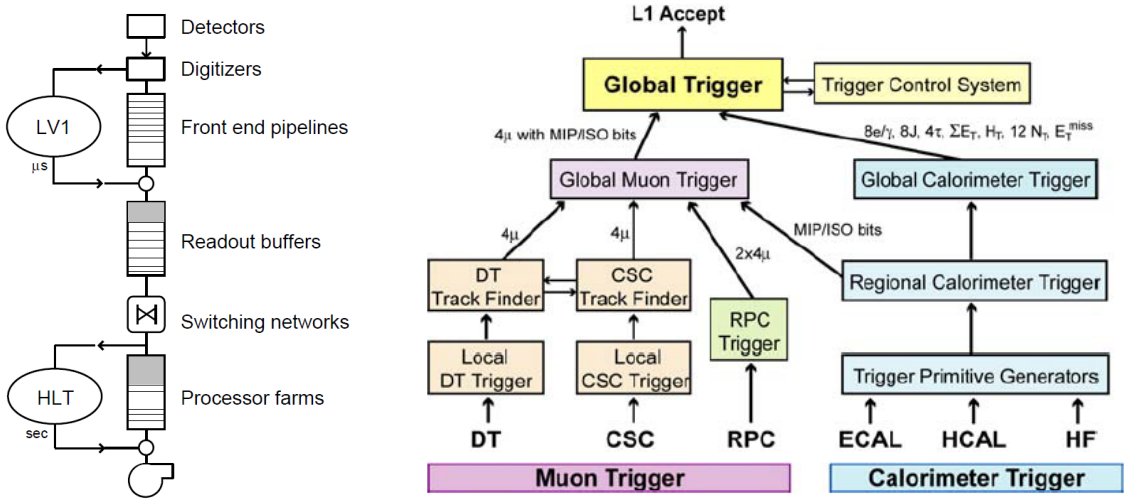

(a) Schematic layout of the CMS trigger system.

(b) Layout of the L1 trigger.

Figure 3.1: Layout of the CMS trigger system. The trigger is seperated into two levels based on partly programmable electronics (L1) and online 'analysis' by entirely programmable algorithms with access to the full data (HLT) [26].

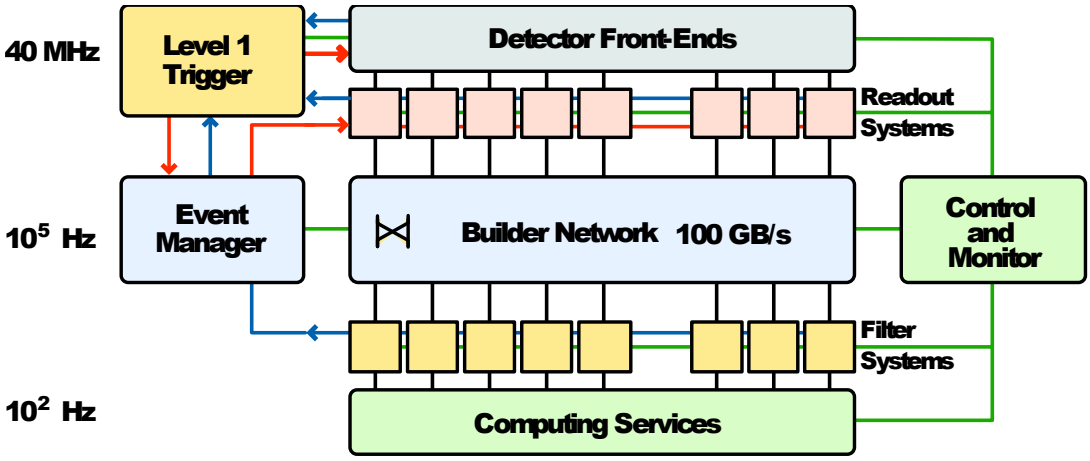

Figure 3.2: Schematic drawing of the CMS DAQ system [26].

3.1.2 L1 Trigger

The L1 trigger uses signals from the calorimeters and the muon subsystems, whereas the entire high-resolution information from the tracker is pipelined at first and used after the readout of the entire event at the HLT stage. The challenge of the L1 trigger is thus a trigger decision with high efficiency for the physics objects and higher-order objects (e/γ, μ, $jets$, $\not\!\!E_T$) and sufficient suppression of noise and background signals with only a fraction of the actual information.
The L1 trigger consists of three layers: local, regional and global trigger parts. At the lowest level so-called Trigger Primitive Generators (TPG) search for deposits in calorimeter towers or track segments and hit patterns in the muon subsystems (local DT and local CSC triggers in Figure 3.1). The regional trigger components combine the locally reconstructed objects in a limited detector segment (DT and CSC track finder in Figure 3.1). They assign an energy/momentum estimate and a measure of quality to the candidate objects. This allows for a ranking of the candidates. At the global trigger level, all the relevant trigger information is combined and the highest-ranked muon and calorimeter objects are forwarded to the Global Trigger that decides whether the event is passed on to the HLT or not.
Since the muon triggering is important for the analysis presented in this thesis, the following trigger-related explanations refer to muons only. The DT chambers provide track segements in the r-ϕ projections with p_T estimates and charge identification and hit patterns in η/z for the local trigger [1]. The CSC chambers offer three-dimensional track segments. In addition, all muon subsystems give timing information, i.e. they associate the segments and hit patterns to a bunch crossing independently from each other. At the regional level, the DT and CSC track finders join matching segments in the barrel and endcap regions and in the overlap region as well, where both detector types play a rôle. The DT and CSC track finders determine the p_T by comparing the slopes of track segments in successive layers of the muon system. The RPC trigger operates in parallel, providing independent track candidates and p_T estimates from pattern recognition in the range $|\eta| < 1.6$. All p_T estimates use a constraint on the interaction point (IP). Each of the DT and CSC track finders forwards the four highest-ranked muon candidates to the global trigger, the RPC forwards up to eight muon candidates, four from the barrel and four from the forward regions.
The information available for each muon candidate at the Global Muon Trigger (GMT) level is given in terms of: η and ϕ coordinates, p_T and charge, a measure of quality of the trigger reconstruction, isolation and MIP information from the Regional Calorimeter Trigger (RCT). The GMT starts with the matching based on the candidates' spatial coordinates. First barrel and endcap RPC candidates are matched with DT and CSC candidates. In the overlap regions, DT and CSC candidates are matched. After the spatial matching, the kinematic properties are compared. The muon candidates' tracks are propagated to the calorimeter and isolation and MIP compatibility are assigned. The four top candidates ranked by p_T and quality are then passed to the Global Trigger. The GT runs algorithms for thresholds (p_T) or basic topologies and then forwards the trigger decision and the associated data to the data acquisition system for readout of the entire event.
The main contribution to the L1 accept trigger rate depends on the threshold applied. Below 5 GeV, most muons arise from decays of pions and kaons. Muons from heavy flavour decays dominate the transverse momentum range 5 GeV $\lesssim p_T^\mu \lesssim$ 35 GeV and beyond 35 GeV, most triggered muons arise from W decays.

3.1.3 HLT Algorithms for Muons

The HLT trigger is divided into two steps, the Level 2 reconstruction (L2) and Level 3 reconstruction (L3). This must not be confused with different trigger levels implemented in the trigger chain with different electronics/filter farms. Both reconstruction levels use the same processor

[1] Momentum thresholds and the ranking scheme used for the muon triggers are based on the transverse momentum p_T. An estimate of the entire momentum is not needed at trigger level.

farm, are fully software-based and can (in principle) be supplied with the entire information of the event. The L2 filter reduces the rate with an improved fit to the L1-seeded muon candidates from the muon system before the L3 filter involves data from the inner tracking detectors to form highest-resolution trigger objects with a reconstruction similar to what is used in the offline analysis. Both, the L2 and L3 reconstruction use Kalman-filter techniques (see Appendix B) and take the expected interaction of the muons with the detector material into account.
The L3 reconstruction starts from the L2 muon track. The track in the muon system with its uncertainties defines a η-ϕ volume in the tracker. The L3 reconstruction builds tracks within this volume starting from the inner layers of the tracker, where pairs or triplets of hits that are compatible with vertex constraints form (multiple) seeds. The L3 inner track reconstruction is performed inside-out, i.e. from the inner to the outer surface of the tracker. The reconstructed inner track with the best χ^2 test statistic is chosen.

3.2 Reconstruction

The standard offline reconstruction of muons in CMS is briefly reviewed. The basics of the reconstruction also apply to the HLT online reconstruction. The reconstruction of the missing transverse energy, which is vital in $W \to l\nu$ analyses is discussed in more detail in Chapter 6.

3.2.1 Kalman Filtering Technique

An introduction to Kalman Filtering techniques is given in [42].
Muons are detected by tracking detectors. In general, track reconstruction starts from a number of simultaneous hits (with the same BX assigned) in one or multiple detector units. Even if the reconstruction of a given track is restricted to a limited detector volume, high track multiplicities and overlapping tracks, decay of charged particles (kinks), noise hits, the finite detector resolution and the interaction between the measured particle and the detector material turn the reconstruction of tracks into a complex problem that can yield ambiguous results. In order to get the best estimate of the track parameters possible and to avoid ambiguities, tracking algorithms have to include several sources of information, such as:

- A set of n measurements $\{m_k\}$, $0 < k < n$ that can consist of the raw hits or pre-reconstructed track segments in the different detector layers.
- Knowledge of the covariance matrix associated with the measurements, taking into account the different resolutions of different detector components that are considered in the track-finding process.
- A precise magnetic field map.
- The detailed material distribution along the particles' track and the expected interaction of the (assumed) particle type.

Further details on Kalman filtering are summarized in Appendix B.

3.2.2 Muon Reconstruction

The muon reconstruction algorithms in CMS are described in [38]. In CMS, the state vector for muon reconstruction is given by $\{x, y, \partial(x)/\partial(z), \partial(y)/\partial(z), q/|\vec{p}|\}$ at a reference surface (layer) $z = z_r$. Different types of system equations (propagators, Equation B.6) are employed differing in speed, precision and flexibility. For the modelling of the detector material in the muon system, the detector volume is divided into magnetic and non-magnetic volumes according to the map of the magnetic field. A magnetic volume is assigned the constant density of iron, a non-magnetic volume a constant density of 5.6% of the iron density. This forms the basis for the assumptions on energy loss and multiple scattering included in the propagator. The standard muon reconstruction differentiates three kinds of muons.

The Stand-alone Muon

The stand-alone (SA) muon reconstruction relies on the hits in the muon system. It starts with a seed state that consists of one (or a pattern of) track segment(s) found in the muon chambers. This seed state is propagated to the innermost layer of the muon system with a matching segment. In a second step, the pre-filter, an inside-out reconstruction is applied to refine the original seed. Then the actual filter is run and the new seed state is propagated outside-in again. Both the pre-filter and the filter are based on the Kalman filtering technique. The filtering is divided into the following steps:

- Finding the next layer with matching segments (navigation).
- Propagating the state vector to this layer (prediction).
- Selection of the best measurement/segment, which is based on the increment of the χ^2 associated with this segment.
- Determination of the new state vector $\boldsymbol{p_{k|k}}$ (filtering).

In the pre-filter step, the full segments reconstructed in the individual chambers are used. The final filter resolves the measurement down to the hit level, allowing for hits to be excluded from the fit that originally belonged to the ad hoc reconstructed segments. The χ^2 cut used by the final filter is tighter than that used by the pre-filter. As a first step of fake track rejection, only tracks with at least two measurements, one of which has to be fired in the DTs or CSCs, are accepted. After this track building, the trajectory is extrapolated to the point of closest approach to the beam line with a loose constraint on the nominal interaction point applied. This improves the momentum estimate. The result is a *stand-alone* muon track.

The Global Muon

The muon momentum resolution is improved significantly by including the track from the silicon tracking detectors (*tracker track*) into the reconstruction, especially for muons with low momenta, $p_T < 200$ GeV, where the resolution in the muon system is dominated by multiple scattering.
The matching of the tracker track with the stand-alone muon is performed in two steps: First a η-ϕ region of interest with origin at the vertex is defined in the tracker, which is opened around the extrapolated direction of the SA muon. Candidate matches are required to lie in this region and have a minimum transverse momentum $p_T > 60\%\ p_T^{\mathrm{SA}}$. In a second step, the SA muon and the candidate tracks are propagated to a common surface. The comparison of a tracker track to the SA muon at this surface is performed with discriminators based on the state vectors of the tracks at the common surface. Both the optimal choices of the common surface (outer tracker hit layer, inner muon hit layer) and the discriminator (spatial coordinates or momentum coordinates only or both) depend on the muon p_T. Cuts on the discriminators reduce the number of tracker track candidates in the region of interest. The decision on one *global muon* track is performed in a global refit of silicon and muon hits for all candidate tracker tracks. Removal of hits is possible in the global refit. After the fit, the track with the best χ^2 is chosen.

The Tracker Muon

The *tracker muon* is especially useful when dealing with very low-momentum muons ($p_T \lesssim 10$ GeV) that tend to leave low-quality signals in the muon system (for example only first station hit). It starts from tracks in the silicon detectors above a (low and adjustable) momentum threshold and performs a loose match to information in the calorimetry and the muon system.

In the following analyses the selected muons are required to pass both the *global* and the *tracker muon* requirement, i.e. all the reconstruction steps described above must have been passed.

Chapter 4

Signal Selection

After the reconstruction of muon candidates, further cuts on the quality of the reconstructed objects have to be applied in order to achieve optimal purity and efficiency for the signal. The muon identification cuts used are described and the impact of the selection is illustrated by some example distributions. Before turning to the selection and plots a short overview of the input for the analysis is in order.

4.1 Data Processing and Software Setup

The computing infrastructure behind the data analysis of the LHC experiments is the LHC Computing Grid [28, 41]. Within the computing structure of CMS [43] three main data formats are used.

- The **RAW** data format contains the full detector data and results from the trigger.
- The **RECO** data format contains the objects that result from the event reconstruction.
- The **AOD** data format is a reduced form of the RECO format. It includes all the higher-level physics objects that are needed for conventional physics analyses. The AOD format is used for the analyses in this thesis.

The CMS software `CMSSW` [44] comprises services needed by the simulation, calibration and alignement, and reconstruction modules that process event data. The physics analyses start from this structure.
In order to further reduce the event content stored in the samples that are used for the analysis and stored locally, it is convenient to use a so-called skimmer, which accesses the original RECO or AOD data files and writes the information needed for the specific analysis in flat `ROOT` [45] trees. The skimmer used for this work is part of the `ACSUSYAnalysis` analysis software framework [46] developed and maintained by Dr. Carsten Magass.
The analysis code used in the following analyses has been written by the author (in particular no electroweak analysis code in `CMSSW` has been used), except for the code for PDF reweighting that has been written by Dr. Carsten Magass.

4.2 Datasets and Simulated Samples

The `CMSSW` version used for the following analyses is `CMSSW_3_9_7`. The analyses are based on the entire set of certified data recorded by the CMS detector at a center-of-mass energy of $\sqrt{s} = 7$ TeV in 2010. The certified data has been taken in runs of the LHC accelerator during which all the subdetectors of CMS were working properly (the so-called 'Muon Physics' certified data ignoring the calorimeters has not been used). The run range extends from run 136035 to run 149294. This data corresponds to an integrated luminosity of $L = 36.1$ pb^{-1}.
The original data is split into *Primary Datasets*, which separate physics objects according to HLT

triggers. The exact names of the datasets are summarized in Table 4.1.

Description	Name
muon triggered sample 2010A	/Mu/Run2010A-Dec22ReReco_v1/AOD
muon triggered sample 2010B	/Mu/Run2010B-Dec22ReReco_v1/AOD
electron triggered sample 2010B	/Electron/Run2010B-Dec22ReReco_v1/AOD
photon triggered sample 2010B	/Photon/Run2010B-Dec22ReReco_v1/AOD

Table 4.1: Datasets used in the analysis. The electron and photon data is only relevant for a cross-check of the muon trigger efficiency in Section 5.2.3.

The Monte Carlo (MC) simulated samples are taken from the official CMS production (Fall 2010 [47]). They have been generated either with PYTHIA 6.4 [48] or with POWHEG [49], [50] interfaced with PYTHIA. The POWHEG method provides a way to interface a next-to-leading-order calculation in QCD (NLO) with a parton-shower event generator like PYTHIA. The detector simulation is performed with GEANT4 [51]. Simulated samples with multiple proton-proton interactions per bunch-crossing (pileup) and without are used and compared in the context of missing transverse energy studies in Chapter 6. The simulated samples are summarized in Table 4.2.
The QCD sample starts from a simulation of minimum bias events with a cut on the transverse momentum of the outcoming partons in the hard interaction $\hat{p}_T > 20$ GeV. Then a muon filter defined by the conditions $p_T^\mu > 15$ GeV and $|\eta^\mu| < 2.5$ is applied. The cross section reported in Table 4.2 includes the corresponding filter efficiency.
Higher-order QCD calculations are used as a point of reference for the inclusive cross sections of the electroweak processes. They are taken from [52] and reported in Table 4.3. For the samples that are not included in the table, the cross section for the normalization is taken from Table 4.2.

Process	Generator	Cuts at gen. level	N_{events}	σ [pb]	PDF
$W^+ \to \mu\nu$	POWHEG	-	~ 2 Mio	5775	CT10
$W^- \to \mu\nu$	POWHEG	-	~ 2 Mio	3944	CT10
$W \to \mu\nu$	PYTHIA	-	~ 5 Mio	7899	CTEQ6L1
$Z/\gamma^* \to \mu\mu$	POWHEG	$M_{\mu\mu} > 20$ GeV	~ 2 Mio	1614	CT10
$Z/\gamma^* \to \mu\mu$	POWHEG	no QED FSR, $M_{\mu\mu} > 20$ GeV	~ 2 Mio	1614	CT10
$Z/\gamma^* \to \mu\mu$	PYTHIA	$M_{\mu\mu} > 20$ GeV	~ 2 Mio	1300	CTEQ6L1
$W^+ \to \tau\nu$	POWHEG	-	~ 2 Mio	5775	CT10
$W^- \to \tau\nu$	POWHEG	-	~ 2 Mio	3944	CT10
$Z/\gamma^* \to \tau\tau$	POWHEG	$M_{\tau\tau} > 20$ GeV	~ 2 Mio	1614	CT10
Incl. μ QCD	PYTHIA	$\hat{p}_T > 20$ GeV, $p_T^\mu > 15$ GeV, $\lvert\eta^\mu\rvert < 2.5$	~ 10 Mio	84680	CTEQ6L1
$t\bar{t}$	PYTHIA	-	~ 1 Mio	94.3	CTEQ6L1
WW	PYTHIA	-	~ 2 Mio	27.8	CTEQ6L1
WZ	PYTHIA	-	~ 2 Mio	10.4	CTEQ6L1
ZZ	PYTHIA	-	~ 2 Mio	4.3	CTEQ6L1

Table 4.2: Monte Carlo simulated samples used in the analysis. The cross sections are taken from [47]. Whenever theoretical input is needed in the following, the processes are normalized to the NNLO/NLO cross sections summarized in Table 4.3. For the W and Z POWHEG samples in the list both samples with and without simulated pileup are used except for the $Z/\gamma^* \to \mu\mu$ sample without FSR that has been used without pileup. The PYTHIA samples used do not include pileup.

Process	Cuts	Accuracy (pQCD)	σ [pb]
$W^+ \to \mu\nu$	-	NNLO	6152
$W^- \to \mu\nu$	-	NNLO	4286
$W \to \mu\nu$	-	NNLO	10438
$Z/\gamma^* \to \mu\mu$	$M_{\mu\mu} > 20$ GeV	NNLO	1666
$Z/\gamma^* \to \mu\mu$	60 GeV $< M_{\mu\mu} <$ 120 GeV	NNLO	972
$t\bar{t}$	-	NLO	158

Table 4.3: Reference cross sections used for the comparison of experimental results with theory and scaling [52].

4.3 Muon Identification

Before turning to the selection of muons in the W and Z analyses, some general remarks on muon identification are in order.
Reconstructed muon objects can be other particles like hadrons passing the HO and penetrating the muon system (*punch through*). The second type are real muons that can either originate from collisions or from cosmic rays (*cosmics*). The muons from collisions can be divided further into muons from particles decaying in flight and muons that were produced in the interaction of interest close to the vertex (*prompt muons*). Muons from decays-in-flight can be further divided into muons from heavy flavor decays (b, c, τ) and light flavor decays (mainly π, K). The selection of prompt muons is the task of muon identification. The main features of muon identification and studies of fake rates (not including cosmics) using simulations can be found in [53]. Studies of fakes and cosmics contamination based on collision data can be found in [54] and [37].

The first selection steps concern the trigger and kinematic variables:

- Muon selection on data requires a choice of muon triggers. For the selection in this section, the trigger requirement is a logical OR of the CMS HLT muon triggers HLT_Mu9, HLT_Mu11 and HLT_Mu15_v1 with transverse momentum thresholds of 9 GeV, 11 GeV and 15 GeV, respectively. This choice is driven by two considerations, high trigger efficiency in the kinematic regime where muons are selected and acceptable trigger rate, i.e. no prescale applied on the trigger. The triggers HLT_Mu9 and HLT_Mu11 have been prescaled since run 147196 and 148822, respectively[1]. The triggers used do not require the muon candidate to be isolated. For the selection in this section, the trigger is required at the event level instead of asking for a trigger match of each muon. In the selection of single- and di-muon events in the W and Z analyses, at least one of the muons is matched explicitly to a L3 trigger object.

- A transverse momentum cut of $p_T > 20$ GeV is applied. Such intermediate p_T muons typically pass the entire detector.

- The muon is required to be contained within the HLT trigger acceptance $|\eta| < 2.1$.

After the trigger requirement and phase space cuts the muon identification comes into play. Several muon ID classes have been defined in CMS [53]. The three main classes correspond to the different reconstructors introduced above, the stand-alone, tracker and global muons.

A number of selection cuts associated with the muon reconstruction and identification are applied. This set of cuts has been developped in the context of muon identification studies [53] and electroweak analysis by the CMS electroweak group (see for example [55]) in the first months of data taking. The cuts applied and their main physics effects are briefly reviewed.

[1] These numbers refer to the list of runs with data that is actually included in the analysis.

- The selected muons are required to pass both the global muon reconstruction and the tracker muon reconstruction. These reconstruction requirements reduce the contamination of the sample due to punch-through, decays-in-flight and mismatching between the tracker part and the track reconstructed in the muon system.
- At least one hit in the muon system must be included in the (final) global fit. This cut is effective against punch-through and decays-in-flight.
- At least one hit in the pixel detector and $\geqq 10$ hits in the tracker. Muon tracks from decays-in-flight tend to have less hits in the innermost detector layers than prompt muons.
- $\chi^2/ndf < 10$ on the combined track. Further reduction of decays in flight.
- The number of chambers in the global fit that contain matched track segments has to be > 1. This selction is effective against punch-through.
- A cut is applied on the impact parameter in the transverse plane with respect to the primary vertex, $|\mathrm{d0}| < 0.2$ cm. This cut is very loose for muons from collision events but effective against cosmics.

The p_T distribution of the leading muons (highest p_T in the event) after this selection is given in Figure 4.1. The distribution observed in data is reproduced by the simulated samples taken into account with maximal deviations of about 10% in the high-statistics region. The total numbers of events after the selection are reported in Table 4.4. The dominant contribution arises from QCD events, most of which are dijet events. Studies on the QCD background carried out in [37] show that the dominant contribution arises from B meson decays, followed by a charm component, decays-in-flight of light flavors and a punch-through component at the permille level. The latter is not included in the QCD sample used for this thesis. In the lower p_T region dominated by QCD,

process	N_{events}
QCD	771871
$W \to \mu\nu$	182882
$Z \to \mu\mu$	26835
$W \to \tau\nu$	8526
$Z \to \tau\tau$	1697
$t\bar{t}$	1098
MC total	992909
Data	901026

Table 4.4: Number of events after single-muon trigger and kinematic requirements reported above and the full set of muon reconstruction/identification criteria applied in the simulation and data.

the simulation overestimates the data. The main reason is an overestimated cross section for B meson production in PYTHIA [57], [58]. Furthermore, the single-muon trigger efficiency in data is smaller than expected by the simulation by about 3%, as shown in Chapter 5. The second-leading physics process contributing is $W \to \mu\nu$ which exhibits a Jacobian peak at $p_T \approx M_W/2 \approx 40$ GeV and exceeds the steeply falling QCD muon p_T spectrum for $p_T^\mu \gtrsim 40$ GeV. It is followed by $Z/\gamma^* \to \mu\mu$ which also shows a Jacobian peak. All other contributions involve steps beyond vector boson production and decay and peak at the chosen phase space boundary $p_T^\mu = 20$ GeV. The selection of pure $W \to \mu\nu$ and $Z/\gamma^* \to \mu\mu$ samples calls for further cuts that reject QCD events. A powerful selection criterion against QCD is the muon isolation. In QCD events, the muon is typically produced in jets, surrounded by other particles. This is not the case in $W \to \mu\nu$ events. The relative muon isolation I_{rel} used in this thesis is defined as the sum of the transverse track momenta in the tracker and the transverse energy deposits in the ECAL and HCAL in a

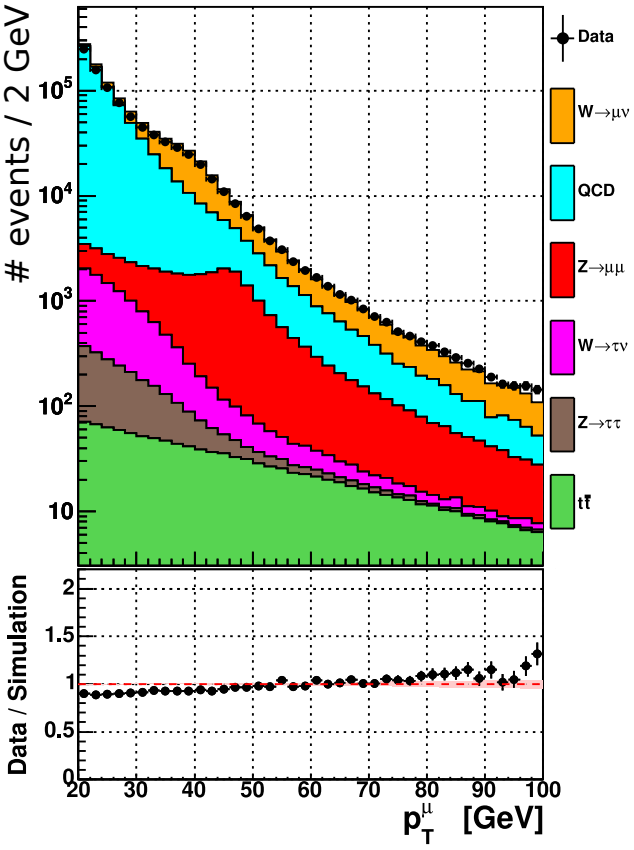

Figure 4.1: The p_T distribution of leading muons after single-muon trigger and kinematic requirements and the full set of muon reconstruction/identification criteria applied. The simulation does not include pileup.

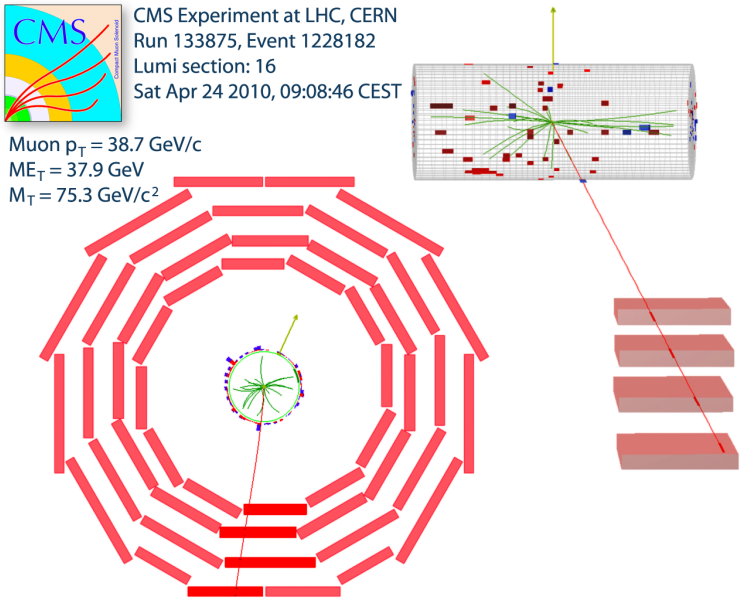

Figure 4.2: An isolated muon in the CMS detector (early W candidate event) [56].

cone around the muon divided by the muon momentum. The muon momentum itself is excluded from the sum. The cone sizes are $\Delta R = 0.3$ for the tracker and ECAL and $\Delta R = 0.4$ for the HCAL, with $\Delta R = \sqrt{(\Delta\eta)^2 + (\Delta\phi)^2}$ being the distance in η-ϕ space.

$$I_{rel} = \left(\sum_{Tracks} p_T + \sum_{ECAL} E_T + \sum_{HCAL} E_T \right) / p_T^{\mu} \tag{4.1}$$

The muon isolation is sensitive to the entire event topology in the cone around the muon. This includes tracks and energy deposits in the calorimetry due to pileup, multiple pp interactions in one bunch-crossing. Pileup is studied in the context of missing transverse energy $\not\!\!E_T$ in Section 6.2.2. The influence on the isolation variable is shown in Figure 4.3.

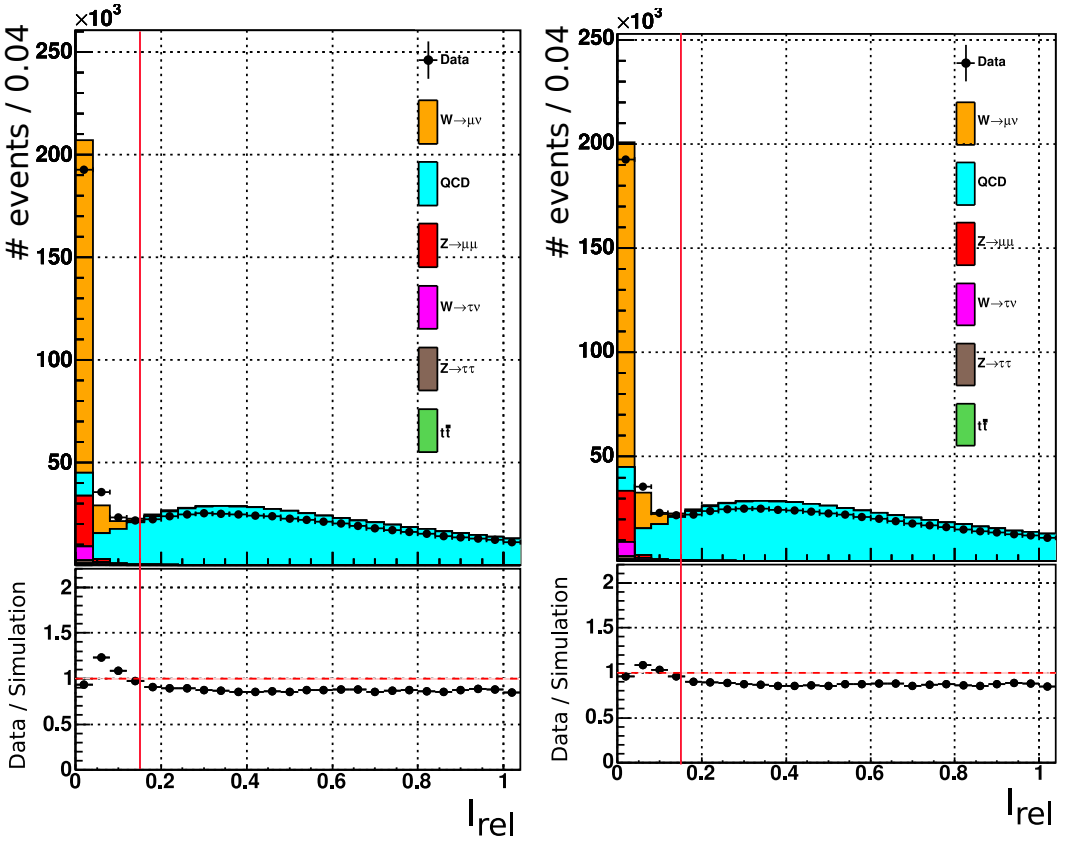

(a) $W \to \mu\nu$ simulated sample without pileup. (b) $W \to \mu\nu$ simulated sample including pileup.

Figure 4.3: Relative muon isolation I_{rel} after single-muon trigger and kinematic requirements reported above and the full set of muon reconstruction/identification criteria applied. The cut used in the analysis is marked by the red line.

The isolation provides a separation between the electroweak processes and QCD. The difference between data and simulation in the first bins is reduced when the simulation of the dominant contribution, $W \to \mu\nu$, includes pileup. The additional activity around the muon leads to a worse isolation. The remaining discrepancy of about 4% in the first bin is partly due to the different trigger efficiencies in data and simulation. A loose cut of $I_{rel} < 0.15$ is applied to all muons in the analysis. According to simulation, the efficiency of the isolation requirement is about 98% for muons from the signal processes $W \to \mu\nu$ and $Z \to \mu\mu$ and 7% for muons from QCD production. The angular distributions of the remaining muons are shown in Figure 4.4. The η distribution exhibits the structure of the muon system. It is discussed further in the context of the trigger efficiency in Section 5.2.4. The ϕ distribution is flat except for a few dips in the detector coverage.

In the following, a muon passing the kinematic, reconstruction, identification and isolation criteria mentioned in this section is referred to as a *tight* muon.

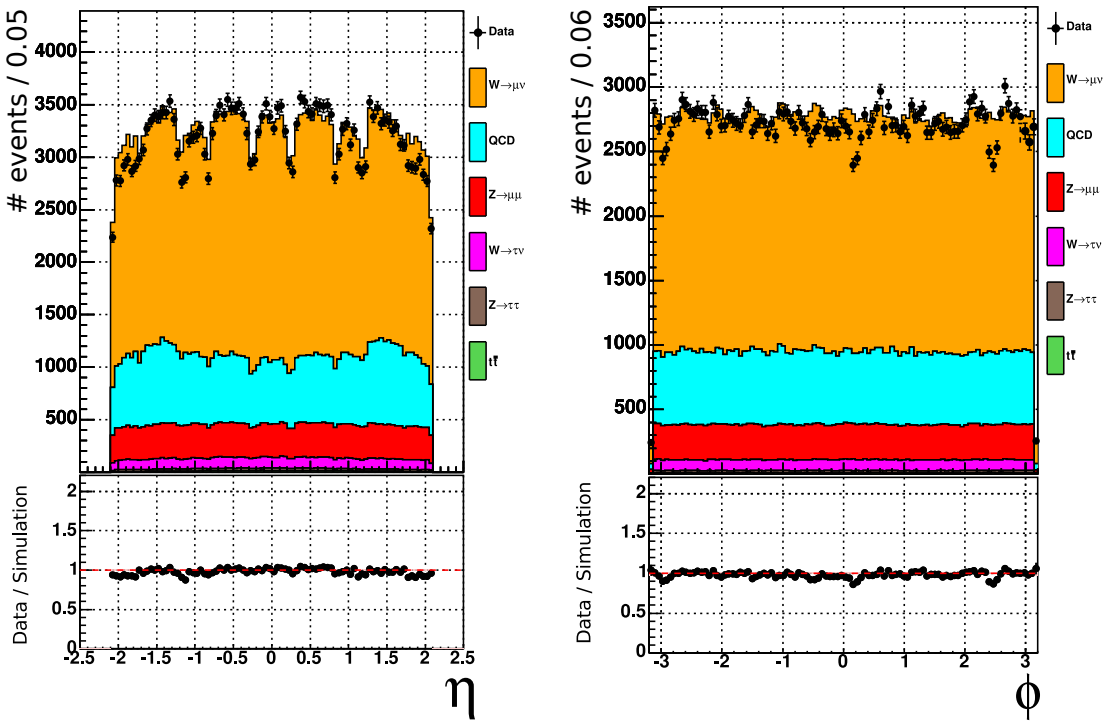

(a) η distribution.

(b) ϕ distribution.

Figure 4.4: Angular distributions after the full single-muon selection. The simulation does not include pileup.

4.4 Selection of $W \to \mu\nu$ Events

The $W \to \mu\nu$ selection calls for exactly one tight muon that is matched to a L3 trigger object within $|\Delta\phi| < 0.1$ and $|\Delta\eta| < 0.1$. In addition a Z/γ^* veto is applied by rejecting events with an additional global muon with $p_T^{\mu} > 10$ GeV. This veto rejects about 50% of the events passing all the other criteria in the $Z/\gamma^* \to \mu\mu$ simulated sample (including the exactly one tight muon requirement). In order to further reduce the QCD background, the muon transverse momentum cut is tightened to 25 GeV. No $\not\!\!E_T$-based cuts are applied. Since $\not\!\!E_T$ is a complicated variable that involves the entire event, it is discussed in a dedicated Chapter 6. The most important plots for the $W \to \mu\nu$ analysis, the M_T distributions for $W^{\pm}$ after data-driven corrections of the background, $\not\!\!E_T$ and the muon efficiencies are depicted in Figure 8.2. The resulting contribution of the selected sample is summarized in Table 4.5. 176357 data events pass the $W \to \mu\nu$ selection.

	N/N_{tot} W^+ [%]	N/N_{tot} W^- [%]
QCD	9.3	12.6
$t\bar{t}$	0.3	0.4
$Z \to \tau\tau$	0.4	0.6
$W \to \tau\nu$	2.5	2.5
$Z/\gamma^* \to \mu\mu$	3.0	3.7
$\sum$ non-QCD bkg	6.2	7.2
$W \to \mu\nu$	84.5	80.2

Table 4.5: Relative contribution of different processes in percent after $W^+ \to \mu\nu$ and $W^- \to \mu\nu$ selection as expected from simulation. Electroweak contributions are scaled to NNLO (NLO $t\bar{t}$) cross section. The number of QCD events is taken from the data-driven approach described in Chapter 7.

4.5 Selection of $Z/\gamma^* \to \mu\mu$ Events

$Z/\gamma^* \to \mu\mu$ events are selected by demanding two tight muons, one of which is matched to a L3 trigger object. The muons must carry opposite charge. In order to further suppress the photon component and mainly measure the Z, an invariant mass cut of 60 GeV $< M_{\mu\mu} <$ 120 GeV is used. The resulting background amounts to about 4 permille. The invariant mass of the dimuon system distribution before the cut on the invariant mass is shown in Figure 4.5. The Z peak observed in data is well reproduced by the simulation.
After the $Z/\gamma^* \to \mu\mu$ selection 12065 data events remain.

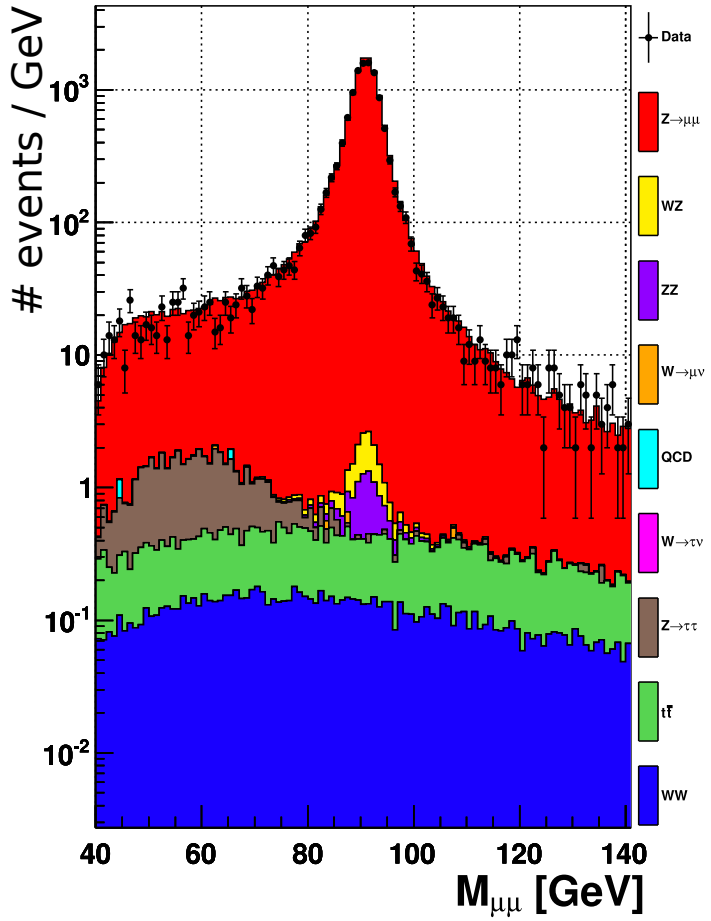

Figure 4.5: Invariant mass distribution of the dimuon system after the selection of two tight muons with opposite charge. The simulation does not include pileup.

Chapter 5

Acceptance and Efficiencies for Muons

In order to determine the cross section, the detector acceptance and efficiencies of the muon selection criteria have to be investigated. The detector acceptance can only be studied using simulated events, wheras efficiencies are evaluated on the data, allowing for a test of the reconstruction, identification and trigger efficiencies expected from simulation.

A comment on the statistical uncertainties reported in the following paragraphs is in order. Acceptances and efficiencies are usually defined as a subset of events or physics objects within a basic set that passes a set of selection criteria. The binomial distribution and associated uncertainties apply to this setup. As derived in [59] the asymmetric statistical uncertainty on the efficiency ϵ is given by:

$$\epsilon = \frac{m}{n} \tag{5.1}$$

$$\sigma_\epsilon^+ = \frac{2m+1}{2(n+1)} - \frac{m}{n} + \frac{1}{2n(n+1)}\sqrt{n^2(2m+1)^2 - 4n(n+1)m^2} \tag{5.2}$$

$$\sigma_\epsilon^- = \frac{m}{n} - \frac{2m+1}{2(n+1)} + \frac{1}{2n(n+1)}\sqrt{n^2(2m+1)^2 - 4n(n+1)m^2}\ . \tag{5.3}$$

For $m \gg 1$ this reduces to:

$$\sigma_\epsilon^+ \approx \sigma_\epsilon^- \approx \sigma_\epsilon \equiv \sqrt{\frac{m}{n^2}\left(1 - \frac{m}{n}\right) + \frac{1}{4n^2}}\ . \tag{5.4}$$

In the following this condition usually holds and the symmetric uncertainty is reported.

5.1 Acceptance Studies

The kinematic acceptance of the detector is defined as the fraction of signal events passing the η, p_T cuts applied to the physics objects under study in the event selection. It is studied on the full simulated signal samples without any preselection. The geometric acceptance is defined as the fraction of events passing the η cuts only, i.e. without requiring the events to pass the p_T cuts. The choice of the exact acceptance definition used depends on the theoretical calculation that the final experimental result is compared with. For example, theoretical calculations for the Drell-Yan cross section exist for several ranges in the dimuon invariant mass $M_{\mu\mu}$. Since the event topology of virtual photon exchange $\gamma^* \to \mu\mu$ does not differ from the process $Z \to \mu\mu$, the term Z cross section is not well defined. Even when other sources of background are considered to be reducible or otherwise accessible on the data itself, the measured cross section will always reflect the full $Z/\gamma^* \to \mu\mu$ process. The natural way of getting as close as possible to what is then called the Z cross section is to select an invariant mass range around the resonance where the contribution from

Z exchange is dominant. The theoretical calculation that the experimental result is compared to has to use the same invariant mass range.

The kinematic acceptance for the $Z/\gamma^* \to \mu\mu$ cross section determination is defined as:

$$A_Z = \frac{N\,(60\text{ GeV} < M_{\mu\mu} < 120\text{ GeV}\ \&\ p_T^{\mu} > 20\text{ GeV}\ \&\ |\eta^{\mu}| < 2.1)}{N\,(60\text{ GeV} < M_{\mu\mu} < 120\text{ GeV})}\ . \tag{5.5}$$

The cuts on the muon kinematics are applied to both muons. In order to include the effects of final state radiation that is included in the theoretical calculations in Table 4.3, the numerator is evaluated with the generated muons after final state radiation, whereas the denominator is evaluated with the muon momenta before final state radiation [60]. As illustrated in Figures 5.1 and 5.2, final state radiation is expected to affect mainly the $M_{\mu\mu}$ and p_T distributions, whereas the influence on η is insignificant. The invariant mass distribution of the dimuon pair is widened towards smaller values by final state radiation. The results on the acceptance for the Z/γ^*

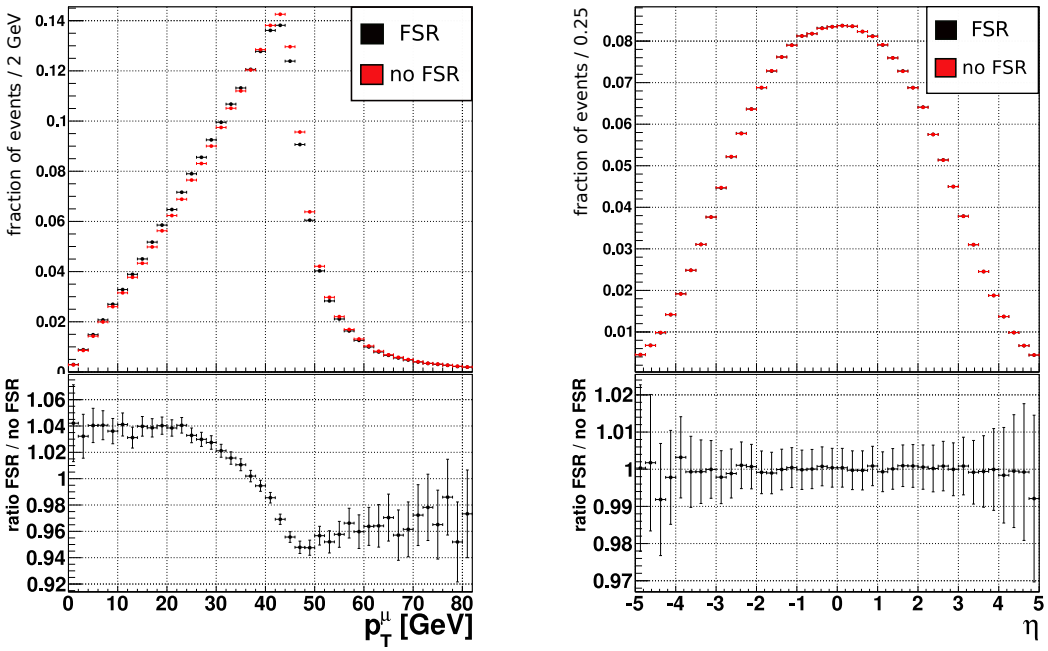

(a) p_T distribution.

(b) η distribution.

Figure 5.1: Comparison of the $Z/\gamma^* \to \mu\mu$ simulation with final state radiation (black) and without it (red). Both generated muons are included in the plots for events within 60 GeV $< M_{\mu\mu} <$ 120 GeV.

signal are reported in Table 5.1 with and without final state radiation. The effect of final state radiation evaluated on the signal sample simulated with POWHEG amounts to 2.6%, mainly due to the influence on the invariant mass. Only about 45% of the generated events have both muons within $|\eta| < 2.1$, i.e. the acceptance of the muon trigger. In the case of the $W \to \mu\nu$ signal, the complication of additional photon exchange is not given. The acceptance is therefore defined with respect to the full number of events in the sample. It is evaluated for both charges seperately:

$$A_{W^{\pm}} = \frac{N^{\pm}(p_T^{\mu} > 25\text{ GeV}\ \&\ |\eta^{\mu}| < 2.1)}{N^{\pm}_{tot}}\ . \tag{5.6}$$

The p_T and η distributions of the muons from W decay for different electric charge are shown in Figure 5.3. The muons from W^+ decay are produced more centrally than those from W^- decay.

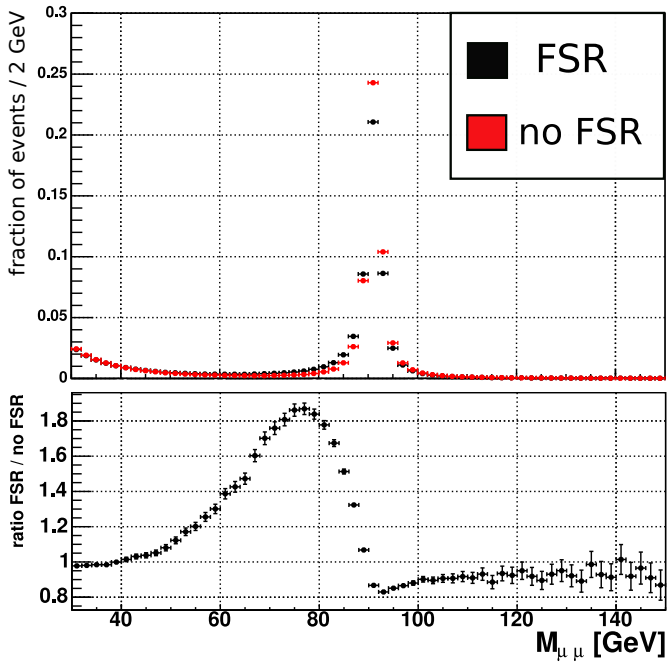

Figure 5.2: The invariant mass distribution of $Z/\gamma^* \rightarrow \mu\mu$ simulated dimuon pairs with (black) and without (red) final state radiation.

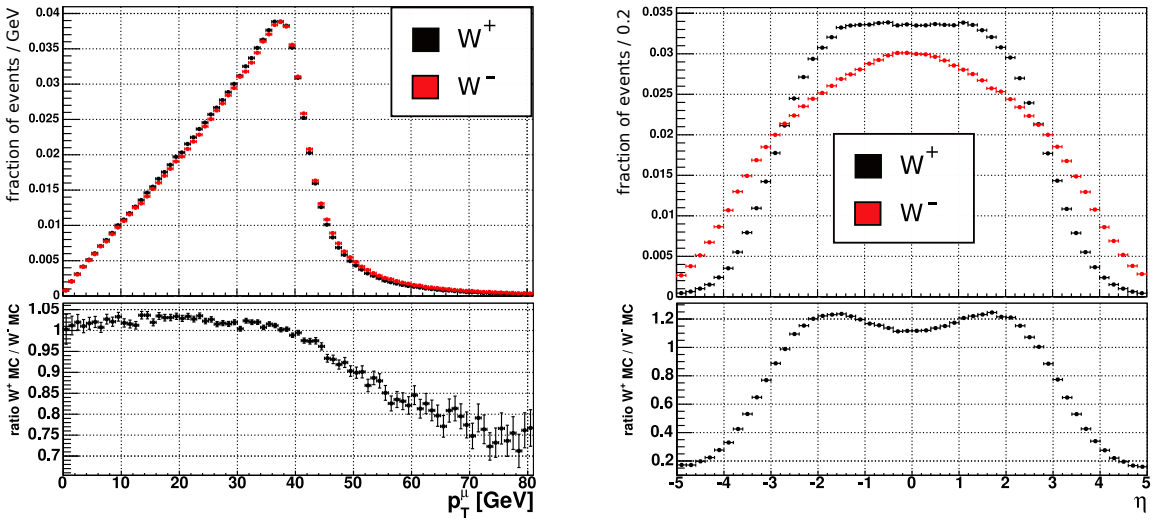

(a) p_T distribution.

(b) η distribution.

Figure 5.3: Distributions of kinematic variables of muons from W decay seperated by electric charge, plus (black) and minus (red). The seperation by charge is done at the generator level. Both distributions are normalized to the number of events in the sample.

Acceptance definition	Z
geometric without FSR	0.4470 ± 0.0005
geometric	0.4394 ± 0.0005
total kinematic without FSR	0.4106 ± 0.0005
total kinematic (A_Z)	0.4002 ± 0.0005

Table 5.1: Results for the geomtric and kinematic Z acceptances with and without final state radiation. Only the statistical uncertainties are included.

Therefore the geometric acceptances for the different electric charges differ by about 17%. After the p_T cut, this difference is reduced to about 2.7%, reflecting the correlation between p_T and η. The results for the acceptances for the $W^{\pm} \to \mu\nu$ signal are reported in Table 5.2. The acceptance

Acceptance definition	W^+	W^-
geometric	0.6925 ± 0.0003	0.5868 ± 0.0003
total kinematic without FSR	0.4706 ± 0.0004	0.4570 ± 0.0004
total kinematic	0.4594 ± 0.0004	0.4471 ± 0.0004

Table 5.2: Results for the geomtric and kinematic W acceptances for both electric charges. For the kinematic acceptance, the results with and without final state radiation are given. Only the statistical uncertainties are included.

for all W events is defined as a weighted mean of the charge dependent acceptances:

$$A_W = \frac{\sigma^{NNLO}_{W^+} A_{W^+} + \sigma^{NNLO}_{W^-} A_{W^-}}{\sigma^{NNLO}_{W^+} + \sigma^{NNLO}_{W^-}} = 0.4544 \pm 0.0003 \ . \tag{5.7}$$

5.1.1 Systematic Uncertainties on the Acceptance

The acceptance as defined above depends on the shapes of the p_T and η distributions of the muons from signal processes. These shapes and their uncertainties can be studied using integrator tools that perform calculations of both total and differential cross sections for certain interactions such as W/Z production or using Monte Carlo tools that simulate the entire event rather than the hard interaction only at the cost of some approximations[1]. The p_T and η distributions depend on the theory tools employed and the parton distribution functions (PDF) used in the calculation.
Before describing the determination of the systematic uncertainties on the acceptance, a brief summary of PDF fitting is given. More comprehensive introductions can be found in [61], [20].
Parton distribution functions (PDF) of the proton are extracted from a global fit to different sources of experimental data, most of which stem from DIS fixed target and HERA experiments. Because of the finite amount of data available, theoretical assumptions on the parameterization of the PDF which is fitted to the data have to be made. The chosen parameterization is fitted to the experimental data including the information on experimental uncertainties available. Different PDFs use different parameterizations and/or different sets of data on which the fit is performed. The data included is measured at different energy scales, or in terms of the variables needed as input for the PDF evaluation, at different factorization scales. The PDF fit result is then evaluated at some different factorization scale that characterizes the process under study. The evolution from one factorization scale to the other can be calculated in perturbative QCD using the DGLAP equations [11–13]. In the following, PDF sets that perform the necessary perturbative QCD calculations at NLO are used with the NLO generator POWHEG. The treatment of theoretical

[1]For example the resummation carried out by the PYTHIA parton shower that is interfaced with the POWHEG generator used for the Monte Carlo signal simulation includes only the resummation of the leading logarithmic terms (LL).

uncertainties like the uncertainty due to the choice of parameterization, QCD and electroweak contributions not considered, the choice of input data and others cannot not be treated in an objective way. However, the experimental uncertainties can be propagated to observables which depend on the PDFs. One method to treat the experimental uncertainties entering the PDF fit, called the Hessian method, is used in the following. Its description is given in Appendix C including some nomenclature used in the following.

The simulated Monte Carlo sample is generated with the central PDF of the NLO CT10 PDF set by the CTEQ group [62]. The event weights w_{event} are defined as the ratio of the new error PDF member S_i over the original central PDF S_0 evaluated at the same momentum fractions $x_1,\ x_2$ of the incoming partons and the same factorization scale $\mu_F \equiv {M_{W,Z}}^2$:

$$w_{event}^{S_i} = \frac{x_1\ f_{S_i}\left(x_1, M_{W,Z}\right) \cdot x_2\ f_{S_i}\left(x_2, M_{W,Z}\right)}{x_1\ f_{S_0}\left(x_1, M_{W,Z}\right) \cdot x_2\ f_{S_0}\left(x_2, M_{W,Z}\right)} \ . \tag{5.8}$$

The reweighted acceptance for a given PDF member S_i is given by the ratio of the sum of weights over all events in the sample after and before acceptance cuts.

$$A_{W,Z}^{S_i} = \frac{\sum_{j=1}^{N_{events}} w_{event}^{S_i,\ j}\ \text{(passing acceptance cuts)}}{\sum_{j=1}^{N_{events}} w_{event}^{S_i,\ j}\ \text{(before acceptance cuts)}} \ . \tag{5.9}$$

For the original central PDF S_0, with $w_{event}^{S_0} = 1$, this reduces to the Formulae 5.5 and 5.6. The reweighting approach allows for both a reweighting of the central PDF to other member PDFs of the same PDF set and a reweighting to an entirely different PDF set.

The information on the different PDFs is accessed via the LHAPDF interface [63]. It is stored in so-called grid files that store pre-calculated tables for the PDFs. An interpolation between these fixed values allows for the evaluation of the PDFs at the desired values. The systematic uncertainty on the acceptance due to the experimental errors on the PDF are studied with the CT10 PDF set [62]. Moreover, an uncertainty associated with the choice of parameterization is estimated by comparing the acceptance results obtained with the central PDFs of three different NLO PDF sets, the baseline choice CT10 [62], the MRST PDF set MSTW08 NLO [20] and HERAPDF1.0 [64]. The latter involves data from $e^{\pm}p$ scattering only, whereas the other two include other sources of data relevant for PDF fitting as well, for example measurements performed at TEVATRON. The CT10 PDF set includes 53 member PDFs ($2n+1$), the MSTW08 set includes 41 and the HERAPDF1.0 set 21. The desired uncertainty on the acceptance is the one evaluated at 68% confidence level (CL). According to [62], the tolerance $T \equiv \sqrt{\Delta\chi^2}$ used for the definition of the CT10 PDF members $S_i^{\pm}$ corresponds to 90% CL. The MSTW08 set is available in LHAPDF for different confidence levels and according to [64], the HERAPDF1.0 set is created for 68% CL. Therefore the uncertainty on the acceptance obtained from Equations C.10, C.11 and C.12 have to be reduced from 90% CL to 68% CL in the case of the CT10 PDF set. According to [20], the manifest assumption of multiplying the uncertainty obtained with the 90% CL PDF set by a factor of $\sqrt{T_{68\%}^2/T_{90\%}^2} = \sqrt{1/2.71} \approx 0.61$ is not appropriate for global PDF analyses. Therefore, the following practical approach is used: For the three signal samples $Z \to \mu\mu$, $W^{\pm} \to \mu\nu$ the uncertainty on the acceptance is evaluated using the MSTW08 PDF sets for 68% CL and 90% CL and the resulting factor between the two results is then propagated to the CT10 results at 90% CL. The factors vary between 0.47 and 0.56 in reasonable proximity to the simple expectation 0.61. The results on the acceptance for the different central PDFs are given with the systematic uncertainties in Table 5.3. The uncertainties associated with the experimental uncertainties on the PDF evaluated with the CT10 PDF set amount to $\lesssim 1\%$.

[2] The momentum fractions $x_1,\ x_2$ are correctly stored in the POWHEG Monte Carlo simulated samples. However, the energy scale for each event is set to the transverse momentum of the vector boson, which is not a good choice for the factorization scale. This is changed to the vector boson mass.

	A_Z	ΔA_Z	A_{W+}	ΔA_{W+}	A_{W-}	ΔA_{W-}
CT10 90% CL	$0.4002^{+0.0073}_{-0.0056}$	0.0061	$0.4594^{+0.0060}_{-0.0045}$	0.0050	$0.4471^{+0.0081}_{-0.0076}$	0.0075
CT10 scaled to 68% CL	$0.4002^{+0.0041}_{-0.0029}$	0.0033	$0.4594^{+0.0033}_{-0.0022}$	0.0026	$0.4471^{+0.0038}_{-0.0038}$	0.0037
MSTW08 NLO 90% CL	$0.4013^{+0.0036}_{-0.0053}$	0.0042	$0.4587^{+0.0027}_{-0.0045}$	0.0034	$0.4521^{+0.0057}_{-0.0058}$	0.0054
MSTW08 NLO 68% CL	$0.4014^{+0.0020}_{-0.0027}$	0.0023	$0.4587^{+0.0015}_{-0.0022}$	0.0018	$0.4519^{+0.0027}_{-0.0029}$	0.0027
HERAPDF1.0 68% CL	$0.3961^{+0.0018}_{-0.0052}$	0.0030	$0.4554^{+0.0035}_{-0.0061}$	0.0047	$0.4478^{+0.0048}_{-0.0072}$	0.0056

Table 5.3: Results on the signal acceptances for different central PDFs. The acceptances are shown with the asymmetric systematic uncertainties according to C.11 and C.12. In addition, the symmetric uncertainty $\Delta A_{W,Z}$ is given.

	ΔA PDF data [%]	ΔA parameter [%]	ΔA_{tot} $+1\%$ $(W^{\pm})$ $+1.6\%$ (Z) [%]
Z	0.82	0.51	1.87
W^+	0.57	0.44	1.23
W^-	0.83	0.54	1.41

Table 5.4: Summary of uncertainties on the acceptance. The total uncertainty is the quadratic sum of the uncertainty from the PDF data input, the uncertainty due to the choice of parameterization and an additional 1% (1.6%) uncertainty due to sources not studied above.

In Figure 5.4 and 5.5, the relative variation of the η distribution is shown for the individual CT10 member PDFs with respect to the central PDF for the W^- and Z signals, respectively. In the central region, the uncertainty on the shape is about $\approx$ 1% in both cases. The PDF systematic uncertainty due to the choice of the prameterization is estimated as half the maximal difference between the central CT10 result and the other two 68% CL values for the acceptance reported in Table 5.3. It is of the same order as the uncertainty associated with the data input of the PDF fit. Other sources of systematic uncertainties on the acceptance not studied here, such as uncertainties associated with initial state radiation, higher-order QCD effects, final state radiation, electroweak contributions and the α_s PDF uncertainty are given in [65] and found to be of the order of 1% for W^+/W^- and 1.6% for Z when added in quadrature.
The systematic uncertainties on the acceptance discussed above are reported in Table 5.4. For the total uncertainty, another 1% (1.6%) is added in quadrature to roughly include the uncertainties neglected.
A W simulated sample including both charges is built from the W^+ and W^- samples by adding them accroding to the theoretical expectation for the W^+/W^- charge ratio. This procedure is justified by the experimental result on the W^+/W^- charge ratio reported in Chapter 8 that is in agreement with the theory. The systematic uncertainty on the acceptance for the full W sample is evaluated in the same fashion as described above. The results are summarized in Table 5.5. Both the systematic uncertainty derived from the PDF sets and the uncertainty due to the parameterization are smaller in the case of the full W compared to W^+/W^-.
The measurement of the W^+/W^- and W/Z cross section ratios involves the acceptance ratios A_{W-}/A_{W+} and A_Z/A_W. The systematic uncertainties on these ratios are summarized in Table 5.6, with the additional systematic uncertainties of $\approx 1.5\%$ for A_{W-}/A_{W+} and $\approx 2\%$ for A_Z/A_W from [65].

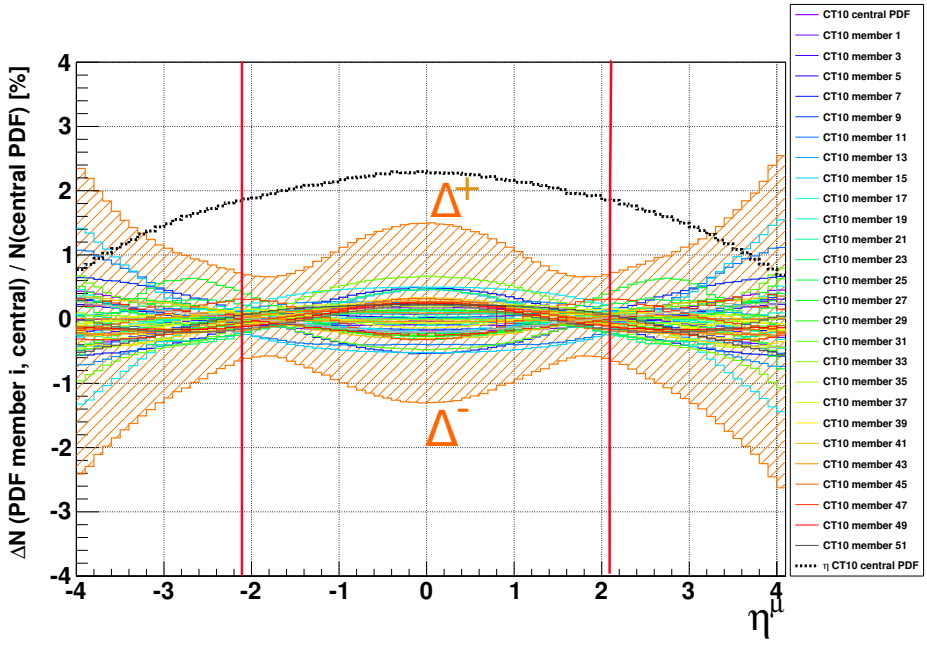

Figure 5.4: Relative variation of the η distribution of generated muons for the individual CT10 member PDFs with respect to the central PDF for the $W^- \to \mu\nu$ signal in percent. For the total variation Δ^+, Δ^- (orange) the individual contributions are summed up as prescribed in Equations C.11 and C.12. The shape of the η distribution of the muons is shown in black for orientation. The red lines mark the acceptance cut.

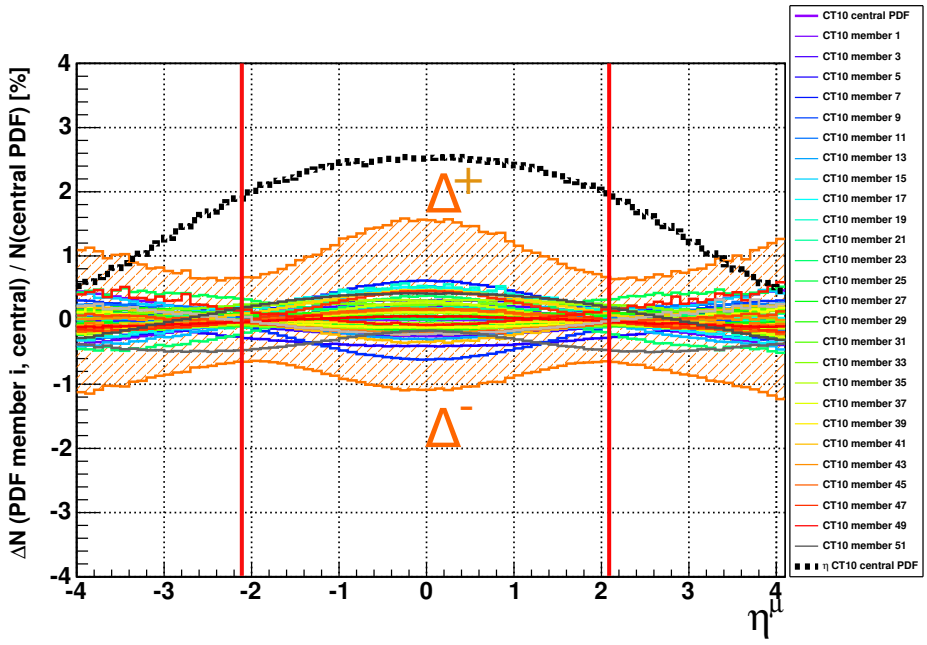

Figure 5.5: Relative variation of the η distribution of generated muons for the individual CT10 member PDFs with respect to the central PDF for the $Z \to \mu\mu$ signal in percent. For the total variation Δ^+, Δ^- (orange) the individual contributions are summed up as prescribed in Equations C.11 and C.12. The shape of the η distribution of the muons is shown in black for orientation. The red lines mark the acceptance cut.

	A_W	ΔA_W PDF data [%]	ΔA_W parameter [%]	$\Delta A_{W,tot}$ + 1% [%]
W	0.4544 ± 0.0003 (stat)	0.24	0.23	1.1

Table 5.5: Summary of uncertainties on the acceptance for the W sample comprising both charges. The total uncertainty is the quadratic sum of the uncertainty from the PDF data input, the uncertainty due to the choice of parameterization and an additional 1% uncertainty due to sources not studied above.

	R_A ± (stat)	ΔR_A data [%]	ΔR_A par [%]	$\Delta R_{A,tot}$ + 1.5% $\left(\frac{A_{W-}}{A_{W+}}\right)$ + 2% $\left(\frac{A_Z}{A_W}\right)$
$\frac{A_{W-}}{A_{W+}}$	0.973 ± 0.001	0.9	0.9	2.0
$\frac{A_Z}{A_W}$	0.881 ± 0.001	0.5	0.3	2.1

Table 5.6: Summary of uncertainties on the acceptance ratios for the W^+/W^- and W/Z cross section ratio measurements in percent. The total uncertainty is the quadratic sum of the uncertainty from the PDF data input, the uncertainty due to the choice of parameterization and an additional 1.5% (2%) uncertainty due to sources not studied above.

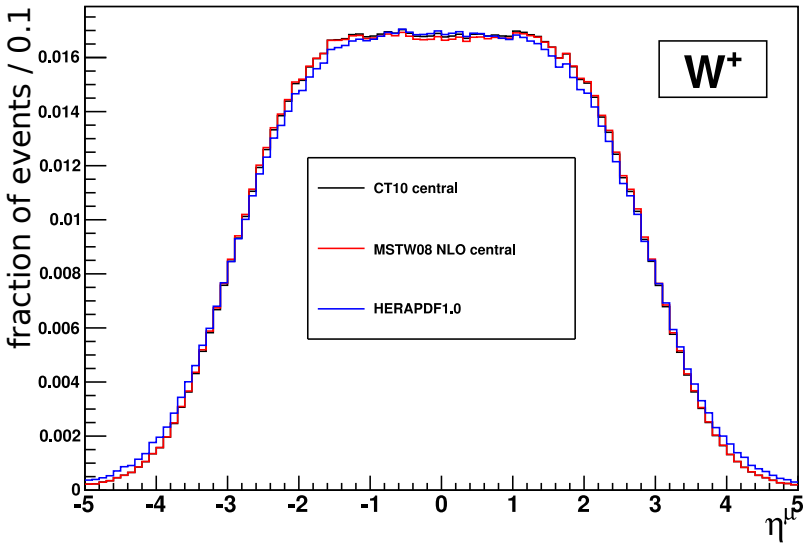

Figure 5.6: Comparison of the η distribution of generated muons for the CT10 (black), MSTW08 (red) and HERAPDF1.0 (blue) central PDFs.

5.2 Efficiencies

5.2.1 Definitions

In contrast to the simulation where cut efficiencies can be examined starting from the generated particle of interest that arises from the hard interaction and testing for a matching reconstructed object with the property under study, efficiencies determined on data are evaluated on a basic set of events that has to be selected by applying trigger, reconstruction and identification criteria. Thus, there is no simple way of deriving the 'absolute' efficiency for a given criterion as there is on a simulated sample.
Once a basic set of events and the corresponding physics objects under study that are used for the efficiency determination are obtained, the efficiency of a selection criterion ϵ^{sel} is given by:

$$\epsilon^{sel} = \frac{N\,(\text{objects satisfying the selection criterion})}{N\,(\text{all objects in the basic set})} \; . \tag{5.10}$$

In the following, the total selection efficiency for a single muon ϵ_μ with the selection criteria discussed in Chapter 4 is divided into reconstruction, isolation and trigger efficiencies:

$$\epsilon_\mu = \epsilon_{Reco}\;\epsilon_{Iso}\;\epsilon_{Trig} \tag{5.11}$$

$$\epsilon_{Reco} = \epsilon_{Glb}\;\epsilon_{Trk}\;\epsilon_{ID}\;. \tag{5.12}$$

The order in which the different factors are shown reflects the different choice of muons in the basic set for each efficiency. The global muon reconstruction efficiency is defined as the fraction of muons satisfying the global muon reconstruction out of all muon candidates within the acceptance:

$$\epsilon_{Glb} = \frac{N_\mu\,(\text{Global \& } |\eta| < 2.1 \text{ \& } p_T > 20 \text{ GeV})}{N_\mu\,(\;|\eta| < 2.1 \text{ \& } p_T > 20 \text{ GeV})} \; . \tag{5.13}$$

The tracker muon requirement is then tested on a set of muons that fulfill the global muon requirement, so it corresponds to the conditional propability of the tracker reconstruction under the assumption of global reconstruction:

$$\epsilon_{Trk} = \frac{N_\mu\,(\text{Tracker \& Global \& } |\eta| < 2.1 \text{ \& } p_T > 20 \text{ GeV})}{N_\mu\,(\text{Global \& } |\eta| < 2.1 \text{ \& } p_T > 20 \text{ GeV})} \; . \tag{5.14}$$

In the same fashion of conditional propabilities, the identification efficiency ϵ_{ID} is determined on muon candidates accepted by both the global and tracker muon reconstruction algorithms, the isolation efficiency is evaluated on well reconstructed objects including all identification criteria used for selection and the trigger efficiency is based on well reconstructed, isolated muons.

5.2.2 The Tag and Probe Method

The muons of interest are muons from W and Z decays. Under the assumption that the two muons from Z decays are uncorrelated and that the hadronic activity in W and Z events is similar, the efficiencies used in $W \to \mu\nu$ analyses can be obtained from a sample of $Z \to \mu\mu$ events by reweighting the efficiencies as a function of η and p_T to the muon kinematics in $W \to \mu\nu$ events. Selecting dimuon events in a sufficiently small invariant mass window around the Z peak allows for a clean selection of the muons of interest, even if the full set of selection criteria is only applied to one of the muons. Therefore, efficiencies can be studied on the data without severe influence of muons from background processes such as QCD dijet events that have a different event topology than the muons of interest (for example more activity around the muons and lower isolation efficiency).
The concept of the tag-and-probe (TP) method is depicted in Figure 5.7.

The basic set of events is given by dimuon events which satisfy the following criteria:

- The dimuon system falls in the invariant mass range 60 GeV $< M_{\mu\mu} <$ 120 GeV.

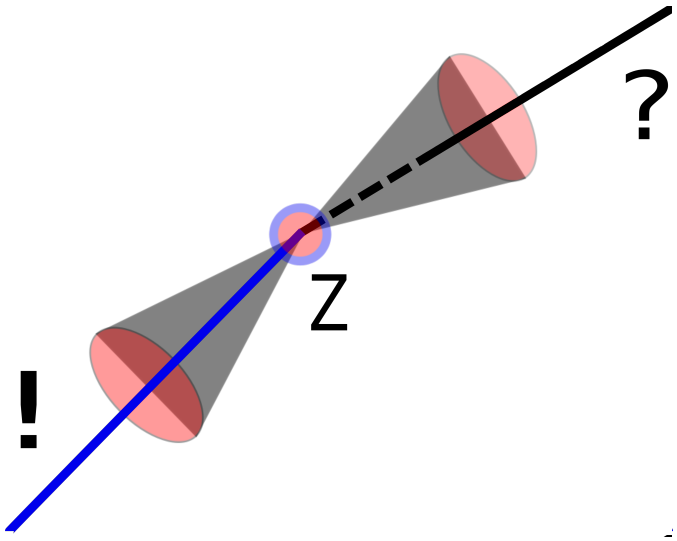

Figure 5.7: Concept of the tag-and-probe method: In dimuon events with invariant mass around the Z peak, one high quality muon is selected (tag) to ensure a low background level and the other muon is tested for the selection criterion under study (probe).

- The two muons carry opposite electric charge.
- At least one of the muons passes all selection cuts described in Section 4 and is matched to a HLT trigger object (*tag*).
- The second muon lies within the acceptance ($|\eta| < 2.1,\ p_T > 20$ GeV).

After this selection, the events are by construction divided into two classes. In the first class, only one muon fulfills the entire set of cuts and serves as the *tag* muon for the *probe* muon, which fails the selection at some point. In this case, only the *probe* muon enters in the efficiency determination. When testing it for a given selection requirement, the *probe* can either fall into the *fail* or *pass* category. The second class of events consists of events where both muons fulfill the tag requirement. In this case they serve as tags for each other and both muons enter the efficiency determination.

A muon from the basic set N^μ can either pass or fail a given selection step:

$$N^\mu = N^\mu_{pass} + N^\mu_{fail}\ . \tag{5.15}$$

Two different categories of muons pass the selection cut, the tag muons N^μ_{tag} and the muons which pass this selection but fail at a different one $N^\mu_{pass-no-tag}$. The efficiencies for the different muon categories are given by [59]:

$$\epsilon_{pass} = \frac{N^\mu_{pass}}{N^\mu} \tag{5.16}$$

$$\epsilon_{tag} = \frac{N^\mu_{tag}}{N^\mu} \tag{5.17}$$

$$\epsilon_{pass-no-tag} = \frac{N^\mu_{pass-no-tag}}{N^\mu} = \frac{N^\mu_{pass} - N^\mu_{tag}}{N^\mu} = \epsilon_{pass} - \epsilon_{tag} \tag{5.18}$$

$$\epsilon_{fail} = \frac{N^\mu_{fail}}{N^\mu} = \frac{N^\mu - N^\mu_{pass}}{N^\mu} = 1 - \epsilon_{pass}\ . \tag{5.19}$$

The total number of Z events in the basic set N^Z can be divided into events with two *tag* muons N^Z_{TT}, one *tag* muon and a passing *probe* muon N^Z_{TP} and one *tag* muon plus a failing *probe*

muon N^Z_{TF}. Assuming that the two muons are uncorrelated, these numbers are linked with the single-muon efficiencies by:

$$N^Z_{TT} \sim N^Z \cdot \left(\epsilon^\mu_{tag}\right)^2 \tag{5.20}$$

$$N^Z_{TP} \sim 2N^Z \cdot \epsilon^\mu_{tag}\epsilon_{pass-no-tag} = 2N^Z \cdot \epsilon^\mu_{tag}\left(\epsilon^\mu_{pass} - \epsilon^\mu_{tag}\right) \tag{5.21}$$

$$N^Z_{TF} \sim 2N^Z \cdot \epsilon^\mu_{tag}\epsilon_{fail} = 2N^Z \cdot \epsilon^\mu_{tag}\left(1 - \epsilon^\mu_{pass}\right) \ . \tag{5.22}$$

In terms of the numbers of events in the three event categories, the single-muon selection efficiency ϵ_{pass} can then be written as:

$$\epsilon_{pass} = \frac{2N^Z_{TT} + N^Z_{TP}}{2N^Z_{TT} + N^Z_{TP} + N^Z_{TF}} \ . \tag{5.23}$$

The tag-and-probe method is subject to the following limitations:

- The cuts for the choice of the basic set are to some extend correlated with the efficiencies under study. The resolution of kinematic quantities such as the muon momentum for example depends on the quality of the muon reconstruction, i.e. the muon identification cuts which the muon passes or fails.

- The tag-and probe method is not sensitive to effects which influence both muons in a correlated way. One example for an event topology with such behaviour is final state radiation by one of the muons in events with a boosted Z which emits both muons into a small solid angle. In this case, the isolation values of the two muons are not uncorrelated.
  Pre-triggering, i.e. the assignment of a wrong bunch crossing to a trigger object, is another effect which is not accounted for by the tag-and-probe method.

5.2.3 Global Efficiencies

The determination of the global efficiency values[3] is based on formula 5.23. Therefore the remaining background contributions in the *tag-tag* category and the *pass* and *fail* categories for each set of selection criteria have to be estimated.
The invariant mass distribution of the *tag-tag* and *tag-no-tag* categories are shown in Figure 5.8. The fits of the simulated signal shapes to these distributions provide χ^2/ndf values of 0.97 and 1.33 for the *tag-tag* and *tag-no-tag* categories, respectively. The overall effect of background contamination on the evaluation of the efficiencies is therefore expected to be small -in agreement with the expectation from simulation- and the set of cuts applied is tight enough to allow for the selection of a pure set of $Z \to \mu\mu$ events.

The number of events in each category, fit results and relevant information from the simulation are collected in Table 5.7. The expected ratio of background to signal ranges from 0.3% in the *tag-tag* category to 8.7% in the *tag-fail* category of the global muon reconstruction requirement. Extended likelihood fits [66] of the simulated signal shape to the data are performed for every category with ROOFIT [67] [4]. In the case of the fail categories, an additional two parameter fit (N_{sig}, N_{bkg}) including a background contribution modelled by a second degree polynomial is carried out. Due to the limited statistics in the simulation, the choice of the background function is not well-defined. The results obtained with lower order polynomials agree with the second order polynomial within the statistical uncertainties of the fit. In the *tag-fail* category of the tracker muon reconstruction requirement, with only 67 entries in data, the fit without background contribution does not converge and therefore no results are given in Table 5.7. As an example,

[3] The global efficiency value is the overall efficiency after integrating over the muon distribution in phase space. The efficiencies as functions of p_T and η are discussed in Section 5.2.4.

[4] For fits with only one normalization parameter, the result of the extended likelihood fit is just a scaled distribution.

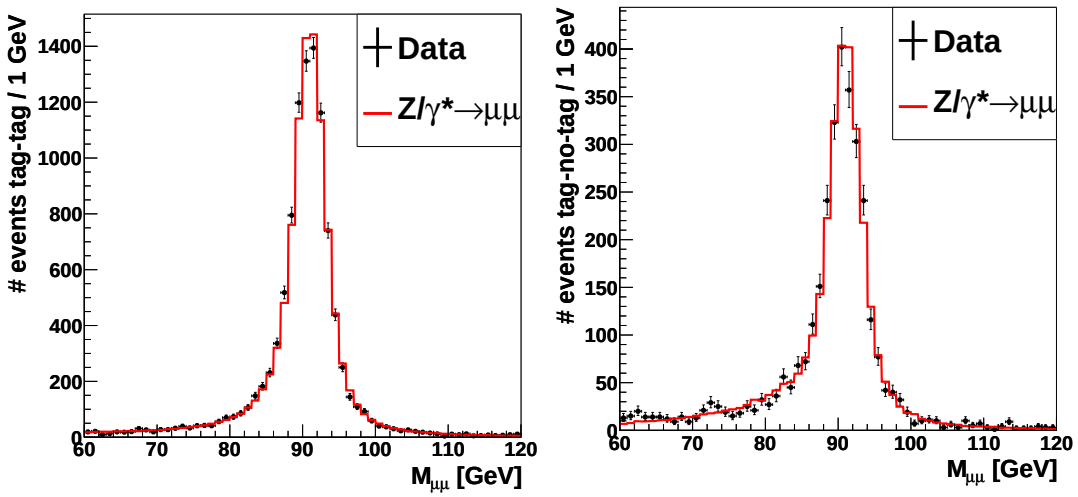

(a) Invariant mass in the *tag-tag* category.

(b) Invariant mass in the *tag-no-tag* category.

Figure 5.8: Invariant mass distribution of the two muons in the *tag-tag* and *tag-no-tag* categories in data (black) and simulation (red). The simulated distributions are fitted to the data.

the fits to the *tag-fail* category of the global muon reconstruction requirement with and without background are shown in Figure 5.9.
The choice of the simulated distribution as templates for the fit instead of the more general, simulation independent relativistic Breit-Wigner shape folded with a Gaussian is explained by asymmetries of the expected signal shapes due to final state radiation (FSR). Since the combined isolation includes contributions from FSR photons in the ECAL, the broadening of the invariant mass distributions to values smaller than M_Z is most significant in the *tag-fail* category of the isolation requirement. The corresponding fit result is depicted in Figure 5.10. Final state radiation is one source of correlation between the two muons from Z decay in the case of boosted Z bosons that eject both muons into a small solid angle.

A cross-check on the number of background events obtained from the fit is possible by using a same-sign (SS) background estimate. For this purpose, the same categories are used but the opposite electric charge requirement in the event selection is replaced by asking for same-sign dimuons. As reported in Table 5.7, the ratio of same-sign to opposite sign (OS) events is about 50% in most categories for the background, while it ranges from 1.3% down to 0.02% for the signal. The suppression of the signal allows for a better access to the background contribution.
The number of same-sign background events N_{SS}^{bkg} is estimated as:

$$N_{SS}^{bkg} \simeq N_{SS}^{data} - N_{OS}^{data} \cdot \left(\frac{N_{SS}^{sig}}{N_{OS}^{sig}} \right)_{MC} . \tag{5.24}$$

And the number of background events in the opposite sign case is given by:

$$N_{OS}^{bkg} \equiv N_{SS}^{bkg} \cdot \left(\frac{N_{OS}^{bkg}}{N_{SS}^{bkg}} \right)_{MC} . \tag{5.25}$$

The above formulae assume that the SS/OS ratio is correctly predicted by the simulation for both the signal and background and that the background contamination in the opposite sign case is small. The statistical significance of the same-sign background estimation is limited by the small statistics in the same-sign categories.
The number of background events obtained from the simulation scaled to the number of observed

category	N_{data}^{OS}	N_{fit}^{signal}	N_{fit}^{bkg}	χ^2_{fit}/ndf	$\left(\frac{N_{bkg}}{N_{sig}}\right)$ [%]	N_{data}^{SS}	$\frac{N_{bkg}^{SS}}{N_{bkg}^{OS}}$ [%]	$\frac{N_{sig}^{SS}}{N_{sig}^{OS}}$ [%]
TT	10320	10319 ± 102	-	0.97	0.3 ± 0.0	0	-	-
TnoT	3216	3216 ± 57	-	1.33	2.7 ± 0.1	75	-	-
TP Glb	2846	2807 ± 70	-	1.24	2.1 ± 0.1	37	61 ± 5	0.038 ± 0.007
TF Glb	370	370 ± 19	-	1.11	8.7 ± 0.7	38	67 ± 8	0.72 ± 0.01
		301 ± 21	69 ± 14	0.70				
TP Trk	2779	2779 ± 53	-	1.24	1.8 ± 0.1	28	52 ± 5	0.022 ± 0.006
TF Trk	67	-	-	-	7.7 ± 0.7	9	97 ± 15	0.30 ± 0.09
TF Trk		43 ± 8	24 ± 7	0.26				
TP ID	2275	2275 ± 48	-	1.37	2.0 ± 0.1	23	51 ± 5	0.021 ± 0.006
TF ID	504	504 ± 22	-	0.60	1.1 ± 0.1	5	56 ± 14	0.029 ± 0.015
TF ID		472 ± 24	32 ± 12	0.48				
TP Iso	1745	1745 ± 42	-	0.88	0.26 ± 0.02	0	-	-
TF Iso	530	530 ± 23	-	0.78	6.4 ± 0.4	23	56 ± 6	0.07 ± 0.02
TF Iso		498 ± 29	32 ± 18	0.74				
TF Trig	1745	1745 ± 42	-	0.88	0.26 ± 0.02	0	-	-

Table 5.7: The numbers of opposite-sign dimuon events in data N_{data}^{OS}, fitted signal and background events N_{fit}^{signal} and N_{fit}^{bkg}, the ratio of signal to background events expected from simulation $\left(\frac{N_{bkg}}{N_{sig}}\right)_{MC}$ and the numbers of same-sign dimuon events in data N_{data}^{SS}. The number of same-sign events expected from simulation includes the signal $Z \to \mu\mu$, $W \to \mu\nu$, $Z \to \tau\tau$ and $t\bar{t}$ samples that are scaled to NNLO and NLO, respectively. The muon-enriched QCD sample is scaled to the cross section used for production with PYTHIA. The fit results including the χ^2_{fit}/ndf are given for fits of the signal shape extracted from simulation. For the fail categories, where the background contamination is expected to be most important, a second fit including a second degree polynomial background shape is performed. Note that there is no *tag-pass* category for the trigger criterion by construction.

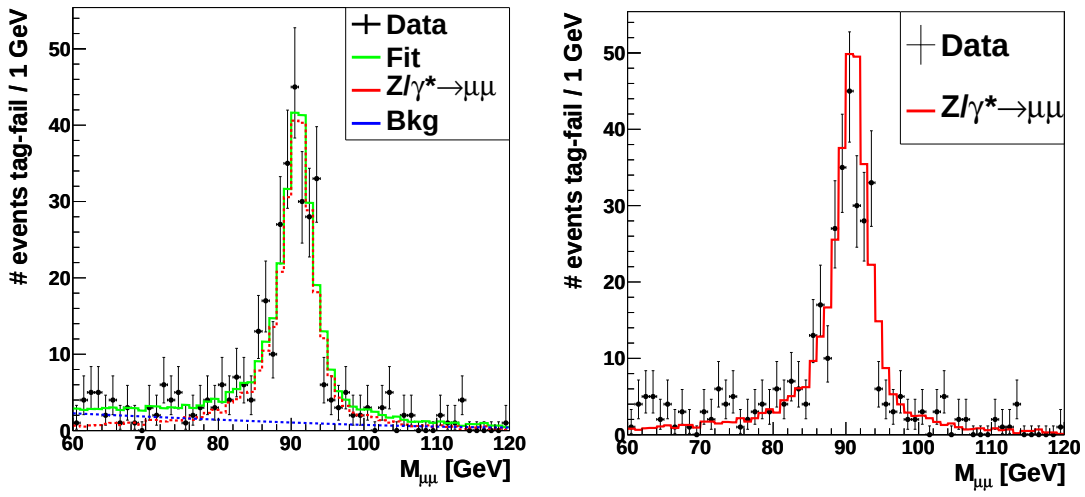

(a) Fit to *tag-fail* category with signal and background shapes.

(b) Fit to *tag-fail* category with signal shape.

Figure 5.9: Fits to the *tag-fail* category for the global muon reconstruction requirement with the signal shape only and a combined fit of signal and background shapes. The background is modelled by a second degree polynomial.

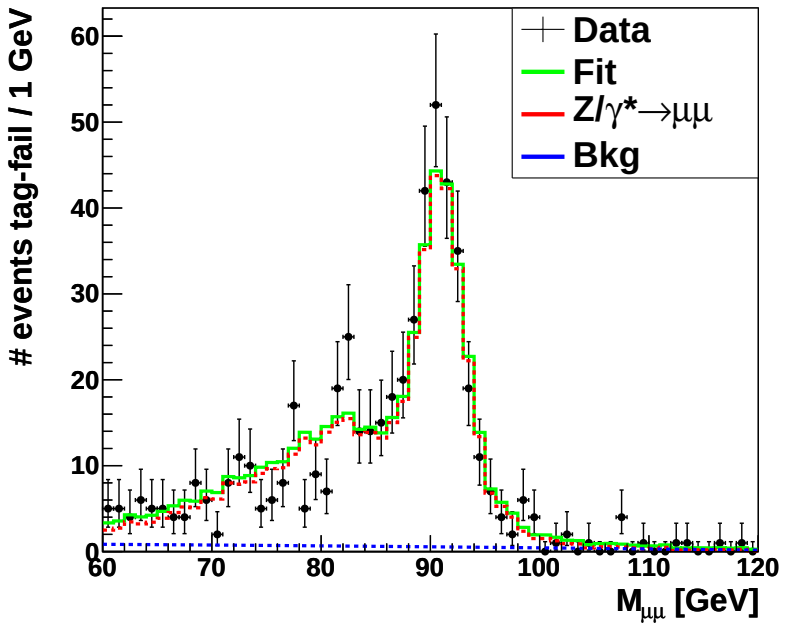

Figure 5.10: Fits to the *tag-fail* category for the isolation requirement with the signal and background contributions. The broadening of the signal shape due to final state radiation is reproduced by the simulation.

events in data, the same-sign method and the background fit are compared in Table 5.8. The partly simulation-driven same-sign background estimation agrees very well with the expected background from simulation in the *tag-pass* categories. In the *tag-fail* categories the same-sign method exceeds the simulation by factors ranging from 1.3 to 1.9, the difference lies within one to two standard deviations of the statistical uncertainties. This excess can be explained considering that the QCD background is not scaled with a k-factor accounting for higher orders than included by PYTHIA and that not all possible sources of background are included. The same-sign background estimate ensures that the impact of backgrounds not included in the used Monte Carlo samples, which have a similar SS/OS ratio as the background considered, is small. A comparison of the background estimates from simulation and the same-sign method with the fits performed in the *tag-fail* categories suggests that the fit results yield an upper limit on the number of background events in these categories.

	N_{OS}^{bkg}			
category	MC	SS method	fit	N_{OS}^{data}
TP Glb	58.6 ± 2.9	58.9 ± 11.1	-	2846
TF Glb	29.6 ± 2.7	56.3 ± 11.4	69 ± 14	370
TP Trk	49.1 ± 4.2	52.7 ± 11.4	-	2779
TF Trk	4.8 ± 0.7	9.1 ± 3.4	24 ± 7	67
TP ID	44.6 ± 2.4	44.2 ± 10.4	-	2275
TF ID	5.5 ± 0.6	8.7 ± 4.5	32 ± 12	504
TP Iso	4.5 ± 0.4	-	-	1745
TF Iso	32.0 ± 2.3	40.4 ± 9.6	32 ± 18	530

Table 5.8: Comparison of background estimates for the different categories obtained from simulation (MC), the same-sign method (SS) and the fit described above, which is only used in four *tag-fail* categories.

The global muon efficiencies are evaluated according to Equation 5.23. The numbers of events in the *tag-tag*, *tag-pass* and *tag-fail* categories are corrected for the small background contributions by the following scheme: In the case of the *tag-tag*, the *tag-pass* category of the isolation and the *tag-fail* category of the trigger requirement with expected background levels below 5 permille and not a single event in the same-sign distributions, the background estimate is obtained from simulation. In the other categories, the same-sign estimate is used. In order to give a systematic uncertainty on the efficiencies associated with the background, Formula 5.23 is evaluated without background contributions as well and the difference is taken as the systematic uncertainty.

selection criterion	ϵ_{data} no Bkg subtraction	ϵ_{data} Bkg subtraction	$\lvert\Delta\epsilon\rvert$
global muon reconstruction	0.9845 ± 0.0008	0.9868 ± 0.0007	0.0023
tracker muon reconstruction	0.9971 ± 0.0003	0.9975 ± 0.0003	0.0004
muon identification	0.9785 ± 0.0009	0.9787 ± 0.0010	0.0002
muon isolation	0.9769 ± 0.0010	0.9785 ± 0.0010	0.0016
muon trigger	0.9220 ± 0.0018	0.9220 ± 0.0018	–
product	0.8652 ± 0.0022	0.8693 ± 0.0022	0.0041

Table 5.9: Result of the tag and probe method with and without the subtraction of background in the different categories.

The influence of the background and the corresponding systematic uncertainty on the efficiencies can be reduced by tightening selection cuts. As shown above, the cuts in this analysis lead to a very tight selection of Z events. Since the Z cross section is high considering the LHC luminosity one year after startup, this selection has been used rather than optimizing the cuts towards an optimal signal efficiency.

On the simulated sample for the signal, systematic uncertainties arising from the choice of the basic set in the context of the tag and probe method can be estimated. In general, the comparison of the single muon efficiencies from a matching of the reconstructed muons to generated muons from the hard interaction and the tag and probe method performed on the signal Monte Carlo serves as a closure test of the tag and probe approach (and the corresponding code). In the following paragraph, the efficiencies evaluated with the generator information are referred to as generator efficiencies ϵ_{gen} and the efficiencies from tag and probe are named ϵ_{TP}.

The evaluation of the generator efficiencies starts from reconstructed muon pairs within the acceptance. The reconstructed muons have to come from a Z decay. The basic set is composed of all the muons selected. Then the efficiencies are evaluated as in the case of tag and probe like in Equation 5.14. They are compared to the efficiencies from tag and probe evaluated on the same-signal Monte Carlo in Table 5.10. The agreement is very good and verifies the implementation of the method.

selection criterion	ϵ_{gen} MC	ϵ_{TP} MC
global muon reconstruction	0.9910 ± 0.0001	0.9909 ± 0.0001
tracker muon reconstruction	0.9952 ± 0.0001	0.9951 ± 0.0001
muon identification	0.9830 ± 0.0001	0.9832 ± 0.0001
muon isolation	0.9811 ± 0.0001	0.9811 ± 0.002
muon trigger	0.9514 ± 0.0002	0.9515 ± 0.0002
product	0.9048 ± 0.0003	0.9050 ± 0.0003

Table 5.10: Comparison of efficiencies derived from the $Z/\gamma^* \to \mu\mu$ simulated sample using the generator information about muons from the Z/γ^* decay and the tag and probe method.

With regard to the separate selection of $W^+ \to \mu^+\nu$ and $W^- \to \mu^-\nu$, the efficiencies are

determined depending on the charge of the muon. Since the muons in the dimuon system are forced to carry opposite sign, Formula 5.23 reduces to:

$$\epsilon^{\pm}_{pass} = \frac{N_{TT} + N^{\pm}_{TP}}{N_{TT} + N^{\pm}_{TP} + N^{\pm}_{TF}} \ . \tag{5.26}$$

The efficiencies for both electric charges are reported in Table 5.11 along with the result derived on the the full set of muons. No background subtraction is applied here, the influence is expected to be $\lesssim 1\%$ due to the results of the background estimation given above. The signal Monte Carlo sample has been tested to show no difference between the single muon efficiencies for different charges within the statistical uncertainty.

selection criterion	ϵ_{data}	ϵ_{data} positive charge	ϵ_{data} negative charge
global muon reconstruction	0.9845 ± 0.0008	0.9846 ± 0.0011	0.9844 ± 0.0011
tracker muon reconstruction	0.9971 ± 0.0003	0.9979 ± 0.0004	0.9964 ± 0.0006
muon identification	0.9785 ± 0.0009	0.9790 ± 0.0013	0.9779 ± 0.0014
muon isolation	0.9769 ± 0.0010	0.9762 ± 0.0014	0.9776 ± 0.0014
muon trigger	0.9220 ± 0.0018	0.9236 ± 0.0025	0.9205 ± 0.0026
product	0.8652 ± 0.0022	0.8672 ± 0.0031	0.8632 ± 0.0031

Table 5.11: Results of the tag and probe method for the full set of selected muons and separated by muon electric charge.

The estimate of background contributions and the comparison at generator level only point to systematic effects smaller than 5 permille. However, biases due to correlated effects between the two muons and effects of variations in the choice of the basic set are not included.

Trigger efficiency

The trigger efficiency determined via tag and probe can be cross-checked with a selection of well reconstructed and isolated muons on a data sample based on triggers orthogonal to the muon triggers, i.e. triggers that obtain their main input from a different subdetector than the muon system. The ECAL does not play a rôle for the muon triggers used (HLT_Mu9, HLT_Mu11 and HLT_Mu15_v1 do not employ the isolation information available for muon triggering). Therefore the correlation between the electron and photon triggers that start from ECAL information is expected to be small and a muon trigger efficiency determination on such data samples is expected to be almost unbiased.
Primary datasets rely on pure HLT trigger bits associated with the desired objects. For the early run period, RunA, there is one primary dataset based on both electron and photon triggers, `/EG/Run2010A-Dec22ReReco_v1` , whereas in the case of later RunB there are separate samples `/Electron/Run2010B-Dec22ReReco_v1` and `/Photon/Run2010B-Dec22ReReco_v1` . In the RunA run period about 9% of the total integrated luminosity of 36.1 pb^{-1} was taken. Due to the changes in both the electron and photon trigger prescales and the muon trigger efficiency with increasing luminosity, a correct determination of the trigger efficiency with the orthogonal trigger method including all the data taken in the 2010 run is a complex task. Therefore, the cross check of the muon trigger efficiency is performed on the RunB data only without taking into account the muon trigger efficiency variations with the correct weight of each luminosity section according to the prescales of electron/photon triggers.
Muons are selected on the electron and photon triggered data samples by applying the entire list of kinematic reconstruction and identification cuts plus isolation. The comparison with the trigger efficiency from tag and probe given above is performed with muons in the corresponding kinematic range only, i.e. $p_T > 20$ GeV.

The comparison of the efficiencies for the kinematic range $p_T > 20$ GeV is presented in Table 5.12. The result for the electron triggered data sample is found to agree with the result from tag and probe within the statistical uncertainties, however the result for the photon triggered sample is about 2% lower than the result from tag and probe. A systematic uncertainty of 1.5% is assigned to the trigger efficiency.

	orthogonal triggers electron	orthogonal triggers photon	tag and probe
$\epsilon_{trigger}$	0.9153 ± 0.0058	0.9018 ± 0.0067	0.9220 ± 0.0018

Table 5.12: Comparison of data-driven approaches for trigger efficiency determination. The RunB data is split into two datasets with electron and photon triggers and values are provided for both cases. Only the statistical uncertainty is reported.

The trigger efficiency from tag and probe with the probe muon passing all selection criteria except for the trigger requirement and a relaxed p_T cut applied is shown as a function of p_T in Figure 5.11.

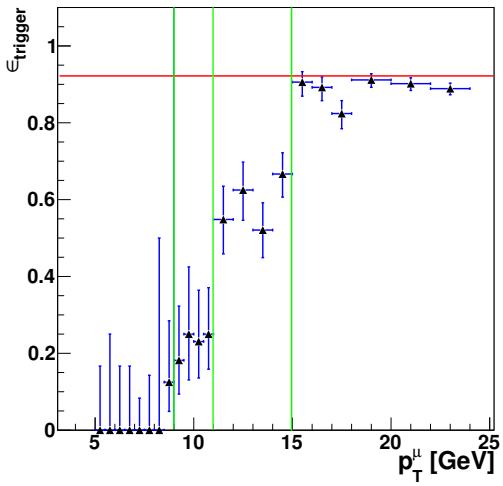

Figure 5.11: Trigger efficiency derived with the tag and probe method on data as a function of muon p_T. The method is disfavoured statistically in the kinematic range studied here. Due to the low statistics in the tag and probe case, the asymmetric binomial uncertainties (Equations 5.2, 5.3) are used. The efficiency shown includes the trigger prescales. The red line indicates the global trigger efficiency from tag and probe in the kinematic range $p_T > 20$ GeV. The green lines indicate the muon trigger p_T thresholds at 9 GeV, 11 GeV and 15 GeV.

The orthogonal trigger method is favoured statistically in the low muon p_T range due to the hard p_T spectrum for muons from Z events. However, the tag and probe method is based on the selection of Z events and therefore yields trigger efficiency results from different luminosity sections with the correct weight in the overall efficiency determination for p_T ranges where a trigger without prescale is active. The HLT trigger efficiency shown here is defined as the fraction of muons matched to a L3 muon trigger object, i.e. it is not corrected for the trigger prescales applied to HLT_Mu9 and HLT_Mu11 as of runs 147196 and 148822, respectively[5]. The HLT p_T thresholds are visible as steps. For $p_T > 15$ GeV the trigger efficiency is well-defined because the HLT_Mu15_v1 trigger path, activated in run 147196 associated with the HLT_Mu9 prescale, is not prescaled and the combination of the three triggers allows for unprescaled coverage over the full

[5]These numbers refer to the list of runs with data that is actually included in the analysis.

amount of data. The trigger efficiency in this region is in agreement with the result from tag and probe for $p_T > 20$ GeV.

5.2.4 Efficiency Distributions

Efficiencies binned in η and p_T of the muon are obtained on the data and the Z/γ^* simulation using the tag and probe method. Since the background contamination has been shown to be small in the context of the global efficiencies in Section 5.2.3, it is not taken into account for the efficiency distributions.

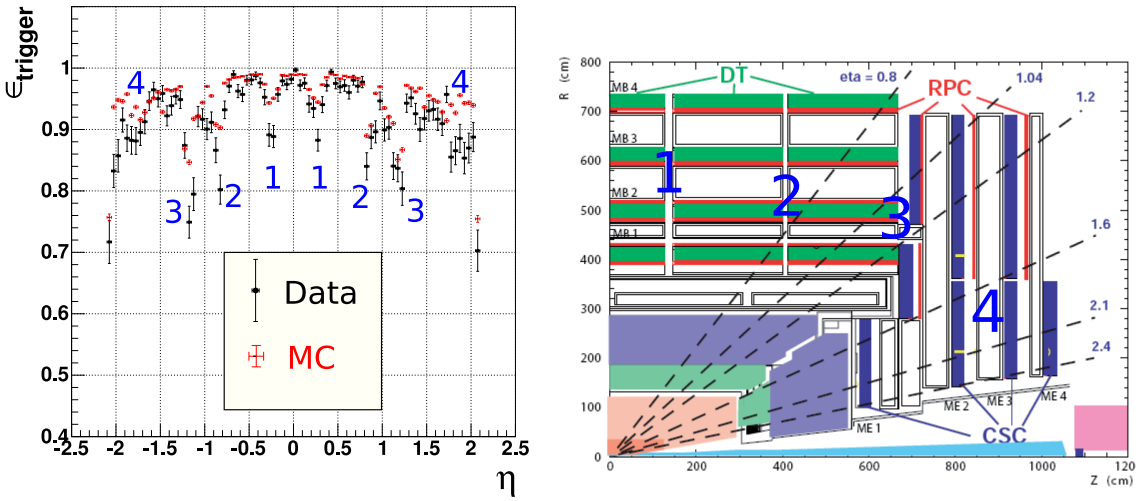

(a) Trigger efficiency.

(b) Cross section of the CMS muon system.

Figure 5.12: Left: Trigger efficiencies derived with the tag and probe method on data (black) and a simulated Z/γ^* sample (red). The dips in the distribution are related to gaps in the CMS muon system shown on the right.

All efficiencies for cuts associated with the muon system show dips in the η regions where the muon system has gaps because of its wheel structure. This applies to the global muon reconstruction ϵ_{Glb}, which starts in the muon system, the identification criteria, which include cuts associated with both the inner track and the muon system and, most distinctively, the muon triggering. The tracker reconstruction efficiency, which is defined with respect to a successful global muon reconstruction in this work, and the isolation efficiency are almost flat in η.
The muon trigger efficiency binned in η and its relation to the structure of the muon system are depicted in Figure 5.12. The trigger efficiency drops between the wheels and in the overlap region of the barrel part equipped with DTs and the forward region equipped with CSCs. These dips are expected from simulation, however they are more pronounced in data. Moreover, the efficiency in the forward region $1.7 \lesssim |\eta| \lesssim 2.1$ is lower than expected from simlation by a factor of about 0.92. In the barrel region away from the dips the trigger efficiency measured in data is only a little lower than expected and the simulation fits the data best. The shape of the η distribution for the other efficiencies is well described by simulation. In particular the pronounced difference between data and simulation for the dips and the forward region occurs only for the trigger efficiency.

For the muon transverse momentum range studied with the tag and probe method $p_T > 20$ GeV, the efficiency distributions are flat, except for the isolation efficiency ϵ_{iso}, which is p_T dependent by definition. The average activity around muons from W and Z decay, is not correlated with the muon itself and therefore does not depend on the muon p_T. This is not the case for the QCD background, where the energy of muons arising from a jet is on average correlated with the jet energy. Moreover, the muon p_T spectrum of the signal lies at significantly higher values than the steeply falling spectrum from QCD muons. Therefore a relative isolation allows for a background suppression with very high signal efficiency. This comes at the cost of a turn-on in the

isolation efficiency for low p_T, shown in Figure 5.13, which is not as pronounced when using an absolute isolation criterion with similar global isolation efficiency. For $p_T \gtrsim 40$ GeV the isolation efficiency is compatible with $> 99\%$ within the statistical uncertainty. Figure 5.14 shows the

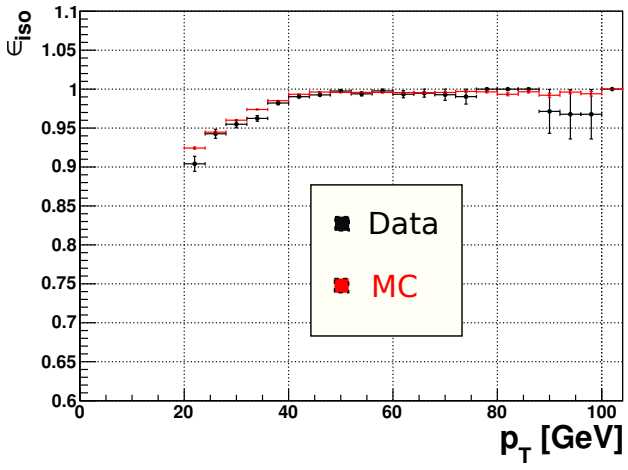

Figure 5.13: Comparison of the isolation efficiencies derived with the tag and probe method on data (black) and a simulated Z/γ^* sample (red). The turn-on behaviour for 20 GeV $< p_T <$ 40 GeV that occurs for the relative isolation is reproduced well by the simulation.

η and p_T distributions for the product of the individual efficiencies. The overall offset between data and simulation in the p_T distribution is due to the different global trigger efficiencies. The turn-on is explained by the isolation efficiency. The shape of the η distribution is mainly driven by the trigger efficiency.
The η and p_T dependencies of the ratio of efficiencies obtained from data and simulation, which enters the analysis as the efficiency correction factor, are also shown in Figure 5.14. As described above, the structure of this ratio in η is introduced by the trigger requirement. Although there are some differences between the expected muon efficiencies from simulation and data, the overall agreement shows no sign of unexpected major inefficiencies that might spoil some analysis techniques established with studies on the simulation or suggest different sets of cuts.
The global efficiency correction considered so far (Tables 5.11 and 5.10) has been derived using Z events with the acceptance cuts $|\eta^\mu| < 2.1$ and $p_T^\mu > 20$ GeV. As shown in the context of the acceptance determination in Figures 5.1 and 5.3, the kinematic distributions for muons from $W^\pm$ and Z events differ. In addition, the muons in the $W \to \mu\nu$ analysis have to pass a tighter p_T cut of $p_T > 25$ GeV. The η and p_T distributions of the product of muon efficiencies obtained on data and the corresponding distributions of generated muons after final state radiation within the acceptance $f_\mu^{MC}(\eta)$, $f_\mu^{MC}(p_T)$ obtained from simulation are convoluted in order to get an improved global muon efficiency estimate for the $W \to \mu\nu$ analysis.
The folding integral is approximated using the same binning for the distribution to be folded as for the binned total efficiency from data. The formulae read:

$$\epsilon_{tot}^{weight,\eta} \equiv \int_{|\eta|<2.1} \mathrm{d}\eta\ \epsilon_{tot}(\eta) \cdot f_\mu^{MC}(\eta) \approx \sum_{bins\ i}^{|\eta|<2.1} \epsilon_{tot,i}^{data}(\eta) \cdot \left(\frac{N_i}{N_{tot}}\right)_\eta^{MC} \tag{5.27}$$

$$\epsilon_{tot}^{weight,p_T} \equiv \int_{p_T^{min}}^{p_T^{max}\equiv 70\ \mathrm{GeV}} \mathrm{d}p_T\ \epsilon_{tot}(p_T) \cdot f_\mu^{MC}(p_T) \approx \sum_{bins\ i}^{p_T^{min}<p_T<70\ \mathrm{GeV}} \epsilon_{tot,i}^{data}(p_T) \cdot \left(\frac{N_i}{N_{tot}}\right)_{p_T}^{MC} \tag{5.28}$$

where the acceptance cuts on p_T^{min} differ for the Z and W analyses. In the case of the folding in p_T an upper cut has to be introduced in the sum because of the small Z statistics used for the efficiency determination in the high-p_T regime. This reweighting procedure is depicted in Figure 5.15 for the variable η.

Before applying the reweighting to the $W^\pm \to \mu\nu$ case, a closure check is performed using the $Z/\gamma^* \to \mu\mu$ simulation only, i.e. the muon distributions $f_{\mu,i}^{MC}(\eta)$ and $f_{\mu,i}^{MC}(p_T)$ and the result

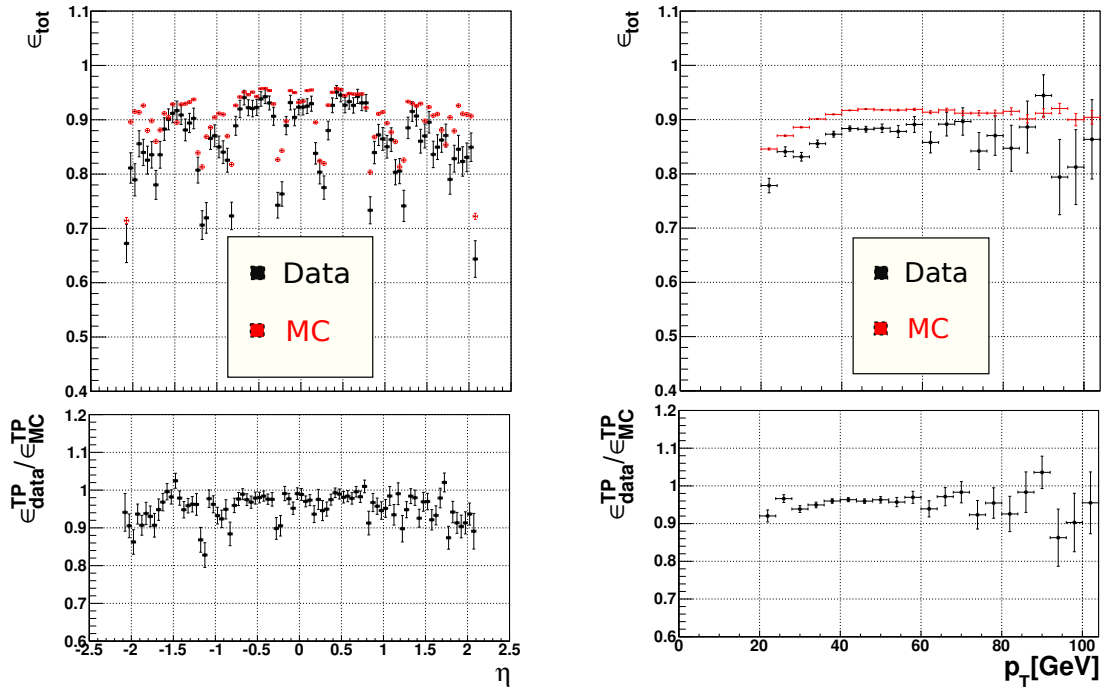

(a) η distribution.

(b) p_T distribution.

Figure 5.14: Overview of the product of efficiencies in η and p_T. Both the efficiencies obtained on the data and simulation and their ratio, which is used as an efficiency correction in the analyses, are shown. The structure of the efficiency plots are explained by the structure of the muon system in η and the efficiency turn-on of the isolation efficiency in the case of p_T. The ratio plot for η shows a muon detection inefficiency in the forward region of the muon system.

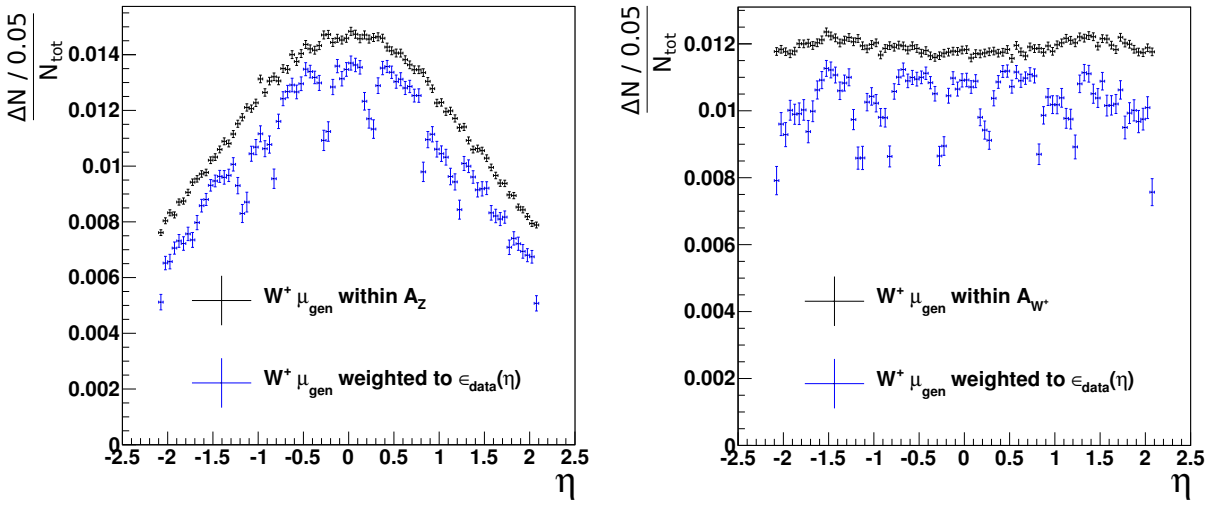

(a) Muons from $Z/\gamma^* \to \mu\mu$ sample.

(b) Muons from $W^+ \to \mu\nu$ sample.

Figure 5.15: The normalized η distribution of generated muons after final state radiation and kinematic cuts according to the simulation (black) and the bin-by-bin product of it with the total single muon efficiency ϵ_{tot} binned in η obtained from the data (blue).

of the tag and probe method run on the simulation $\epsilon^{MC}_{tot,i}(\eta)$ and $\epsilon^{MC}_{tot,i}(p_T)$. The results for the global efficiency ϵ_{tot} from reweighting are then compared to the result from simple tag and probe counting before subtraction of the background (the background is not subtracted for the efficiency distributions). The outcome of this closure test is reported in Table 5.13. The closure test does not show a bias of the reweighting method.

signal	$\epsilon^{TP,MC}_{tot}$	$\epsilon^{weight,\eta}_{tot}$ MC	$\epsilon^{weight,p_T}_{tot}$ MC
$Z/\gamma^* \to \mu\mu$	0.9050	0.9050	0.9050

Table 5.13: Closure test of the reweighting method performed on the $Z/\gamma^* \to \mu\mu$ simulation.

The result of the reweighting for $Z/\gamma^* \to \mu\mu$ and $W^{\pm} \to \mu\nu$ using the efficiency distributions obtained on data is shown in Table 5.14. The single muon efficiencies for the different signals agree within 3 permille. The highest efficiencies are obtained for the $Z/\gamma^* \to \mu\mu$ signal, followed by $W^- \to \mu\nu$ and $W^+ \to \mu\nu$. This is expained by the muons from $Z/\gamma^* \to \mu\mu$ being produced most centrally among the different signals and the muons from $W^- \to \mu\nu$ being produced more centrally than those from $W^+ \to \mu\nu$ (Figures 5.1 and 5.3) considering the slight trigger inefficiency in the forward region. The results obtained using Equations 5.27 and 5.28 differ slightly. In the case of the $W^{\pm} \to \mu\nu$ signal, the difference is rounded up and propagated to the final efficiency values as a systematic uncertainty. In the final efficiency determination for the $W^{\pm} \to \mu\nu$ signal, the values reported in Table 5.14 are used as a correction of the charge dependent efficiencies from tag and probe in Table 5.11.

signal	$\epsilon^{TP,data}_{tot}$ no bkg	$\epsilon^{weight,\eta}_{tot}$ data	$\epsilon^{weight,p_T}_{tot}$ data
$Z/\gamma^* \to \mu\mu$	0.8652	0.8654	0.8655
$W^+ \to \mu\nu$	-	0.8603	0.8596
$W^- \to \mu\nu$	-	0.8624	0.8620

Table 5.14: Results of the reweighting obtained using the efficiency distributions obtained from data. For comparison, the efficiency from event counting according to Equation 5.23 without background subtraction $\epsilon^{TP,data}_{tot}$ is given.

The results of the reweighting in Table 5.14 are obtained with transverse momentum cuts of $p_T > 20$ GeV and $p_T > 25$ GeV for the muons from Z/γ^* and $W^{\pm}$ decays, respectively. The single muon efficiencies for the $W^{\pm}$ samples with the reduced cut at $p_T > 20$ GeV are about 1% smaller than with the analysis cut $p_T > 25$ GeV. The main reason for this is the turn-on behaviour of the isolation efficiency in p_T (Figure 5.13). The difference between the efficiencies for the muons from $W^{\pm}$ and Z decays with the same p_T cut amounts to 1.0-1.5%, which is a non-negligible effect in precision measurements.

5.2.5 Results

According to the selection of the $Z \to \mu\mu$ and $W^{\pm} \to \mu\nu$ signals, the different single-muon efficiencies contribute to the full efficiency factor $\epsilon_{W/Z}$ as:

$$\epsilon_W = \epsilon_{Glb}\ \epsilon_{Trk}\ \epsilon_{ID}\ \epsilon_{Iso}\ \epsilon_{Trig} \tag{5.29}$$

$$\epsilon_Z = \epsilon^2_{Glb}\ \epsilon^2_{Trk}\ \epsilon^2_{ID}\ \epsilon^2_{Iso}\ \left(1-(1-\epsilon_{Trig})^2\right)\ . \tag{5.30}$$

In the Z case, both muons have to pass all selection criteria except for the trigger requirement and the associated efficiencies enter to the second power. Only one of the two muons has to be matched to a L3 trigger object. Therefore the trigger factor stands for the complementary event of both muons not firing the trigger, with the efficiency for one muon not firing the trigger given

by $(1 - \epsilon_{Trig})$. The tag and probe efficiencies can be taken directly from Table 5.9. The resulting full efficiency factor for Z events is given by:

$$\epsilon_Z = 0.8832 \pm 0.0029 \text{ (stat)} \pm 0.0080 \text{ (bkg)} \pm 0.0021 \text{ (trigger)} \pm 0.0088 \text{ (add)} \ . \tag{5.31}$$

Since correlated effects and the effect of variations of the different categories have not been studied, an additional systematic uncertainty of 1% is assigned. The systematic uncertainty due the background contamination is taken as the full difference of the result from Equation 5.30 with the individual efficiencies evaluated with and without the background (Table 5.9). This estimate is considered conservative because the estimated number of background events is not compatible with zero within the statistical uncertainties (Table 5.8).

For the W analysis, the full efficiency factor is simply the full single-muon efficiency. Since the efficiency values for different electric charge of the muon reported in Table 5.11 do not include the subtraction of the small background contributions, a correction is applied according to the change of the total muon efficiency from tag and probe including both charges with and without the background. Furthermore, a correction due to the different muon kinematics in $W^{\pm}$ and Z events is applied. The exact definitions using the results reported in Tables 5.11, 5.9 and 5.14 are:

$$\epsilon_W^{\pm} = \epsilon_{tot}^{\pm,Z} \cdot \left(\frac{\epsilon_{tot}^{bkg,Z}}{\epsilon_{tot}^{no\ bkg,Z}} \right) \cdot \left(\frac{\epsilon_{weight,\eta}^{\pm}}{\epsilon_{tot}^{no\ bkg,Z}} \right) \ . \tag{5.32}$$

The results read:

$$\begin{aligned} \epsilon_W^{+} &= 0.8664 \pm 0.0031 \text{ (stat)} \pm 0.0041 \text{ (bkg)} \pm 0.0010 \text{ (reweight)} \pm 0.0130 \text{ (trigger)} \pm 0.0087 \text{ (add)} \\ \epsilon_W^{-} &= 0.8646 \pm 0.0031 \text{ (stat)} \pm 0.0041 \text{ (bkg)} \pm 0.0010 \text{ (reweight)} \pm 0.0130 \text{ (trigger)} \pm 0.0086 \text{ (add)} \ . \end{aligned}$$

Instead of using the product of the acceptances and tag and probe efficiencies derived in this chapter, the full factor $A \cdot \epsilon$ is taken from the simulation and then corrected for the efficiencies determined on the data. This scheme has also been used in [60]. The corrections are applied in the following fashion:

$$A'_{W,Z} = (A \cdot \epsilon)_{W,Z}^{MC} \cdot \left(\frac{\epsilon_{data}^{TP}}{\epsilon_{MC}^{TP}} \right)_{W,Z} \ . \tag{5.33}$$

For the $W^{\pm} \to \mu\nu$ analysis, the factor $(A \cdot \epsilon)_W^{MC}$ includes the Z veto cut, which is neither included in the acceptance definition given above nor in the product of efficiencies ϵ_{tot}. The factors ϵ^{TP} correspond to the product of efficiencies ϵ_{tot}. Using the ratio of the tag and probe efficiencies obtained on the data and the simulation reduces biases due to the tag and probe method. The weighting of the efficiency to the kinematics of the W is included in the factor $(A \cdot \epsilon)_W^{MC}$ obtained from the simulation. The factor $\epsilon_{data}^{TP}/\epsilon_{MC}^{TP}$ does not contain corrections for the W kinematics. One effect not accounted for by the tag and probe method associated with imperfect timing in the DT system (pre-firing of the L1 trigger) has been identified and the effect on the $W^{\pm}$ and Z cross sections has been estimated in [60] to be about 0.5% and 1%, respectively. Therefore an additional factor of 0.995 and 0.99, respectively, is propagated to the efficiency correction factors. The results on the efficiency correction factors are summarized in Table 5.15.

signal	$\epsilon_{data}^{TP}/\epsilon_{MC}^{TP}$
$Z/\gamma^* \to \mu\mu$	0.9688 ± 0.0032 (stat) ± 0.0137 (syst)
$W^+ \to \mu\nu$	0.9580 ± 0.0034 (stat) ± 0.0179 (syst)
$W^- \to \mu\nu$	0.9536 ± 0.0034 (stat) ± 0.0180 (syst)

Table 5.15: Efficiency correction factors entering the $W^{\pm}$ and Z cross section determination.

The quadratic sum of statistical and systematical uncertainties on the correction factors are propagated to the cross section results as a systematic uncertainty.

Chapter 6

Missing Transverse Energy

At hadron colliders such as the LHC, the total momentum vector $\vec{p}$ of the interaction between two partons is not known due to the compositness of the protons in the initial state. However, the intrinsic transverse momentum of the partons within the proton $\vec{k}_T$ is negligible compared to the total transverse energy in the event and thus the transverse vector sum over all particles produced in the collision vanishes due to conservation of momentum. Exclusively weakly interacting particles cannot be detected within a collider experiment such as CMS, physics objects have a finite momentum resolution, objects are misidentified, particles fall into regions of the detector which are not fully instrumented and detector noise effects the vector sum over all detected objects. These phenomena give rise to an additional term in the vector sum, representing the missing transverse energy $\not\!\!E_T$:

$$\sum_{rec} \vec{p}_T + \vec{\not\!\!E}_T = 0 \ . \tag{6.1}$$

Assuming a perfect detector and reconstruction, exclusively weakly interacting particles would be the only source of missing transverse energy and could easily be identified. In practice, however, the missing transverse energy involves the entire event and is thus sensitive to every detector effect and the (mis)calibration of all reconstructed objects. This includes all the hadronic activity in the event from soft contributions due to the underlying event in proton-proton interactions and multi-proton interactions in the same bunch-crossing (pileup) to clustered energy (jets). In conclusion, its sensitivity to the entire event makes the understanding and calibration of the missing transverse energy an important challenge at the start-up of any hadron collider experiment. A proper understanding of the missing transerve energy is mandatory for the identification of leptonic W boson decays, which involve neutrinos in the final state.

6.1 Definitions and $\not\!\!E_T$ Reconstruction Algorithms

A definition of the missing transverse energy $\not\!\!E_T$ in terms of the reconstructed physics objects can be written as follows:

$$\vec{\not\!\!E}_T = -\left(\sum \vec{p}_T^{\,\mu} + \sum \vec{E}_T^{e} + \sum \vec{E}_T^{\gamma} + \sum \vec{E}_T^{jets} + \vec{U}\right). \tag{6.2}$$

The first terms in the sum are given by single-particle objects with well-calibrated momenta/energies from standard reconstruction. The contributions linked to the fragmentation and hadronization of partons are split into two contributions.

1. Clustered energy $\sum \vec{E}_T^{jets}$: Reconstructed jets above a p_T threshold which depends on the $\not\!\!E_T$/jet type (see below) used. For calorimetric $\not\!\!E_T$, the threshold is $p_T = 20$ GeV.

2. Unclustered energy $\vec{U}$: Energy deposits and tracks which are either not associated with the above mentioned physics objects or belong to a jet below the p_T threshold in 1.

6.1.1 Calorimetric $\not\!\!E_T$

The calorimetric $\not\!\!E_T$ algorithm (Calo $\not\!\!E_T$) [68] sums over calorimeter towers in the ECAL and HCAL up to the forward region $|\eta| < 5$, neglecting energy deposits below noise threshold. Since muons are minimally ionizing in a wide momentum range (1 GeV $\lesssim p_T^\mu \lesssim$ 100 GeV), they deposit only about 2 GeV in the calorimeters and the momentum information must be inferred from the track in the tracker and muon system. The muon track p_T is resummed and the associated deposit in the calorimeters is excluded from the sum. The explicit formula for the muon correction reads:

$$\vec{\not\!\!E}_T^{\,\mu} = -\sum_{\text{towers}} \vec{E}_T - \sum_{\text{muons}} \vec{p}_T + \sum_{\text{muons}} \vec{E}_T^{\,\text{MIP}}. \tag{6.3}$$

Since all other physics objects deposit almost their entire energy in the calorimeters, this is the only track correction which is mandatory to achieve a reasonable $\not\!\!E_T$ description.
In addition to the muon track correction, jet energy scale (JES) corrections [69] are applied to unfold the jet energy and $\not\!\!E_T$ to the particle level, which is relevant for the hard interaction. Among other effects, the JES corrections account for the nonlinearity in response of the calorimeters due to its non-compensating structure, the $|\eta|$ dependence due to different instrumentation and material budget in the tracker, the production of neutrinos within jets from meson decays and the neglect of energy deposits below threshold.

6.1.2 Track Corrected $\not\!\!E_T$

In contrast to Calo $\not\!\!E_T$, where corrections to the JES account for the under-measurement of the energy deposits in the calorimeters, the track corrected $\not\!\!E_T$ (TC $\not\!\!E_T$) algorithm [70] employs the tracker information to improve the raw Calo $\not\!\!E_T$ reconstruction, thus making use of the tracker's superior reconstruction of charged tracks with $p_T < 100$ GeV. The neutral component of the hadronic energy remains uncorrected and the muon correction is the same as in the case of Calo $\not\!\!E_T$. Each track that is not identified as a muon or electron is associated with a calorimetric energy deposit from a response function that is derived from a simulated single-pion sample (i.e. charged particles are treated as pions). The momentum of each reconstructed track replaces the associated energy deposit in the missing transverse energy:

$$\vec{\not\!\!E}_T^{\,\text{tc}} = \vec{\not\!\!E}_T^{\,\mu} + \sum_{\text{tracks}} \langle \vec{E}_T \rangle^{pion} - \sum_{\text{tracks}} \vec{p}_T. \tag{6.4}$$

Due to the non-negligible energy loss in the tracker, tracks with $p_T < 2$ GeV typically do not reach the calorimeters and are included without an associated energy deposit. For tracks with $p_T > 100$ GeV, the influence of badly reconstructed tracks supersedes the bias due to the calorimetric response and thus no correction is applied.

6.1.3 Particle Flow $\not\!\!E_T$

The abovementioned $\not\!\!E_T$ algorithms start from the information in the calorimeters which is corrected in further steps of the reconstruction. The Particle Flow $\not\!\!E_T$ (PF $\not\!\!E_T$) is based on a different approach to the reconstruction of the entire event [71], using the information from all subdetectors to generate a list of particles in the event that consists of five categories: muons, electrons, photons, charged and neutral hadrons. All objects are calibrated according to the specific particle type. Thus, instead of starting from higher order objects such as jets used in CaloMet and correcting for the JES, higher order objects are built from ensembles of particles with already calibrated momenta and energies. The PF $\not\!\!E_T$ is the negative sum of all particles in the event and includes by construction a correction of the calorimetric response for both charged and neutral components of the hadronic energy.

6.1.4 Type-I and Type-II Corrections

For future reference the terminology for $\not\!\!E_T$ corrections in CMS is briefly explained. The corrections to the raw $\not\!\!E_T$ reconstruction are divided into two contributions:

- **Type-I** corrections: JES corrections are applied to jets (clustered energy) above a threshold depending on the $\not\!\!E_T$ type. For Calo $\not\!\!E_T$ the criteria are $p_T > 20$ GeV and electromagnetic energy fraction < 0.9.
- **Type-II** corrections: An additional correction can be applied to the unclustered energy $\vec{U}$ in Equation 6.2. This part of the hadronic energy includes the underlying event and pileup and originates from non-perturbative QCD. Both the underlying physics and the detector response are different from high-p_T jets and therefore the $\not\!\!E_T$ correction is split into two parts.

In this thesis, the $\not\!\!E_T$ configuration includes only the type-I correction for Calo $\not\!\!E_T$ as described in section 6.1.1. No further corrections are applied to TC and PF $\not\!\!E_T$ which both already include a correction for tracker information.

6.2 $\not\!\!E_T$ in $Z \to \mu\mu$ Events

6.2.1 Definition of the Hadronic Recoil in $Z \to \mu\mu$ Events

This section consists of general remarks concerning $\not\!\!E_T$ that lead to the choice of PF $\not\!\!E_T$ as the baseline for the analysis. This study was carried out before the final dataset was chosen and the data used here is taken from RunB only and corresponds to an integrated luminosity of $L = 32.5$ pb^{-1}. As of Section 6.3, where quantitative input for the analyses is derived, the full dataset is used again.
$Z \to \mu\mu$ events are among the final states of highest purity that can be selected with a simple set of cuts at a hadron collider experiment. The vector boson four-momentum can easily be reconstructed from the two observed muons. In addition the muon p_T resolution for muons with $p_T^{\mu} \sim 50$ GeV is about 1%. All in all, this makes the Z a perfect probe for the hadronic energy that recoils against the vector boson (Figure 6.1).

The large Z production cross section and the high selection efficiencies for the signal ensure large statistics even for Z events that are accompanied by a high-p_T jet ($\approx 10\%$ of the selected Z events). Thus Z events can be used to test the detector response to both unclustered and clustered hadronic energy.

As illustrated in Figure 6.2, in Z events, the momentum sum in the transverse plane can be decomposed into three different contributions:

$$\vec{p}_T^{\,Z} + \vec{U}_T + \not\vec{E}_T = 0 \; . \tag{6.5}$$

Assuming the entire energy in the event could be measured, the hadronic recoil $\vec{U}_T$ would balance the vector boson. This is not the case in a real detector and the sum of the measured hadronic recoil and the transverse momentum of the Z is the negative missing transverse energy. The hadronic recoil can be split on an event-by-event basis into components parallel and perpendicular to the Z boson. The normalized basis vectors spanning the transverse plane are denoted $\vec{e}_1$ and $\vec{e}_2$:

$$\vec{e}_1 = \frac{1}{|\vec{p}_T^{\,Z}|} \begin{pmatrix} p_x^Z \\ p_y^Z \end{pmatrix} \qquad \vec{e}_2 = \frac{1}{|\vec{p}_T^{\,Z}|} \begin{pmatrix} -p_y^Z \\ p_x^Z \end{pmatrix} \tag{6.6}$$

$$U_1 = \vec{U}_T \cdot \vec{e}_1 \qquad U_2 = \vec{U}_T \cdot \vec{e}_2 \tag{6.7}$$

In the context of this thesis, Equation 6.5 serves as a definition for the hadronic recoil $\vec{u}_T$ in Z events:

$$\vec{U}_T \equiv -\left(\vec{p}_T^{\,Z} + \not\vec{E}_T\right) . \tag{6.8}$$

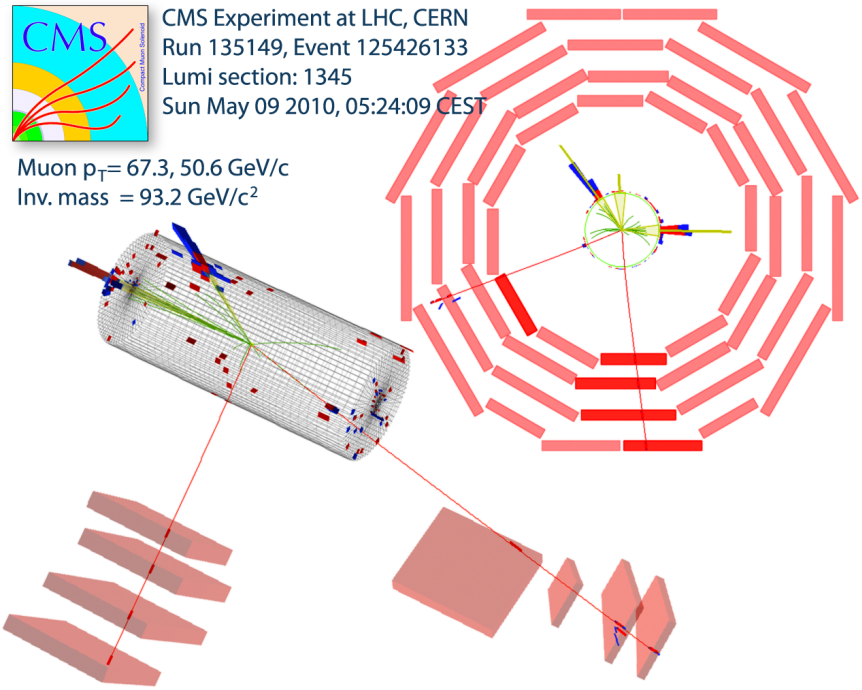

Figure 6.1: One of the first $Z \to \mu\mu$ candidate events observed with the CMS detector [56]. Two jets recoil against the muons.

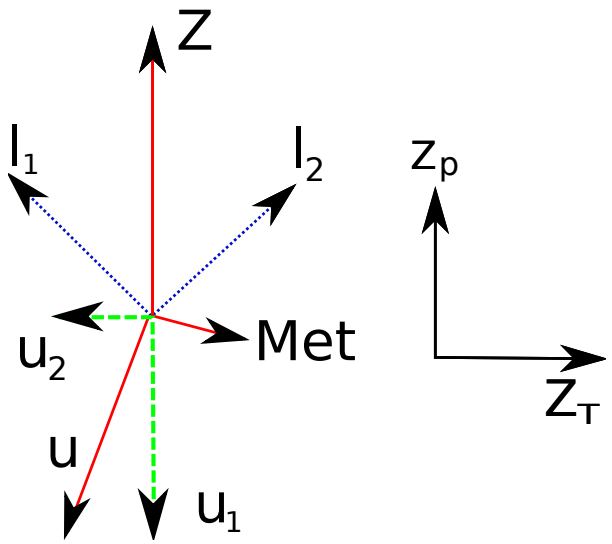

Figure 6.2: Hadronic recoil in $Z \to \mu\mu$ events split into contributions U_1 and U_2 parallel and perpendicular to the momentum vector of the vector boson, respectively.

The terms on the right hand side of Equation 6.8 are taken from the event content of the data and simulation.
The distributions of the Z p_T and the total hadronic recoil are shown in Figure 6.3 for data and the simulation using type-I corrected Calo $\not\!\!E_T$. The corresponding $\not\!\!E_T$ distribution is depicted in Figure 6.6. All three distributions peak around 10 GeV. This has the following implications:

- Typical Z events are accompanied by soft QCD contributions rather than hard QCD radiation with high-p_T jets. Only $\approx 10\%$ of the events have a hadronic recoil $|U_T| > 40$ GeV. Thus Z events provide more statistics for studies of the unclustered hadronic energy $\vec{U}$ in Equation 6.2 than for testing the jet response of the calorimeters.

- Considering the imperfections in the reconstruction of the hadronic energy in the calorimeters, the missing transverse energy plays an important rôle in the transverse momentum balance in Z events. In contrast to the $\not\!\!E_T$ distribution, p_T^Z and $|\vec{U}_T|$ exhibit pronounced tails above 40 GeV.

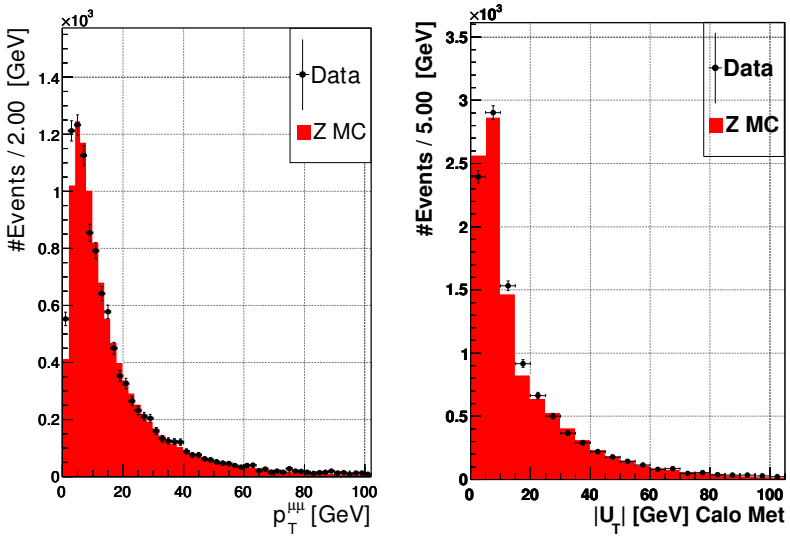

Figure 6.3: Left: Z boson p_T with the characteristic turn-over between 0 GeV $\leq p_T^Z \leq$ 10 GeV. Right: Magnitude of hadronic recoil $|u_T|$.

As shown in Figure 6.3, for low p_T^Z and $|\vec{U}_T|$ the characteristic turn-over can be seen for both data and simulation. In any fixed order calculation of the differential Z production cross section, the distributions would diverge for $|\vec{U}_T|$, $p_T^Z \to 0$ due to non-perturbative soft and collinear QCD radiation. In a full calculation to all orders the divergent large logarithms can be resummed, yielding a turn-on behaviour for both distributions (see for example [18]). In the high-p_T region dominated by perturbative QCD, the rapidly falling behaviour of the fixed order calculation determines the shape of the distributions. The combination of both regions yields the observed turn-over at about 5-10 GeV. In Figure 6.4 the two components of the hadronic recoil U_1 and U_2 are shown. While the recoil component perpendicular to the vector boson U_2 is symmetrically distributed around zero, the parallel component U_1 prefers the direction opposite to the Z, as expected. The tail in the total hadronic recoil (Figure 6.3) stems from the tail in the parallel component U_1 (Figure 6.4).

6.2.2 Pileup

At the design luminosity of $\mathcal{L} = 10^{34}\text{cm}^{-2}\text{s}^{-1}$ an average of ≈ 20 proton-proton interactions will take place at each bunch crossing every 25 ns. Each interaction of interest is thus overlaid by several uncorrelated event topologies. This phenomenon is named pileup. In the tracker, pileup

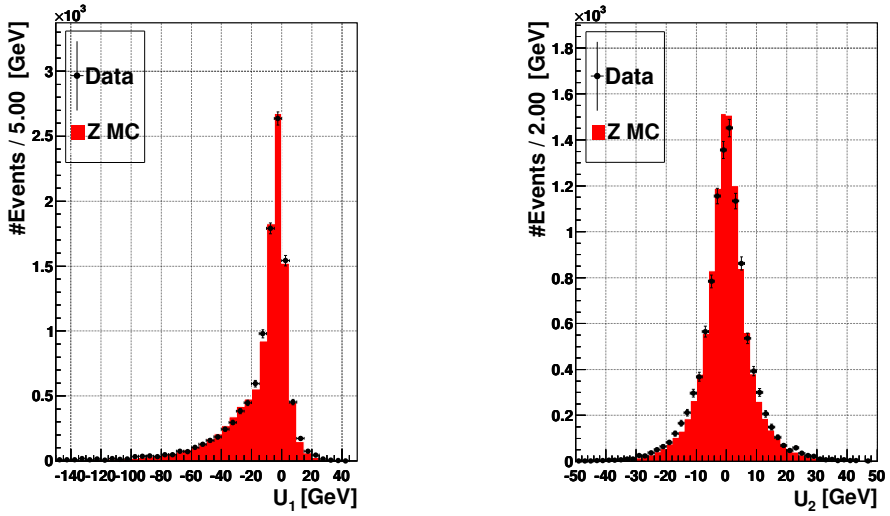

Figure 6.4: Components of the hadronic recoil for type-I corrected Calo $\not\!\!E_T$ in selected Z events for data (black) and simulation (red).

amounts to several primary vertices close to the nominal center of the detector in one bunch-crossing. Vertex requirements can be used to distinguish between pileup and parasitic interactions between protons in wrong bunch-crossings upstream the beam-pipe. The machine pileup also has to be distinguished from detector pileup that denotes the agglomeration of electronic signals from different events in the detector electronics.
For the CMS data considered in this anlysis, the instantaneous luminosity ranges from $\mathcal{L} \sim 10^{27}\text{cm}^{-2}\text{s}^{-1}$ to $\mathcal{L} \sim 10^{32}\text{cm}^{-2}\text{s}^{-1}$ and the estimated average number of pileup events per bunch-crossing [72] ranges from ≈ 0.1 to ≈ 2.3, respectively.
The following approach is used to estimate the effects of pileup on the $\not\!\!E_T$ reconstruction:

- So-called good vertices are defined by two requirements:
  - ≥ 5 degrees of freedom, i.e. tracks associated to the vertex.
  - $|z| < 15$ cm, i.e. the distance to the nominal center of the detector along the beam-pipe lies within a range that is consistent with a vertex arising from a good bunch-crossing.
- The standard MonteCarlo simulated samples are compared to simulated samples including pileup. The simulated events are reweighted to the good vertex distribution observed in data. The comparison between the good vertex distributions in data and simulation including pileup are shown in Figure 6.5.

6.2.3 Comparison of different $\not\!\!E_T$ Flavors

A comparison of the $\not\!\!E_T$ distributions for the three different $\not\!\!E_T$ algorithms is given in Figure 6.6. The data is compared to both the standard simulation and the simulation with pileup after vertex reweighting. The main effect of the additional pileup events is a degradation of the $\not\!\!E_T$ resolution, which smears events out of the peak region into the tail. The inclusion of pileup improves the agreement between simulation and data significantly for all $\not\!\!E_T$ flavors.
The $\not\!\!E_T$ algorithms including tracker information show less pronounced tails as Calo $\not\!\!E_T$. In data, both PF $\not\!\!E_T$ and TC $\not\!\!E_T$ algorithms find 48 events above 40 GeV, whereas Calo $\not\!\!E_T$ yields 172 events. The broadening of the Calo $\not\!\!E_T$ distribution with respect to PF $\not\!\!E_T$ and TC $\not\!\!E_T$ is explained by the superior resolution of the tracker compared to the calorimeters for charged particles in low-p_T jets. Figure 6.7 shows the scalar transverse energy $\sum E_T$ distribution for the different reconstruction algorithms. In the case of the Calo $\sum E_T$ reconstructor, the scalar transverse

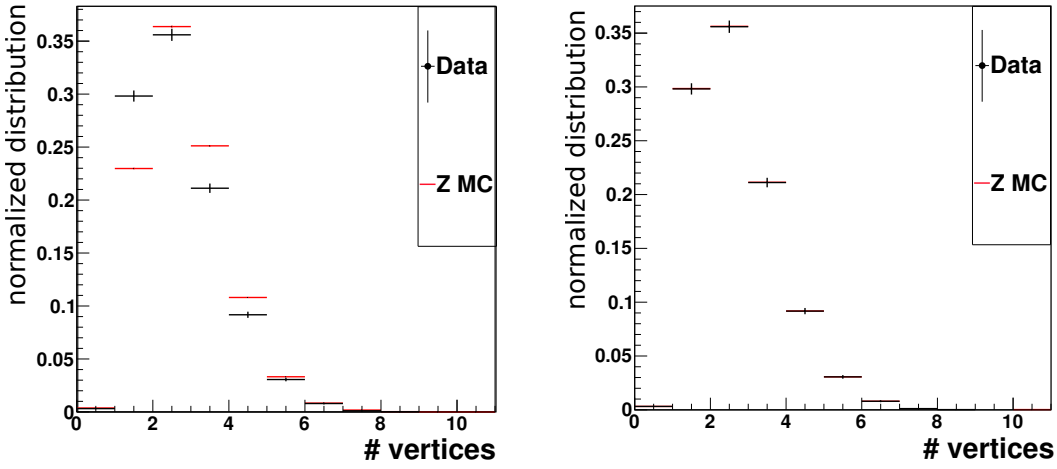

Figure 6.5: Comparison of the good vertex distributions in data (black) and simulation (red) before (left) and after (right) the reweighting.

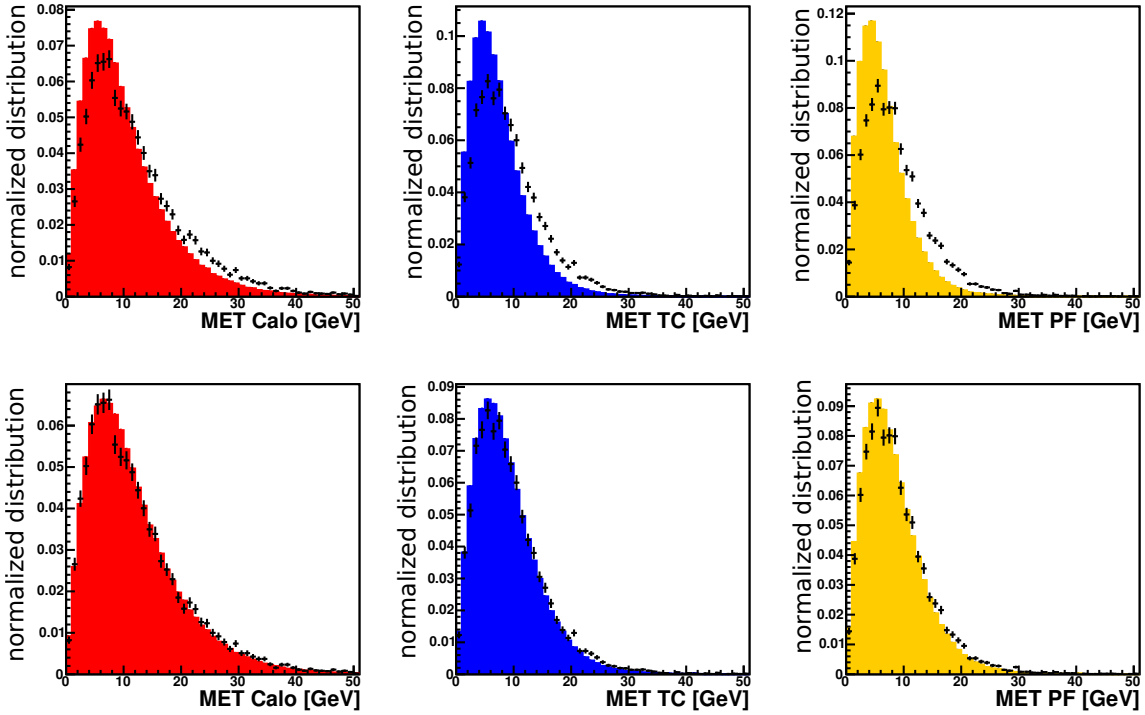

Figure 6.6: Comparison of $\not\!\!E_T$ for Calo $\not\!\!E_T$ (red), TC $\not\!\!E_T$ (blue) and PF $\not\!\!E_T$ (orange) in simulation and data (black). Upper row: Standard Monte Carlo simulation. Bottom row: Pileup Monte Carlo simulation reweighted to the distribution of good vertex in data.

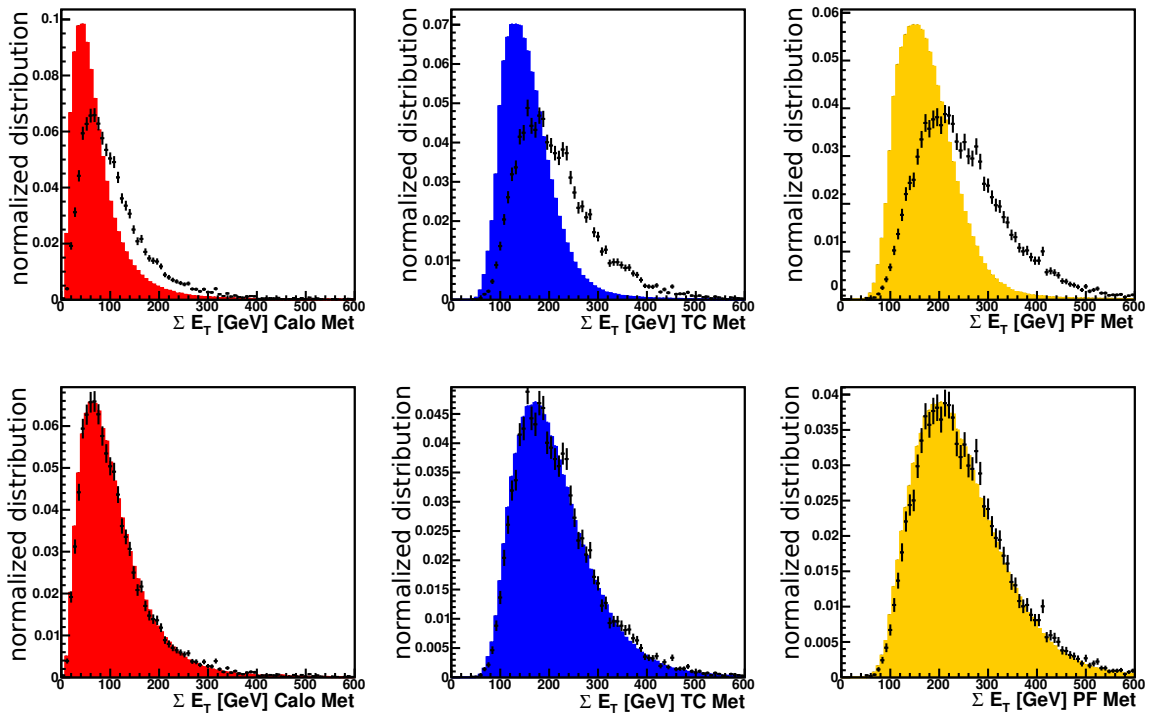

Figure 6.7: Comparison of $\sum E_T$ for Calo $\sum E_T$ (red), TC $\sum E_T$ (blue) and PF $\sum E_T$ (orange) in simulation and data (black). Upper row: Standard Monte Carlo simulation. Bottom row: Pileup Monte Carlo simulation reweighted to good vertex distribution in data.

energy is defined as the scalar sum over all entries above detector threshold. The corrections applied by the TC $\sum E_T$ reconstructor are the same as in the case of $\not\!\!E_T$ and the particle flow algorithm just sums up the $|p_T|$, $|E_T|$ contributions of all reconstructed objects. Although not as powerful as a discriminator in most physics analyses, $\sum E_T$ picks up every contribution to the entire event without cancellations as in the case of the vector sum $\vec{\not\!\!E}_T$ and is therefore helpful to detect noise or test the overall detector response. As depicted in Figures 6.6 and 6.7, $\sum E_T$ is more sensitive to pileup than $\not\!\!E_T$. The mean of the $\sum E_T$ is shifted by 44% (Calo), 33% (TC), 37% (PF), when including pileup (Table 6.1). The factor 2 between Calo $\sum E_T$ and the other two $\not\!\!E_T$ reconstructors is due to the better detector response when combinig information from the tracker and the calorimeters and the inclusion of track momenta below 2 GeV in TC and PF $\sum E_T$.

	$\langle\sum E_T\rangle$ Powheg [GeV]	$\langle\sum E_T\rangle$ Powheg PU [GeV]
Calo	73.6 ± 0.1	105.7 ± 0.1
TC	157.7 ± 0.1	210.1 ± 0.1
PF	176.3 ± 0.1	241.6 ± 0.1

Table 6.1: Mean of the $\sum E_T$ distributions for different reconstructors with and without pileup.

6.2.4 Response and Resolution

Compared to the resolution of the hadronic energy recoil against the Z, the Z transverse momentum distribution is narrow and the finite resolution of the muon p_T can be neglected. This makes Z events a useful probe for the detector response to hadronic energy and the corresponding resolution.

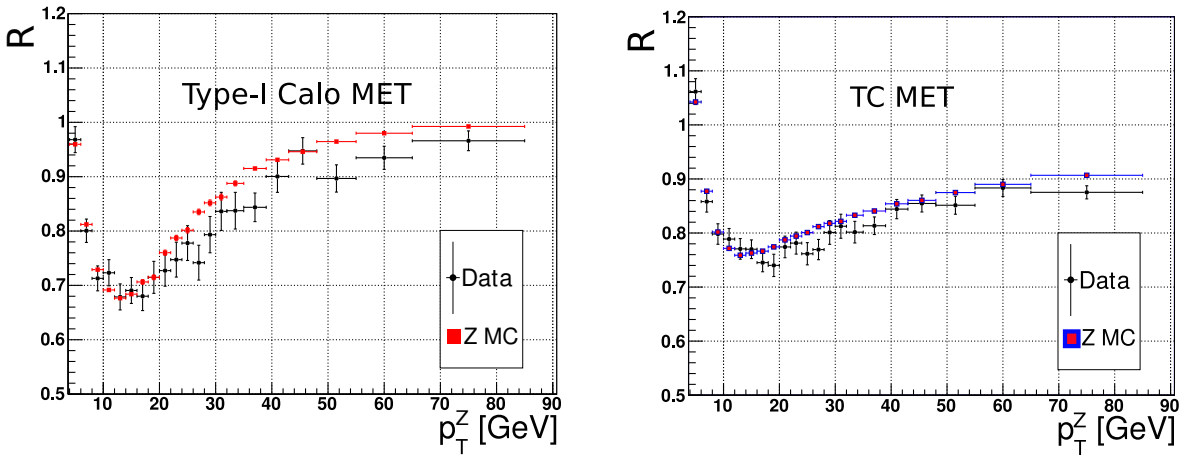

Figure 6.8: Comparison of the detector response in data (black) and simulation including pileup for Calo $\not\!\!E_T$ and TC $\not\!\!E_T$.

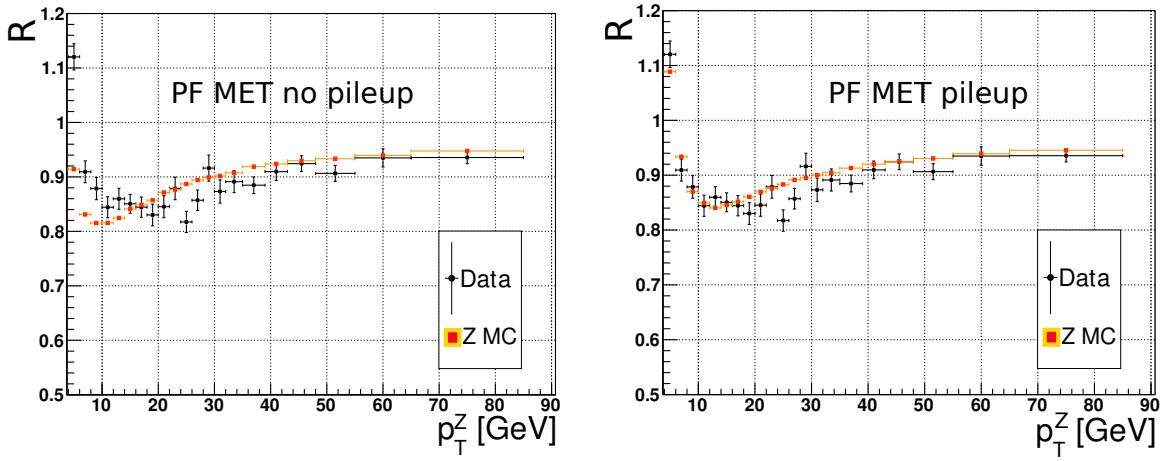

Figure 6.9: Comparison of the detector response in data (black) and simulation for PF $\not\!\!E_T$ with the standard simulation (left) and pileup simulation (right).

In the following the response R is defined as:

$$R = \langle \frac{|U_1|}{p_T^Z} \rangle. \tag{6.9}$$

Note that this definition is only suitable for $\langle |U_1| \rangle \gtrsim \mathrm{RMS}\,(U_1)$, which is the case for $p_T^Z \gtrsim 10$ GeV. The response is extracted event by event and the mean is calculated binned in Z p_T.
All the response curves in Figures 6.8, 6.9 show a turn-on for $p_T^Z \gtrsim 10$ GeV, due to the fact that unclustered low-energy objects are typically underestimated by the calorimeters. This feature also shows that Type-II $\not\!\!E_T$ are not applied. In the range 10 GeV $< p_T^Z <$ 20 GeV, the average response is about 70% for Calo $\not\!\!E_T$ in both data and simulation compared to 76% and 85% for TC and PF $\not\!\!E_T$, respectively. The difference between the two $\not\!\!E_T$ reconstructors including tracker information shows a substantial improvement by the most comprehensive $\not\!\!E_T$ reconstructor, PF $\not\!\!E_T$, compared to the ad hoc correction of Calo $\not\!\!E_T$ for tracks by the TC algorithm. The very good response of $> 95\%$ for Calo $\not\!\!E_T$ in the high p_T region is explained by the Type-I $\not\!\!E_T$ corrections.
The resolution of the recoil component U_1 is shown in Figures 6.10 and 6.11. The simulation including pileup improves the agreement between data and simulation compared to the simulation

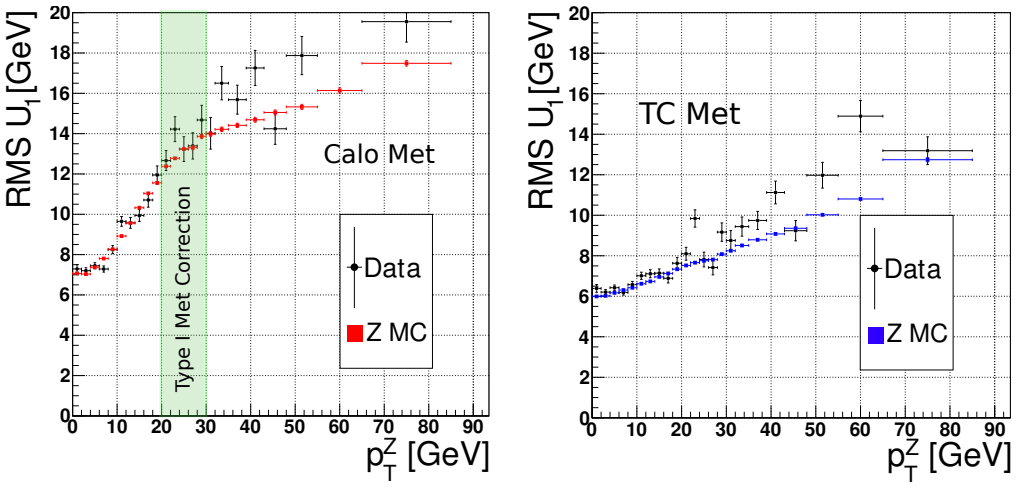

Figure 6.10: Comparison of the U_1 resolution in data (black) and simulation including pileup for Calo $\not\!\!E_T$ and TC $\not\!\!E_T$.

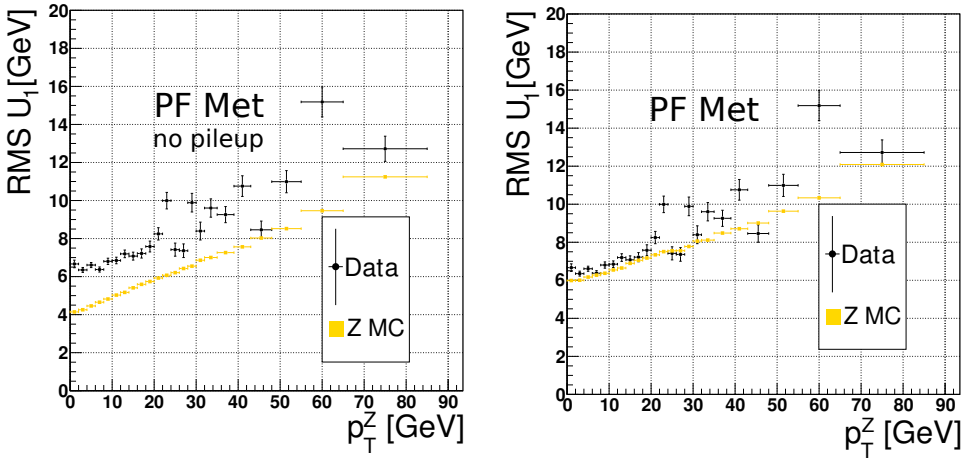

Figure 6.11: Comparison of the U_1 resolution in data (black) and simulation for PF $\not\!\!E_T$ with the standard simulation (left) and pileup simulation (right).

without pileup. However, the width of the hadronic recoil is still underestimated. The resolution is similar for TC and PF $\not\!\!E_T$. The Calo $\not\!\!E_T$ reconstructor exhibits a steeply increasing width of U_1 in the low Z p_T region. Beyond the Type-I correction threshold of 20 GeV the slope of the resolution is reduced.

The conclusion of this study is that the PF $\not\!\!E_T$ reconstruction is chosen as the baseline in the following analysis because of its good resolution, which leads for example to a clear separation of the QCD background and the $W \to \mu\nu$ signal in the M_T distribution after W selection (Figure 8.2), and its superior response in the low Z p_T region with high Z (W) statistics.

The underestimated width of the recoil in the simulation including pileup suggests that it might be favorable for precision measurements (such as W mass fits) to extract the hadronic recoil from the data itself and recalculate the $\not\!\!E_T$ information in the simulation accordingly. Such an approach is discussed in the next section.

6.3 Hadronic Recoil Modelling

Instead of relying on the $\not\!\!E_T$ information in the simulation, another option is chosen to build $\not\!\!E_T$ templates for the $W \to \mu\nu$ analysis. As in the case of the data-driven efficiency determination, information from Z events is used for the $W \to \mu\nu$ analysis. The hadronic recoil measured in Z events in data is parameterized and used to build a new $\not\!\!E_T$ replacing the original $\not\!\!E_T$ information in the simulation event by event. This method was introduced in CMS in [73].

Z events are selected in both data and simulation with the standard selection cuts from Chapter 4. The hadronic recoil components in the transverse plane parallel and perpendicular to the vector boson, U_1 and U_2, can be calculated in Z events with Equations 6.5 to 6.7. The chosen baseline PF $\not\!\!E_T$ is used throughout this section.
U_1 and U_2 are evaluated in bins of p_T^Z. When a sufficiently fine binning such as the one in Figure 6.13 is chosen, the U_1 and U_2 distributions can be approximated by a Gaussian[1]. Gaussian fits to the hadronic recoil components in a simulated $Z \to \mu\mu$ sample without pileup are depicted in Figure 6.12 for the bin 15 GeV $< p_T^Z <$ 16 GeV.

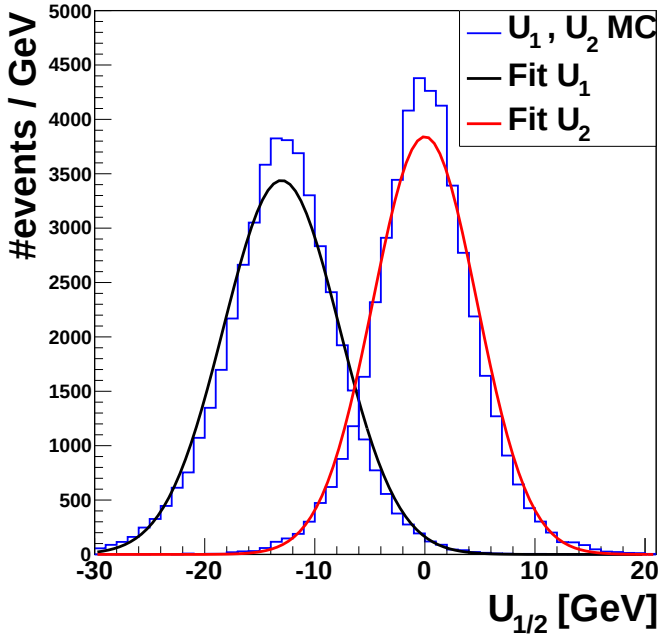

Figure 6.12: Distributions of the hadronic recoil components parallel and perpendicular to the vector boson, U_1 and U_2, in simulated Z events with 15 GeV $< p_T^Z <$ 16 GeV with Gaussian fits.

For each p_T^Z bin the Gaussian mean and width are extracted from the fits. The result is plotted in Figures 6.13 and 6.14. As discussed in the previous section, the width of the hadronic recoil in the simulation without pileup is underestimated. For low p_T^Z the width of both hadronic recoil components is about the same. The width of the recoil component parallel to the vector boson U_1 increases faster with increasing p_T^Z than the width of the perpendicular component U_2, because the hadronic activity parallel to the vector boson increases faster with p_T^Z than the hadronic activity perpendicular to the vector boson. However, the width of U_2 is not independent of p_T^Z because the hadronic activity recoiling against the Z spreads out perpendicular to the vector boson.
The dependence of the Gaussian means $\langle U_1 \rangle$ and $\langle U_2 \rangle$ with p_T^Z is well modelled by the simulation. $\langle U_2 \rangle$ is compatible with zero over the entire range in p_T^Z. $\langle U_1 \rangle$ exhibits an approximately linear

[1]Since the Calo $\not\!\!E_T$ used in this analysis does not include Type II $\not\!\!E_T$ corrections, this is only true for PF and TC $\not\!\!E_T$.

dependency on p_T^Z with slope < 1. This is explained by the response of the detector to hadronic energy studied in the previous section. The curvature of the second degree polynomial fit to $\langle U_1 \rangle$ as a function of p_T^Z in Figure 6.13 is explained by the turn-on behaviour of the response Figure (6.9).

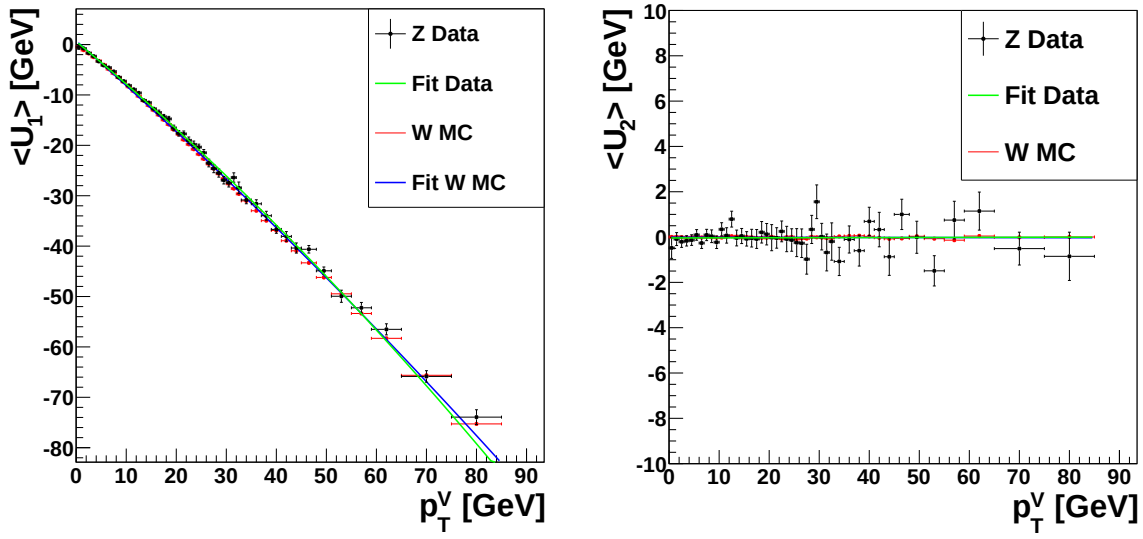

Figure 6.13: Comparison of the mean from Gaussian fits to U_1 (left) and U_2 (right) in data and simulation without pileup. The second degree polynomial fits are used for the construction of the data-driven recoil $\vec{U}'_T$.

The Gaussian mean and width as a function of p_T^Z are interpolated by a second degree polynomial for the widths σ_{U_1} and σ_{U_2} and the mean $\langle U_1 \rangle$. The choice of these functions is suggested by the simulation. The nomenclature used for these functions in the following reads:

$$\langle U_1 \rangle \left(p_T^Z\right) = p_0^{\langle U_1 \rangle} + p_1^{\langle U_1 \rangle} \cdot p_T^Z + p_2^{\langle U_1 \rangle} \cdot \left(p_T^Z\right)^2 \tag{6.10}$$

$$\sigma_{U_i} \left(p_T^Z\right) = p_0^{\sigma_{U_i}} + p_1^{\sigma_{U_i}} \cdot p_T^Z + p_2^{\sigma_{U_i}} \cdot \left(p_T^Z\right)^2 \quad , \quad i = 1.2 \; . \tag{6.11}$$

The simulated $W \to \mu\nu$ samples allow for the reconstruction of the W transverse momentum due to the stored information on the neutrino's four-momentum. Therefore the procedure described above can also be applied to the $W \to \mu\nu$ simulated samples with the hadronic recoil given as:

$$\vec{U}_T = -\left(\vec{\not{E}}_T + \vec{p}_T^{\,\mu}\right) \; . \tag{6.12}$$

The results for the p_T^V $(V = W, Z)$ dependence of the hadronic recoil components for $W \to \mu\nu$ is found to be in agreement with the result from the $Z/\gamma^* \to \mu\mu$ Monte Carlo samples. The new hadronic recoil U'_1 (U'_2) is sampled into the simulated samples event by event according to a Gaussian PDF of mean $\langle U'_1 \rangle$ $(\langle U'_2 \rangle = 0)$ and width $\sigma_{U'_1}$ $\left(\sigma_{U'_2}\right)$:

$$\langle U'_1 \rangle \left(p_T^W\right) = p_{0,data}^{\langle U_1 \rangle} \cdot \frac{p_{0,W}^{\langle U_1 \rangle}}{p_{0,Z}^{\langle U_1 \rangle}}|_{MC} + p_{1,data}^{\langle U_1 \rangle} \cdot \frac{p_{1,W}^{\langle U_1 \rangle}}{p_{1,Z}^{\langle U_1 \rangle}}|_{MC} \cdot p_T^W + p_{2,data}^{\langle U_1 \rangle} \cdot \frac{p_{2,W}^{\langle U_1 \rangle}}{p_{2,Z}^{\langle U_1 \rangle}}|_{MC} \cdot \left(p_T^W\right)^2 \tag{6.13}$$

$$\sigma_{U'_i} \left(p_T^W\right) = p_{0,data}^{\sigma_{U_i}} \cdot \frac{p_{0,W}^{\sigma_{U_i}}}{p_{0,Z}^{\sigma_{U_i}}}|_{MC} + p_{1,data}^{\sigma_{U_i}} \cdot \frac{p_{1,W}^{\sigma_{U_i}}}{p_{1,Z}^{\sigma_{U_i}}}|_{MC} \cdot p_T^W + p_{2,data}^{\sigma_{U_i}} \cdot \frac{p_{2,W}^{\sigma_{U_i}}}{p_{2,Z}^{\sigma_{U_i}}}|_{MC} \cdot \left(p_T^W\right)^2 \tag{6.14}$$

The new missing transverse energy $\not{E}'_T$ is calculated as:

$$\vec{\not{E}}'_T = -\left(\vec{U}'_T + \vec{p}_T^{\,\mu}\right) \; . \tag{6.15}$$

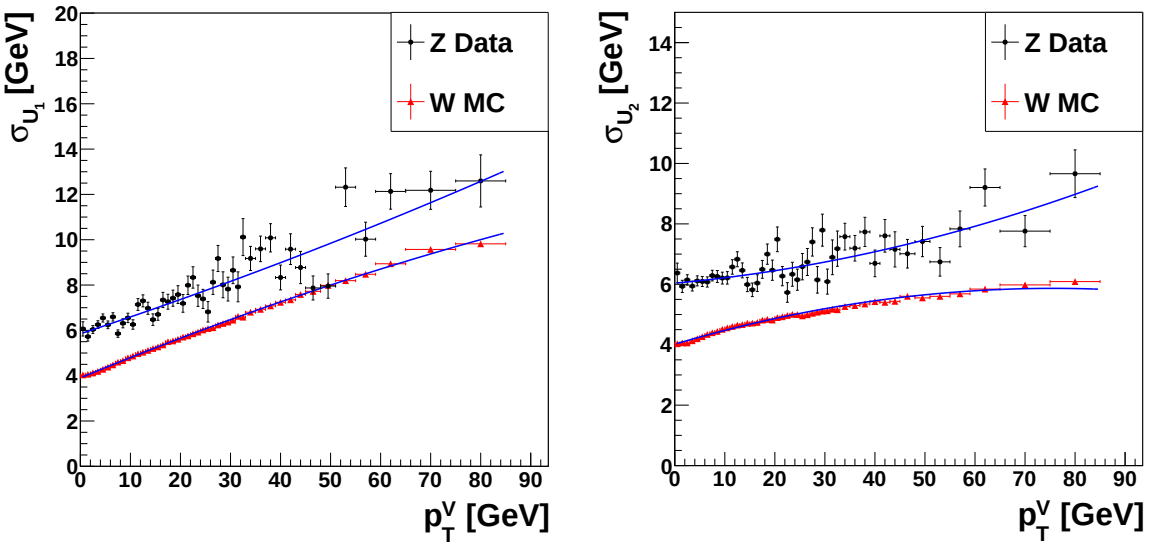

Figure 6.14: Comparison of the width from Gaussian fits to U_1 (left) and U_2 (right) in data and simulation without pileup. The second degree polynomial fits are used for the construction of the data-driven recoil $\vec{U}'_T$.

The intrinsic bias of this method is determined with a closure test. All parameters in Equations 6.13 and 6.14 associated with Z selected samples are set to 1, i.e. the parameterization of the recoil $\vec{U}'_T$ is directly taken from the $W \to \mu\nu$ simulation. A comparison of the $\not\!\!E_T$ and M_T distributions is shown in Figure 6.15 for the $W^+ \to \mu\nu$ simulation. Within the region of seizable $W^+ \to \mu\nu$ statistics, the bin-by-bin difference between the original simulated distribution and the distribution with the new $\not\!\!E'_T$ is found to be largest at the edge of the Jacobian, i.e. at $\not\!\!E_T \sim M_W/2$ and $M_T \sim M_W$. It reaches approximately 7% in the case of $\not\!\!E_T$ and 3% in the case of M_T. This bias corresponds to a broadening of the distributions and is explained by the assumption of a Gaussian for the U_1 and U_2 distributions binned in p_T^V. As depicted in Figure 6.12, the width of the distributions is slightly overestimated by the Gaussian. This feature is seen for all p_T^V bins in both the simulation and data and leads to the observed bias towards broader distributions. An extension of the recoil modelling with fits of the sum of two Gaussians has been studied on the simulation. However, the functional form of the two Gaussian widths per recoil component cannot be fitted by a simple model as the second degree polynomial in the single-Gaussian model. Omitting the fits to the recoil components altogether and sampling the new recoil according to the binned distributions measured on data is another approach that will be discussed in the context of the W mass fit in Chapter 9. The single-Gaussian model is used in the cross section fit.

The impact of the recoil modelling according to Equations 6.13 and 6.14 on the simulation without pileup is shown in Figure 6.16. The peak region with the highest W statistics is smeared out and the number of events in this region is reduced by a factor of about 0.9. The shapes of the edge of the Jacobian and the tail of the $\not\!\!E_T/M_T$ distributions are significantly changed with the number of events changing up to 50% for single bins.

Since no $\not\!\!E_T$-based cuts are applied in the $W \to \mu\nu$ cross section determination, the systematic uncertainty associated with the shape of the M_T signal distribution used in the fit is expected to be small. For the cross section the number of selected events is important rather than the distribution of the events after the selection. Therefore the systematic uncertainty on the cross section associated with the shape of the M_T distribution is evaluated in a conservative fashion by comparing the cross section results with recoil modelling and with the non-pileup simulation. The numbers are given with the cross section results in Section 8. This procedure of evaluating the systematics is not feasible for the W mass fit in Section 9, which is very sensitive to the shape

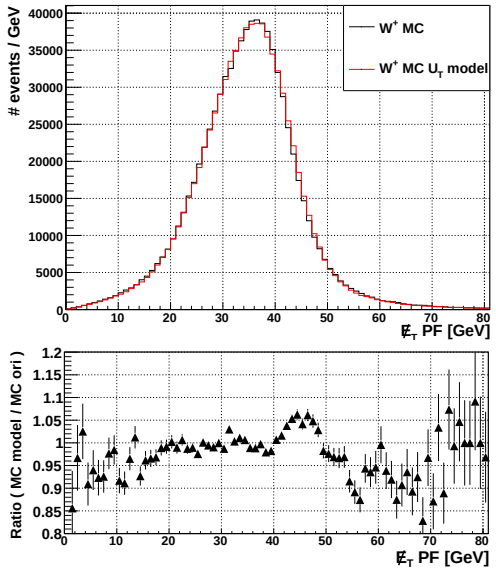

(a) Closure test recoil model for $\not{E}_T$.

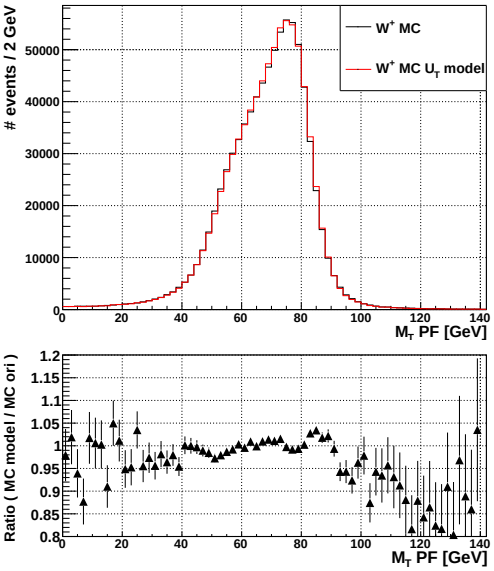

(b) Closure test recoil model for M_T.

Figure 6.15: Result of a closure test for the recoil model: $\not{E}_T$ and M_T distributions after W selection cuts in the original simulated $W^+ \to \mu\nu$ sample (black) and after application of the recoil modelling with input from the same $W^+ \to \mu\nu$ sample. The muon p_t cut is set to the final selection value $p_T > 25$ GeV.

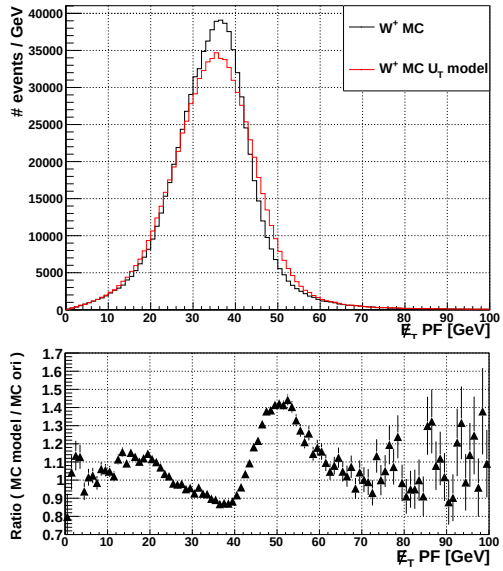

(a) Impact of the recoil model on $\not{E}_T$.

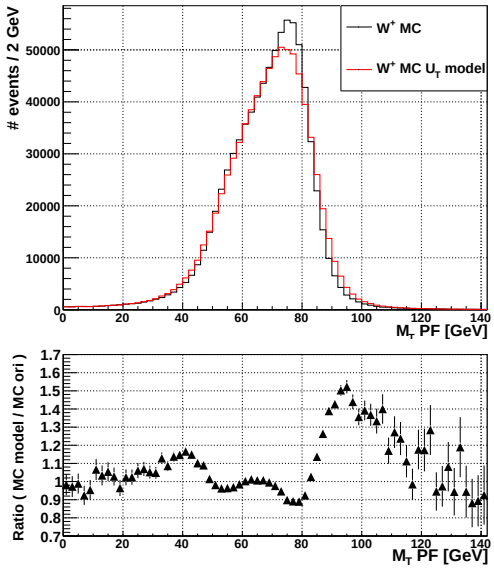

(b) Impact of the recoil model on M_T.

Figure 6.16: Impact of the data-driven recoil model on the simulated distribution without pileup: $\not{E}_T$ and M_T distributions after W selection cuts in the original simulated $W^+ \to \mu\nu$ sample (black) and after application of the recoil modelling. The muon p_t cut is set to the final selection value $p_T > 25$ GeV.

of the M_T distribution. Instead, the statistical uncertainties of the fit parameters p_0 and p_1 from the recoil modelling on Z-selected data events in Equations 6.13 and 6.14 are varied up and down by 1σ in a maximally correlated fashion. The result are two additional error distributions for $\not\!\!E_T$ and M_T, one for the variation of the Gaussian widths σ_{U_1}, σ_{U_2} and one for the variation of the Gaussian mean $\langle U_1 \rangle$. The systematic uncertainty associated with the shape of the $\not\!\!E_T$ and M_T distributions is then evaluated by performing the fit using the distributions for the variations up and down. The determined uncertainties for the variation of the width and the variation of the mean are added in quadrature. The formulae for the thus evaluated uncertainty on an observable X (here: M_W) read:

$$\Delta_X^{width} = \frac{1}{2}|X_{up}^{width} - X_{down}^{width}| \tag{6.16}$$

$$\Delta_X^{mean} = \frac{1}{2}|X_{up}^{mean} - X_{down}^{mean}| \tag{6.17}$$

$$\Delta_X^{\not\!\!E_T\ shape} = \sqrt{(\Delta_X^{width})^2 + (\Delta_X^{mean})^2}\ . \tag{6.18}$$

The result of the variation of the fit parameters is examplarily shown in Figure 6.17 (a) for the fit to the Gaussian width σ_{U_1}. The impact on the M_T distribution of the $W \to \mu\nu$ signal for the variation of both widths is depicted in Figure 6.17 (b).

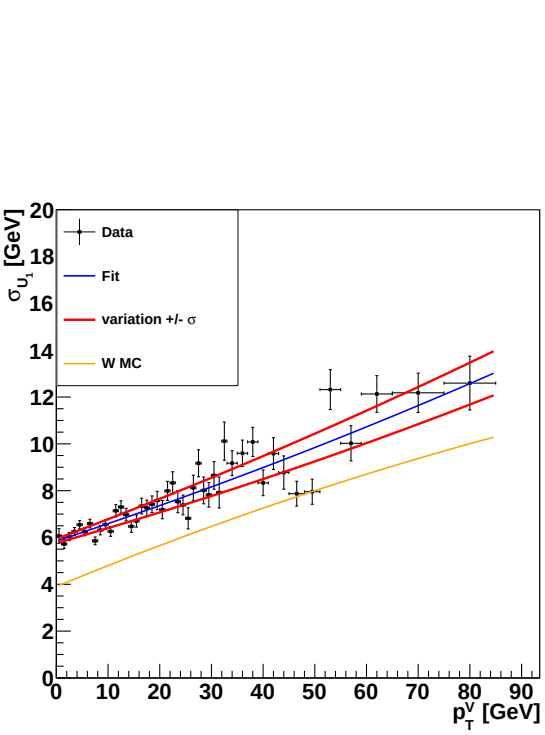

(a) Variation of the fit parameters (red) for σ_{U_1}.

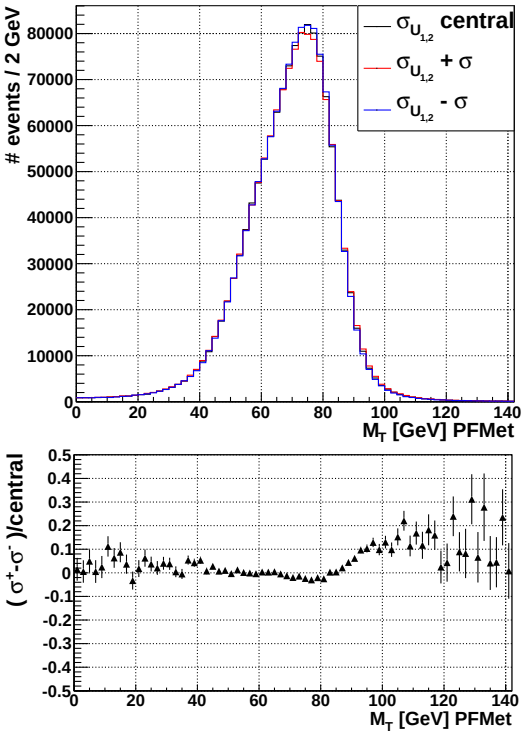

(b) M_T distributions for the central value of σ_{U_1}, σ_{U_2} (black) and the variation of the associated fit parameters up (red) and down (blue).

Figure 6.17: Impact of the variation of fit parameters for the Gaussian widths. The W MC shown for comparison does not include pileup.

The method for a data-driven hadronic recoil modelling presented here is one way to improve the agreement between the $W \to \mu\nu$ simulation without pileup and the data. It is used for the correction of the simulation in Chapter 8. A comparison with two other approaches is carried out in Chapter 9.

Chapter 7

QCD Background Estimation

In contrast to the Z/γ^* analysis with its fully reconstructable final state, the $W \to \mu\nu$ selection relies on the reconstruction of $\not{E}_T$, which is more ambiguous than the clean muon signature. Hence the $W \to \mu\nu$ signal suffers from a higher amount of background contamination than the Z/γ^* analysis, where the background is below the 1% level. The so-called electroweak backgrounds $Z \to \mu\mu$, $W \to \tau\nu$ and $t\bar{t}$ are supposed to be modelled well by the simulation. The background from QCD, mainly dijet events, involves more non-perturbative contributions and the simulation is therefore considered to be less reliable. Therefore evaluating the QCD background on the data itself with as little input from simulation as possible has the highest priority among the background considerations.
Deriving the QCD background from data calls for the selection of a dataset that is dominated by QCD events with a set of cuts that is as close to the original signal selection as possible. Muons from QCD events originate typically from mesons decaying in jets and are accompanied by activity in both the tracker and calorimetry, i.e. they are not well isolated. Another criterion useful for the $W \to \mu\nu$ analysis where the missing transverse energy $\not{E}_T$ and the transverse mass M_T are involved is the separation of the signal from the QCD background due to the considerable missing transverse energy or characteristic transverse mass distribution of the signal. As depicted in Figures 4.1 and 8.2, the QCD background populates the regions of lower p_T (similar for $\not{E}_T$) and M_T. The separation of the QCD background from the $W \to \mu\nu$ signal due to the isolation (relative isolation as defined above) and a $\not{E}_T$-based variable (M_T) as predicted by the simulation is shown in Figure 7.1.

In general, the background estimation method used is based on cut inversion and an extrapolation of the background dominating the inverted sample to the signal region. Comprehensive introductions to this technique can be found in [74], [75]. The conditions for this approach are:

1. Two variables that separate the background from the signal. These variables define a signal region A, where the background determination is most important, an inverted region that is divided into the subregions B and D and a control region C (Figure 7.1).

2. The variables ought to be statistically independent or at least as little correlated as possible.

Under the simplifying assumptions that regions B,C and D are populated by the background only and the two working variables x_1, x_2 described by the distribution function $\rho(x_1, x_2)$ are statistically independent, the number of background events in the signal region can be easily calculated.

$$\rho(x_1, x_2) = \alpha(x_1) \cdot \beta(x_2) \quad \Rightarrow \quad N_A = \frac{N_B \cdot N_C}{N_D} \ . \tag{7.1}$$

This is the idea behind the so-called ABCD approach, which only involves event counting in the four regions.
This idea can be extended from extrapolating a number of events to extrapolating distributions from the inverted region (B and D) to the non-inverted region region (A and C). Under the simplifications mentioned above, the background distribution of variable x_2 in the non-inverted

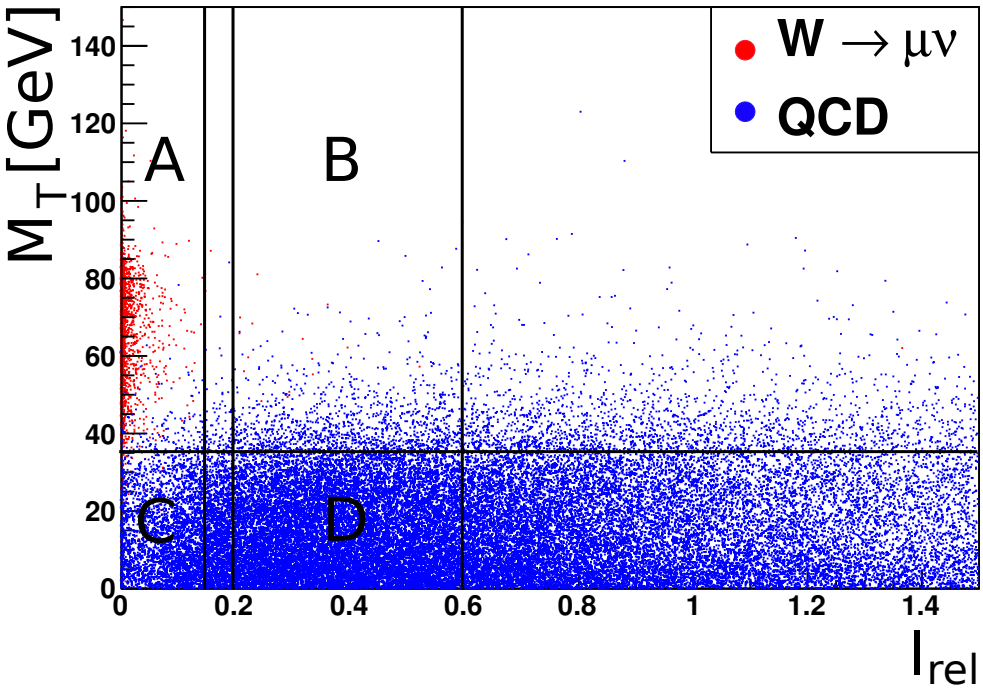

Figure 7.1: Separation of the QCD background (blue) from the $W \to \mu\nu$ signal (red) as predicted by the simulation. The regions for an ABCD-like background estimation in the signal region A are shown.

region can be obtained from the one in the inverted region by simple extrapolation. The scaling can be extracted from additional observables or by fitting both the signal distribution and the background for the variable x_2 to the x_2 distribution observed in data.
Before turning to the background extraction, the correlation between pairs of working variables composed of one isolation based variable and one $\not\!\!E_T$-based variable is studied in order to quantify the deviation from the ideal statistically independent behaviour.

7.1 Correlation Studies

The pairs of isolation and $\not\!\!E_T$-based variables under consideration are:

$$(I_{abs}, M_T)\,, \quad (I_{rel}, \not\!\!E_T)\,, \quad (I_{abs}, M_T)\,, \quad (I_{abs}, \not\!\!E_T) \quad . \tag{7.2}$$

All $\not\!\!E_T$-based variables in this section are based on the PF $\not\!\!E_T$ reconstruction. The relative isolation I_{rel} is the isolation variable defined in the signal selection, the absolute isolation I_{abs} is given by the activity around the muon only without dividing out the muon p_T, i.e. $I_{abs} = \sum_{Trk} p_T + \sum_{ECAL} E_T + \sum_{HCAL} E_T$. The Pearson's correlation coefficient [66]:

$$\rho_{xy} \equiv \frac{\mathrm{cov}\,(x, y)}{\sigma_x \sigma_y} \tag{7.3}$$

is used to quantify the correlation between the variables in a given pair. The Pearson's correlation coefficient is designed as a measure of the linear correlation between two variables. The case $\rho_{xy} = 0$ is not equivalent to statistical independence of the two variables, which is the desired feature for the QCD background extrapolation. However, it will be shown that the correlation for the varables finally considered in the analysis is approximately linear, which justifies the choice of the Pearson's correlation coefficient.
The correlation is determined on both the simulated QCD samples and the data. In order to select

a QCD sample of high purity on the data, the correlation analysis is restricted to the inverted region $I_{rel} > 0.2$[1]. All other cuts are the same as in the regular $W \to \mu\nu$ selection. The p_T cut is set to $p_T > 20$ GeV, allowing for the selection of a larger QCD sample on the data than the tighter cut at $p_T > 25$ GeV, which is helpful for testing the data-driven QCD background estimation.
The correlation coefficients for different pairs are reported in Table 7.1.

pair of variables (x, y)	ρ_{xy} data	ρ_{xy} MC
$(I_{abs}, \not{E}_T)$	0.187	0.223
(I_{rel}, M_T)	0.163	0.195
$(I_{abs}, \not{E}_T)$	0.098	0.123
(I_{rel}, M_T)	0.051	0.076

Table 7.1: Correlation coefficients quantifying the correlation between different pairs of isolation and $\not{E}_T$-based variables. Values are provided for both a QCD sample selected on data and the QCD simulated sample.

The correlations obtained on data are smaller than those from the simulated samples for all pairs. However, the ordering of the pairs' correlations is correctly reproduced by the simulation. The correlation decreases when using M_T instead of $\not{E}_T$ as the $\not{E}_T$-based variable and I_{rel} instead of I_{abs} as the isolation variable. Accordingly, the pair with the minimal correlation, which fulfills the conditions for the extrapolation best, is (I_{rel}, M_T). Those two variables are chosen as the main working variables in the following, although results of the extrapolation for the pair $(I_{rel}, \not{E}_T)$ will be given as well.
Table 7.2 contains the results for the correlation between $\sum E_T$, a measure of the overall energy in the event and kinematic variables of the QCD selected sample. This points to the reason why the relative isolation I_{rel} leads to smaller correlations with the $\not{E}_T$-based variables than the absolute isolation I_{abs}. All three variables missing transverse energy $\not{E}_T$, muon transverse momentum p_T^μ and the isolation I_{abs} exhibit a strong positive correlation with $\sum E_T$ in QCD events. $\sum E_T$ in QCD events is associated with the average jet energy in the events. A higher jet energy leads on average to higher muon momentum of muons from meson decay within the jet and to a worse isolation of these muons. It also leads to higher missing transverse energy due to mismeasurements of the jets. When using the relative isolation I_{rel} instead of the absolute isolation I_{abs}, the positive correlation of I_{abs} and p_T^μ with $\sum E_T$ is partly divided out and therefore the positive correlation between the isolation variable and $\not{E}_T$ is reduced.
The smaller correlation between p_T^μ and $\sum E_T$ compared to $\not{E}_T$ and $\sum E_T$ explains the reduction of the correlation when changing from the pair $(I_{rel}, \not{E}_T)$ to (I_{rel}, M_T).

pair of variables (x, y)	ρ_{xy} data	ρ_{xy} MC
$(\sum E_T, p_T^\mu)$	0.284	0.365
$(\sum E_T, \not{E}_T)$	0.339	0.389
$(\sum E_T, I_{abs})$	0.459	0.590

Table 7.2: Correlation coefficients quantifying the correlation of different kinematic and isolation variables with $\sum E_T$. Values are provided for both a QCD sample selected on data and the QCD simulated sample.

The distributions of the pairs $(\sum E_T, p_T^\mu)$, $(\sum E_T, I_{abs})$ and (I_{rel}, M_T) are depicted in Figures 7.2 and 7.3.

[1]For variables which are not statistically independent, the value of the correlation coefficient ρ_{xy} depends on the choice of this cut.

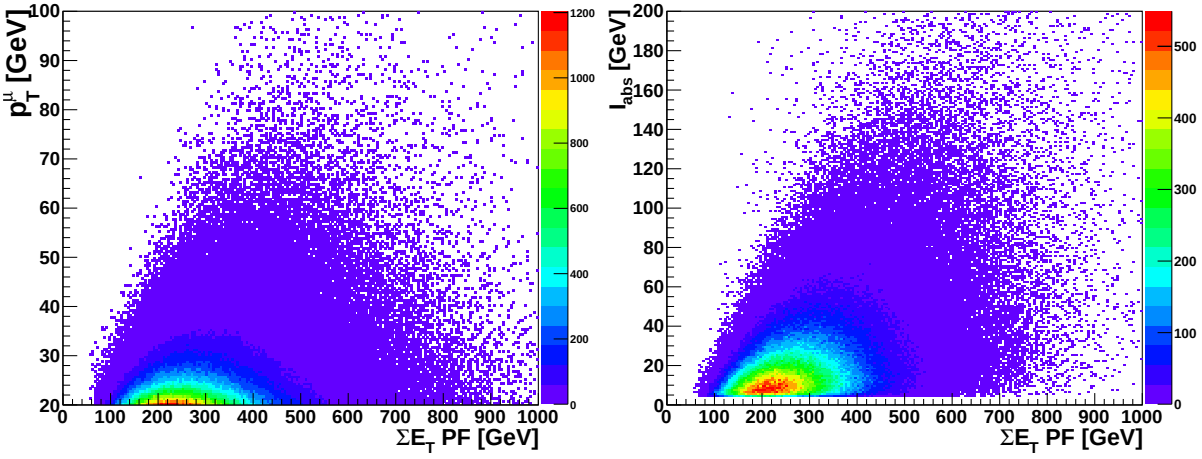

(a) p_T^μ vs. $\sum E_T$.

(b) I_{abs} vs. $\sum E_T$.

Figure 7.2: Correlation between muon related variables and $\sum E_T$ in QCD events selected via isolation-cut inversion on data.

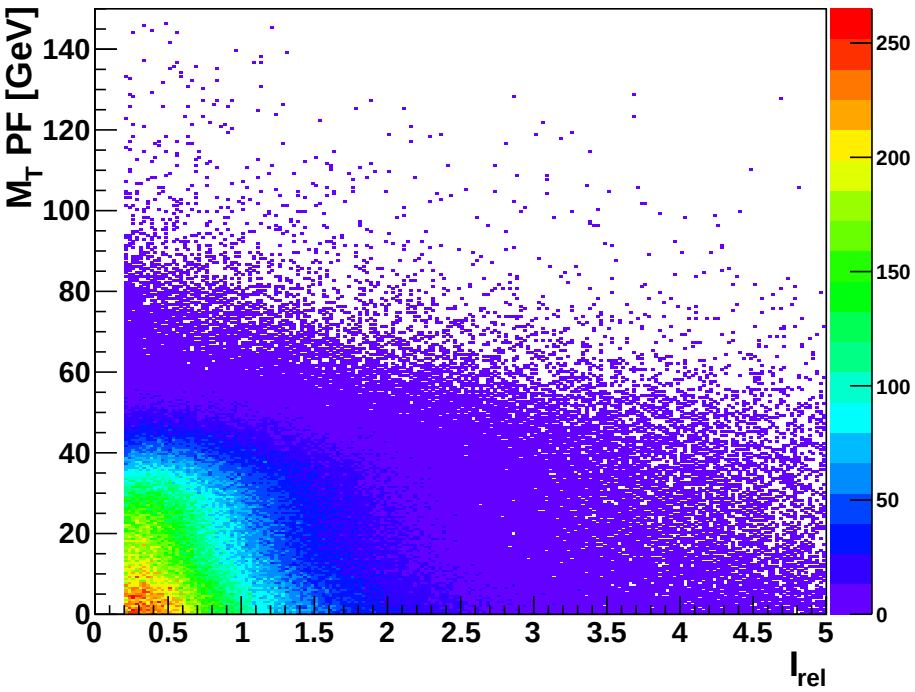

Figure 7.3: Correlation between I_{rel} and M_T in QCD events selected via isolation-cut inversion on data.

7.2 Data-driven QCD from semi-isolated Events

The selection of semi-isolated events calls for both a lower and an upper cut on the isolation. The lower limit is chosen close to the signal region at $I_{rel} = 0.2$ and the choice of the upper limit depends on two conditions:

- The distribution to be extrapolated should be similar to the original distribution in the signal region. This condition prefers a low upper limit.
- The selected sample should contain as much statistics as possible and at least as many QCD events as expected in the signal region.

The shape of the extrapolated distribution is roughly quantified by its mean and RMS, in order to be able to check the first condition on data and simulation. For the extrapolation of the M_T distribution using the PF $\not\!\!E_T$ algorithm, these two quantities are depicted in Figure 7.4 binned in I_{rel} for both data and simulation.

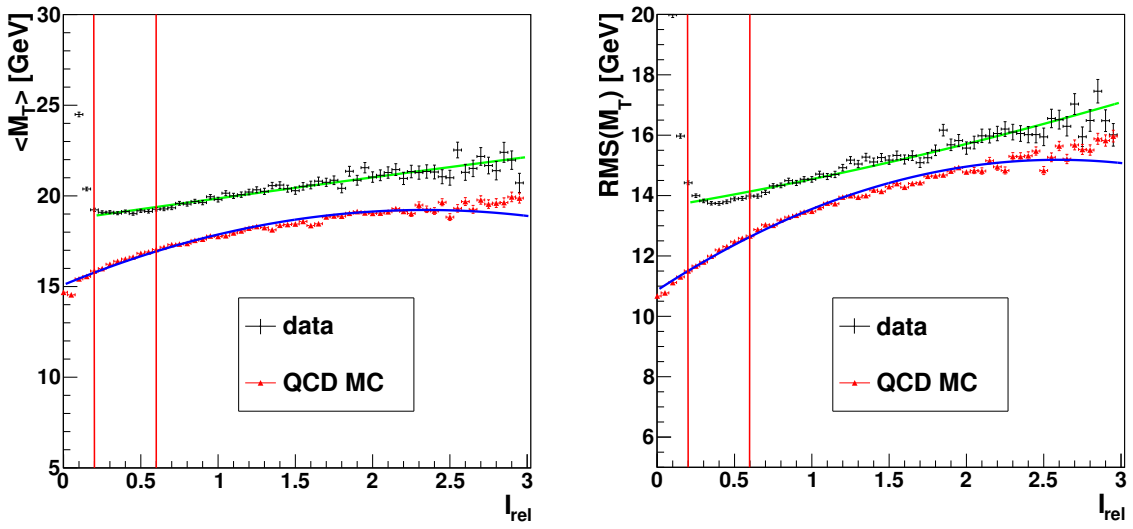

(a) Mean of M_T binned in I_{rel}.

(b) RMS of M_T binned in I_{rel}.

Figure 7.4: Mean and RMS of the M_T distribution binned in I_{rel}. The red lines indicate the lower and upper boundaries of the semi-isolated region. A second degree polynomial is fitted to data and MC as suggested by the shape of the curve in the simulation. No correction for electroweak contributions are applied, as indicated by the steep slope in data for $I_{rel} < 0.2$.

Both the mean and the RMS of the M_T distributions are underestimated by the simulation over the full range in I_{rel} considered. This is partly explained by missing pileup in the QCD Monte Carlo sample used here. Pileup has the effect of broadening $\not\!\!E_T$ and M_T distributions. The steep slope in the isolated region $I_{rel} < 0.15$ in Figure 7.4 manifest in data but not in the QCD simulated sample is due to the signal and electroweak backgrounds. The upper limit of the semi-isolated region is placed at $I_{rel} = 0.6$, ensuring a small variation of the M_T mean and RMS over the full semi-isolated region. The semi-isolated region is depicted in Figure 7.6 (a).
The remaining influence of the correlation between M_T and I_{rel} on the M_T distribution extrapolated with the semi-isolated method can be tested on the simulation and is illustrated in Figure 7.5. According to Figure 7.4 the QCD simulation suggest a stronger variation of the mean and sigma of the M_T distribution in the semi-isolated region than observed in data. Therefore the bias of the shape from extrapolation of semi-isolated events is expected to be smaller than shown in Figure 7.5. After the boundaries of the semi-isolated region have been defined, the extrapolation of the M_T distribution is straightforward. The remaining small electroweak contributions in

the semi-isolated region are subtracted. The corresponding M_T distributions are taken from the simulation and are scaled to the NNLO cross section. The effect of the correction for electroweak contributions on the number of QCD events extrapolated is below the 1% level.
In order to compare the extrapolated distribution to the data in the control region C, it has to be scaled to the appropriate number of events in the isolated region. The scaling factor is derived on another QCD sample of high purity that is accessible on data. The difference between the ϕ coordinates of the muon and $\not\!\!E_T$ in the selected single muon sample is assumed to exhibit a smaller correlation with the isolation of the muon than $\not\!\!E_T$ and p_T^μ. The bias on the scaling factor due to the correlation between $\Delta\phi$ and I_{rel} is tested on the QCD simulation and found to be of the order of 3% for PF $\not\!\!E_T$. As depicted in Figure 7.6 (b), the selected data at $\Delta\phi < 0.8$ is expected to yield a pure QCD sample. This sample is then divided into two subsamples, one with muons passing the isolation cut and the other with muon isolations falling into the semi-isolated region. Both subsamples are corrected for electroweak contributions as expected from the simulation. These corrections are negligible for the semi-isolated subsample but as big as $\sim$ 15% for the isolated subsample. The fraction of isolated to semi-isolated events determined with the subsamples is the sought-after scaling factor for the extrapolated template:

$$\mathcal{D}\left(M_T\right)^{iso}_{extrapolated} = \left(\frac{N_{iso}}{N_{semi-iso}}\right)_{\Delta\phi<0.8} \cdot \mathcal{D}\left(M_T\right)^{semi-iso} \tag{7.4}$$

with the M_T distribution of semi-isolated events $\mathcal{D}\left(M_T\right)^{semi-iso}$ and the scaled distribution to be compared to the data in the isolated control region $\mathcal{D}\left(M_T\right)^{iso}_{extrapolated}$. The scaling factors for PF, TC and Calo $\not\!\!E_T$ are 0.26, 0.26 and 0.29, respectively. The statistical uncertainty on the scaling factor is about 1%. The range $0 < M_T/\text{GeV} < 20$ of the final extrapolated M_T distribution $\mathcal{D}\left(M_T\right)^{iso}_{extrapolated}$ is compared to the M_T distribution observed in data after the isolation cut in Figure 7.7 for the PF $\not\!\!E_T$ and Calo $\not\!\!E_T$ cases. The distribution observed in data after the isolation cut is corrected for electroweak contributions expected from simulation. The agreement

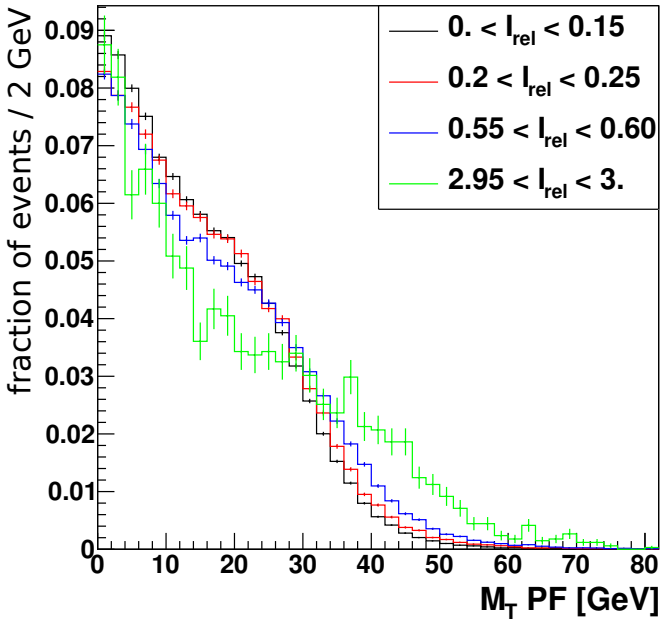

Figure 7.5: Influence of the correlation between M_T and I_{rel} on the extrapolated M_T distribution. The normalized distributions are shown for the entire isolated signal region and three smaller bins in I_{rel} that correspond to the lower and upper edges of the semi-isolated region and an example for very badly isolated muons ($2.95 < I_{rel} < 3$).

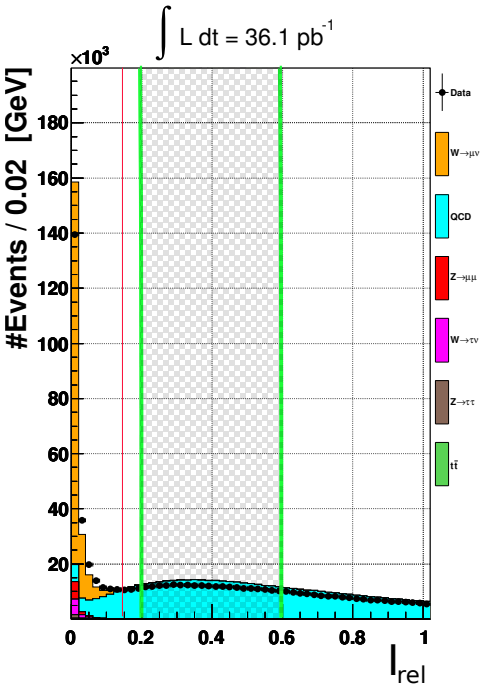

(a) Illustration of the semi-isolated region defined above (shaded). The selection cut is indicated by the red line.

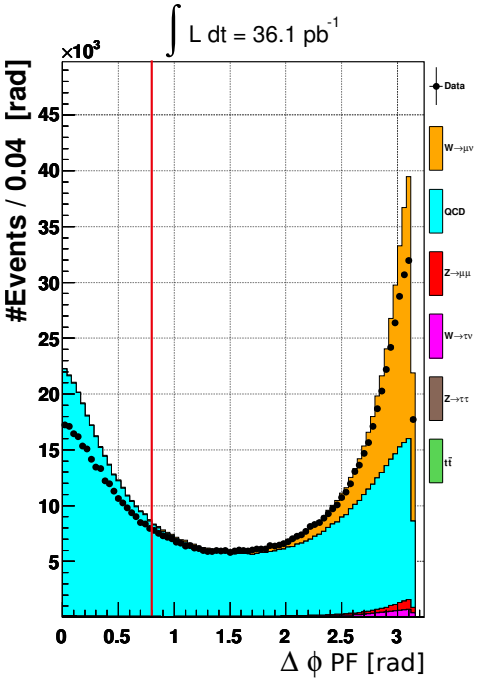

(b) The $\Delta\phi$ distribution of events after all selection cuts but the isolation cut applied. The red line indicates the subsample used to derive the scaling factor for the extrapolated QCD template ($\Delta\phi < 0.8$).

Figure 7.6: Distributions illustrating the semi-isolated method. The simulation shown does not include pileup and the QCD sample is scaled to the PYTHIA cross section which is known to be too high for the dominating contribution from B mesons [57], [58].

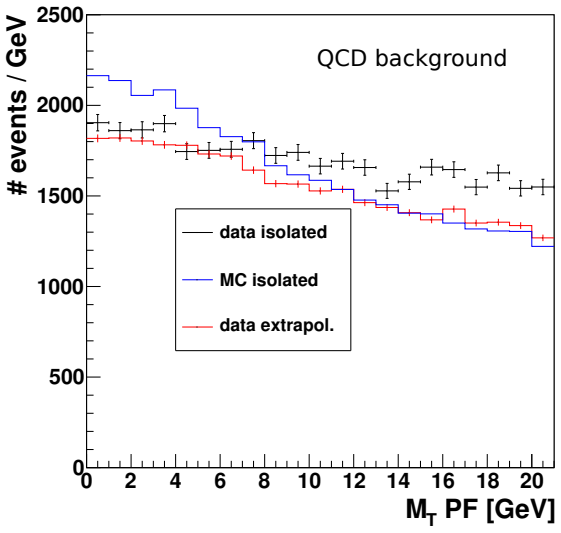

(a) QCD extrapolation for PF $\not\!\!E_T$.

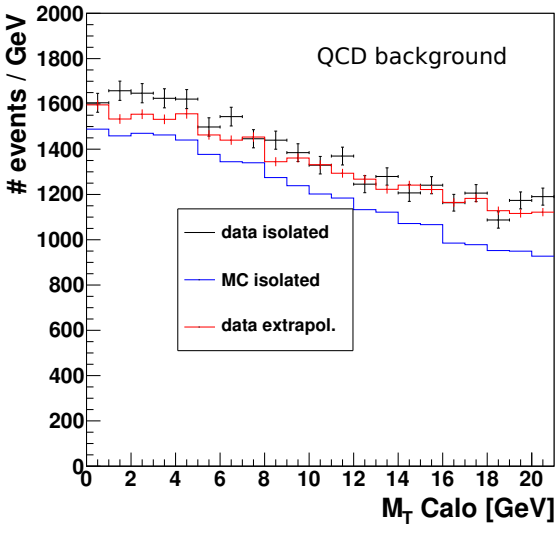

(b) QCD extrapolation for Calo $\not\!\!E_T$.

Figure 7.7: Results of the semi-isolated method for the M_T distribution obtained with the PF $\not\!\!E_T$ algorithm (left) and the Calo $\not\!\!E_T$ algorithm (right). The extrapolated template (red) is scaled with the method described above. The shape of the distribution from simulated QCD events in the isolated region is shown for comparison (blue). The QCD simulation is scaled such to allow for a simple comparison of the shapes.

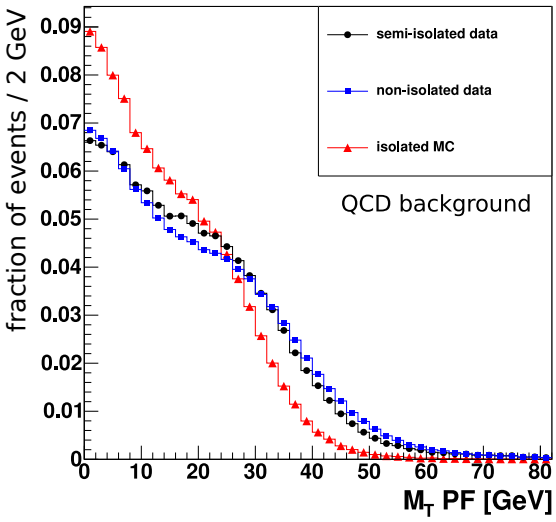

Figure 7.8: Comparison of the normalized M_T distribution obtained from the semi-isolated region in data (black), the full non-isolated region $I_{rel} > 0.2$ in data (blue) and the isolated region in the simulation (red).

is found to be good in the case of Calo $\not\!\!E_T$. In the case of PF $\not\!\!E_T$, the extrapolated distribution is twisted against the distribution of isolated data events but shows better agreement than the QCD simulation in the isolated region, which is plotted for comparison.
The observed improvement of the template obtained from the semi-isolated method with respect to the simulation tested in the control region justifies its application in the fit for the $W^{\pm} \to \mu\nu$ cross-section determination described in Section 8. The shapes of different templates of the M_T distribution from both data and the simulation are shown in Figure 7.8. The distribution taken from simulation is significantly steeper than those obtained from data. The distribution in the full non-isolated region $I_{rel} > 0.2$ is twisted with respect to the distribution from semi-isolated data events resulting in a longer tail, as expected. Since the cross section is obtained from a fit of background and signal templates to the M_T distribution observed in data, the effect of the different background shapes on the cross section is quantified in Section 8. For the cross-section result, the template from the semi-isolated region is used. The full difference on the cross section results obtained with the semi-isolated and the simulated template is taken as the systematic uncertainty due to the QCD background. Considering the seizable difference in the shape of these distributions, this uncertainty estimate is considered to be conservative.

In order to be able to extract the W^+/W^- cross section ratio, the data-driven QCD templates have to be determined for both electric charges of the muon. As depicted in Figure 7.9(a), the shapes of the two distributions agree but the yield is charge-asymmetric, with a preference of μ^+ production by about 5%. This asymmetry is expected from the simulation, where it amounts to 3% for selected QCD events in the isolated region.

Increasing the p_T cut from 20 GeV to 25 GeV reduces the QCD background with its steeply falling p_T distribution by a factor of 0.37. The number of QCD background events for PF $\not\!\!E_T$ in the full M_T range obtained with the data-driven template and scaling are reported in Table 7.3. Since the comparison in Figure 7.7 (a) suggests that the scaling is biased towards a lower QCD event yield in the case of PF $\not\!\!E_T$, the final numbers on the QCD background are taken from the cross section fit in Chapter 8. For the 25 GeV p_T cut, they are found to be about six percent higher than the numbers for the scaling described above.

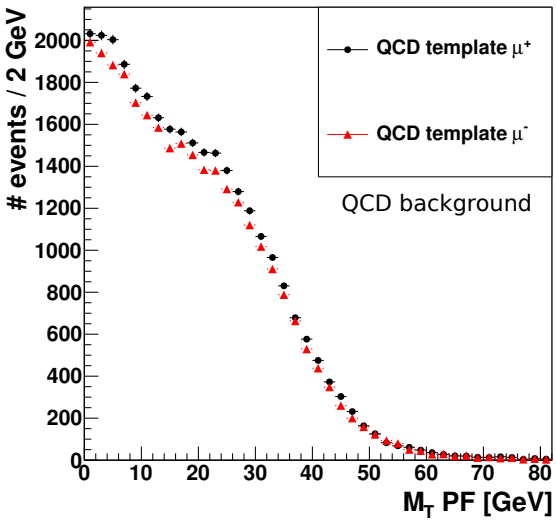

(a) Extrapolated M_T distribution for different muon charges after scaling. Both the shape and the scaling are derived from samples with the chosen muon electric charge.

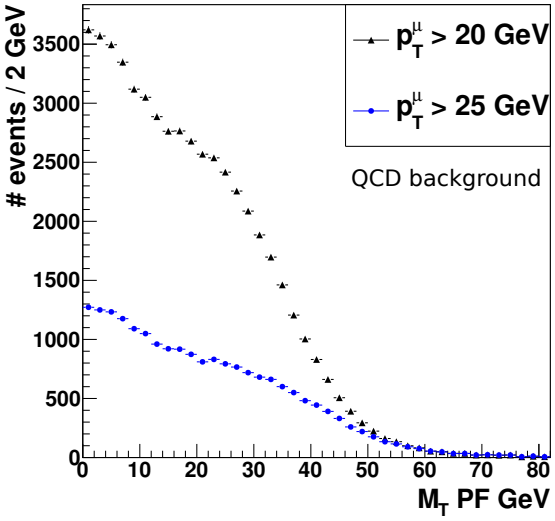

(b) Extrapolated M_T distribution for the default muon p_T cut at 20 GeV used throughout this section and the tighter cut at 25 GeV, used for the cross section determination.

Figure 7.9: Comparison of data-driven QCD templates for different muon charge and different muon p_T cuts.

	N_{QCD} $p_T^\mu > 20$ GeV	N_{QCD} $p_T^\mu > 25$ GeV
both charges	54141 ± 423	20214 ± 250
positive charge	30774 ± 321	10299 ± 179
negative charge	29335 ± 311	9915 ± 175

Table 7.3: Number of QCD events in the full M_T region after cuts obtained with the data-driven method outlined above. Results are given for two p_T cuts and different muon charges. Only the statistical uncertainties are reported.

Chapter 8

Results Cross Section Measurement

The determination of the cross sections is based on the standard formula:

$$\sigma = \frac{N_{tot} - N_{bkg}}{A \cdot \epsilon \cdot L} \ . \tag{8.1}$$

As described in Section 5 the treatment of the factor $A \cdot \epsilon$ is similar for the processes $pp \to Z/\gamma^* + X \to \mu\mu + X$ and $pp \to W^{\pm} + X \to \mu\nu + X$, involving the full factor $A' = A \cdot \epsilon$ and a data-driven efficiency correction $(\epsilon_{data}/\epsilon_{MC})$. The luminosity and its uncertainty are external input from [24]. The treatment of the numerator in Equation 8.1 is different for the Z and $W^{\pm}$ signals.
The experimental cross section results derived in this thesis are compared to the theoretical predictions from [55].

8.1 Results Z Cross Section

Since the expected background after the selection of Z events is at the permille level and the same-sign background estimation carried out in Chapter 5 is in agreement with the expectation from simulation in the *tag-pass* categories, no background subtraction is performed and the full background expectation from the simulation is taken as a systematic uncertainty. A total of 12065 events pass the Z selection and are taken as the number of signal events N_{sig}. The cross section is determined according to:

$$\sigma_Z = \frac{N_{sig}^Z}{(A_Z \cdot \epsilon_Z)^{MC} \cdot \left(\frac{\epsilon_{data}^{TP}}{\epsilon_{MC}^{TP}}\right)_Z \cdot L} \ . \tag{8.2}$$

The systematic uncertainties for the Z cross sections are summarized in Table 8.1. The dominant uncertainty is the one on the luminosity taken as 4% according to [24]. The uncertainty on the selection efficiency enters the cross section determination via the efficiency correction factor $\epsilon_{data}^{TP}/\epsilon_{MC}^{TP}$. Its relative statistical and systematic uncertainties reported in Chapter 5 are added in quadrature and taken as the systematic uncertainty on the selection efficiency. The uncertainty due to the muon momentum scale has not been studied in the context of this thesis and is taken from [55]. The theoretical uncertainty has been discussed in Chapter 5.
The result of the Z/γ^* cross section measurement in the range 60 GeV $< M_{\mu\mu} <$ 120 GeV reads:

$$\sigma_{pp \to Z/\gamma^*+X} \cdot \mathrm{BR}\,(Z/\gamma^* \to \mu\mu) = 0.955 \pm 0.009\ (\mathrm{stat}) \pm 0.015\ (\mathrm{exp}) \pm 0.018\ (\mathrm{theo}) \pm 0.038\ (\mathrm{lumi})\ \mathrm{nb} \tag{8.3}$$

The systematic uncertainties dominate the total uncertainty. The leading systematic uncertainty is due to the one on the luminosity. The other experimental systematic uncertainties of are comparable to the theoretical uncertainty on the acceptance.
The result is in agreement with the theoretical prediction of 0.97 ± 0.04 nb [55].

source	syst. uncertainty σ_Z [%]
luminosity	4
selection efficiency	1.5
Background	0.4
muon momentum scale & resolution	0.4
total experimental	1.6
theoretical	1.9

Table 8.1: Breakdown of the systematic uncertainties on the Z cross sections in percent.

8.2 Results $W^{\pm}$ Cross Sections

The number of signal events for the cross section determination in the $W^{\pm} \to \mu\nu$ case is based on a binned extended likelihood [66] fit of a model of two templates to the M_T distributions. One fit is performed per electric charge of the reconstructed lepton. The fit is carried out with the RooFit package [67].
The two templates are a QCD template derived on the data with the semi-isolated approach discussed in Section 7 and a second template comprising the signal $W \to \mu\nu$ and the leading electroweak backgrounds $W \to \tau\nu$, $Z/\gamma^* \to \mu\mu$, $Z/\gamma^* \to \tau\tau$ and $t\bar{t}$. Two fit parameters are determined, N_{QCD} and N_{EWK}. An overview of the expected signal and background contributions according to the simulation and the data-driven QCD background determination described in Chapter 7 is given in Table 8.2.

N/N_{tot}	W^+ [%]	W^- [%]
QCD	9.3	12.6
$t\bar{t}$	0.3	0.4
$Z \to \tau\tau$	0.4	0.6
$W \to \tau\nu$	2.5	2.5
$Z/\gamma^* \to \mu\mu$	3.0	3.7
$\sum$ EWK	6.2	7.2
$W \to \mu\nu$	84.5	80.2

Table 8.2: Relative contribution of different processes in percent after $W^+ \to \mu\nu$ and $W^- \to \mu\nu$ selection as expected from simulation. Electroweak contributions are scaled to NNLO (NLO $t\bar{t}$) cross section. The number of QCD events is taken from the data-driven approach described in Chapter 7.

The region of low transverse mass is dominated by the QCD multijet background and the $W^{\pm} \to \mu\nu$ signal exhibits the characteristic Jacobian peak. The small electroweak background peaks within 50 GeV $< M_T <$ 60 GeV, close to the peak of the signal, and has a broad distribution. A fit involving a third template comprising the electroweak backgrounds only would not be sensitive to this contribution. Therefore, the electroweak backgrounds are included in the signal template. The weight of the individual contributions in the electroweak template involves the cross section ratio with respect to the signal, i.e. all electroweak cross sections are expected to scale with the $W \to \mu\nu$ signal cross section. The cross sections are fixed to the theoretical NNLO calculations. The leading electroweak backgrounds are $W \to \tau\nu$ and $Z/\gamma^* \to \mu\mu$. For the $W \to \tau\nu$ background the cross section ratio is expected to scale exactly with the signal cross section. A variation of the W/Z cross section ratio within 5% is expected to yield a variation of the extracted $W \to \mu\nu$ cross section at the level of a few permille.
The shape and total selection efficiency $A \cdot \epsilon$ of the electroweak background contributions are taken directly from the POWHEG simulation for the W/Z samples and the PYTHIA sample for $t\bar{t}$. The

signal template is taken from the POWHEG simulation without pileup with the data-driven recoil correction discussed in Chapter 6. The formula for the fit model $\mathcal{M}(M_T)$ reads:

$$\mathcal{M}(M_T) = N_{EWK} \cdot \left[\frac{\sum\limits_{i,\mathrm{EWK}} \sigma_i \cdot (A_i \epsilon_i) \cdot \mathcal{D}_i}{\sum\limits_{i,\mathrm{EWK}} \sigma_i \cdot (A_i \epsilon_i)} \right] + N_{QCD} \cdot \mathcal{D}_{QCD} \ , \tag{8.4}$$

with the normalized M_T distributions of the individual contributions after $W \rightarrow^{\pm} \mu\nu$ selection, $\mathcal{D}_i$.

The fit is performed in the M_T region 0 GeV $< M_T <$ 120 GeV with a binning of 1 GeV, ensuring a number of data events per bin greater than 10. The fit results are shown in Figures 8.1 and 8.2.

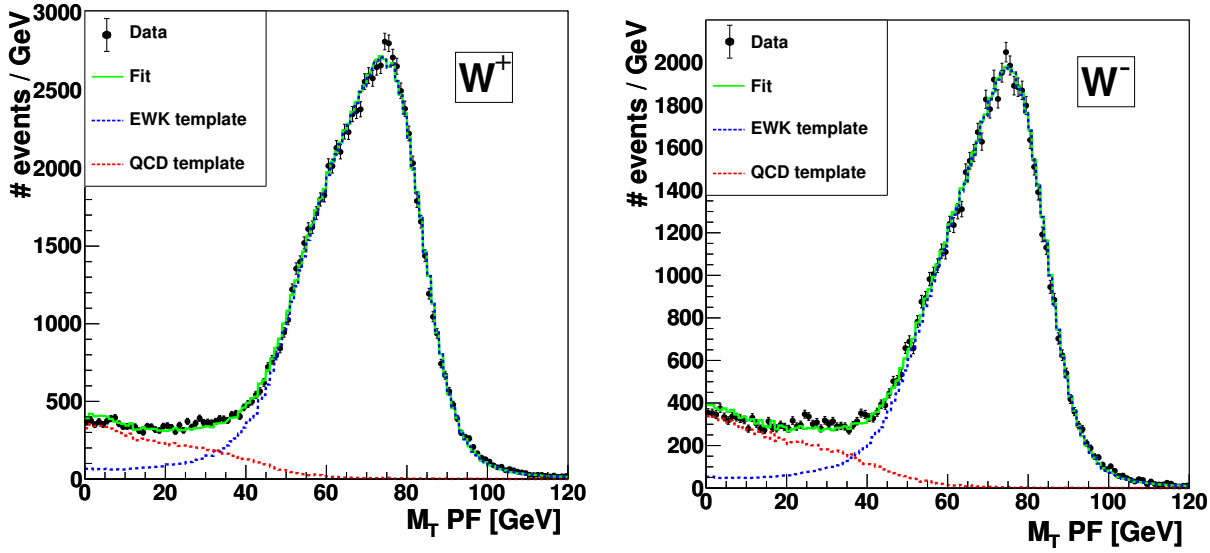

(a) Fit after $W^+ \rightarrow \mu\nu$ selection.

(b) Fit after $W^- \rightarrow \mu\nu$ selection.

Figure 8.1: Fit with two templates to the M_T distribution after $W^{\pm} \rightarrow \mu\nu$ selection. The central values of the data-driven recoil modelling are used for the signal template and the QCD template is obtained from data.

The agreement between the fitted templates and the data is significantly improved when changing from the simulation without pileup to the (partially) data-driven templates. The χ^2/ndf improves from 11.74 to 1.95 in the case of the $W^+ \rightarrow \mu\nu$ selection. The χ^2/ndf values are reported in Table 8.3 for different combinations of the signal and QCD input templates.

templates (signal / QCD)	χ^2/ndf W^+	χ^2/ndf W^-
recoil / data-driven	1.95	1.97
recoil σ_{U_i} up / data-driven	1.91	1.76
recoil σ_{U_i} down / data-driven	2.52	2.35
pileup MC / data-driven	1.78	2.13
non-pileup MC / data-driven	8.37	8.61
non-pileup MC / MC	11.74	12.43

Table 8.3: χ^2/ndf of the two parameter fit for different choices of the QCD and signal template. The variation of the widths in the recoil modelled signal template by $\pm 1\sigma$ are denoted by 'up' and 'down'.

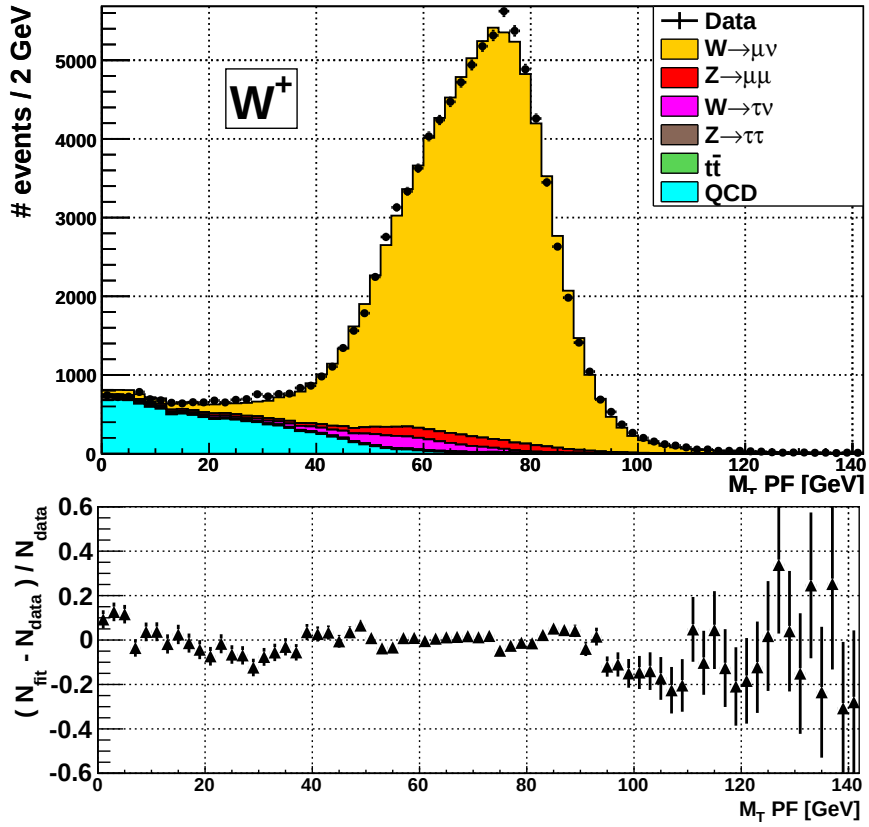

(a) Fit after $W^+ \to \mu\nu$ selection.

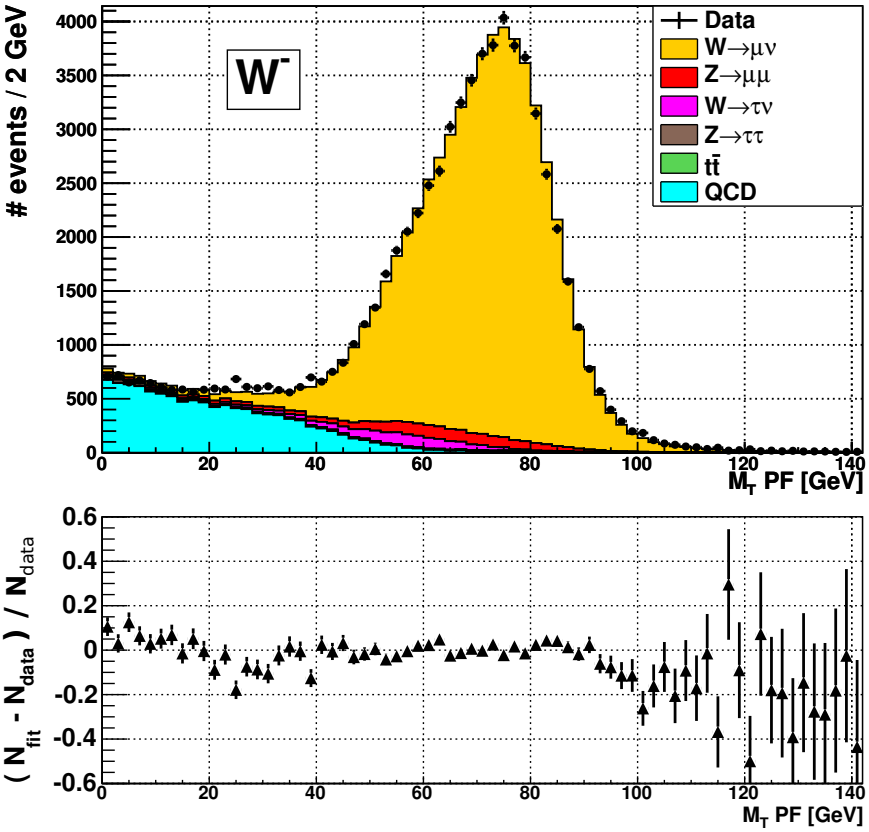

(b) Fit after $W^- \to \mu\nu$ selection.

Figure 8.2: Individual contributions after scaling according to the fit result.

As depicted in Figure 8.2, small discrepancies between the fit and the data increasing the χ^2/ndf arise mainly in the QCD dominated region $M_T < 40\ GeV$ and in the tail of the signal distribution $M_T > 90\ GeV$. The imperfection in the shape of the QCD template from semi-isolated events in the case of PF $\not\!\!E_T$ is expected from the discussion in Chapter 7. The underestimation of the signal yield in the tail of the M_T distribution can be explained by the overestimation of the hadronic recoil width with the single-Gaussian model. Due to the increased $\not\!\!E_T$ width, too many events are smeared out of the peak into the region of the sharp Jacobian edge. The number of events in the region of the edge is increased, wheras the tail of the distribution does not receive as many additional events due to the overestimated smearing of the peak. However, a simple reduction of the hadronic recoil width used in the recoil modelling does not improve the overall χ^2/ndf as indicated by the values in 8.3. As mentioned before, the shape does not have a significant impact on the determination of the $W^{\pm}$ cross section. The comparison of different signal templates is carried out in Chapter 9.

The number of signal events N_{sig} is extracted from the fit result of N_{EWK} according to the fit model $\mathcal{M}(M_T)$ in Equation 8.4:

$$N_{sig}^{W^{\pm}} = \frac{N_{EWK}}{\sum\limits_{i,\mathrm{EWK}} \frac{\sigma_i}{\sigma_{W^{\pm}}} \cdot \frac{A_i \epsilon_i}{A_{W^{\pm}} \epsilon_{W^{\pm}}}} \ . \tag{8.5}$$

And the cross section is calculated according to:

$$\sigma_{W^{\pm}} = \frac{N_{sig}^{W^{\pm}}}{\left(A_{W^{\pm}} \cdot \epsilon_{W^{\pm}}\right)^{MC} \cdot \left(\frac{\epsilon_{data}^{TP}}{\epsilon_{MC}^{TP}}\right)_{W^{\pm}} \cdot L} \ . \tag{8.6}$$

The results for the fit parameters and N_{sig} are reported in Table 8.4.

	N_{EWK}	N_{sig}	N_{QCD}
W^+	91516 ± 314	85292 ± 292	10962 ± 133
W^-	62752 ± 261	57548 ± 239	10551 ± 125

Table 8.4: Fit result for $W^{\pm}$.

The systematic uncertainties for the W cross sections for both charges are summarized in Table 8.5. The dominant uncertainty is the one on the luminosity taken as 4% according to [24]. The uncertainty on the selection efficiency enters the cross section determination via the efficiency correction factor $\epsilon_{data}^{TP}/\epsilon_{MC}^{TP}$. Its relative statistical and systematic uncertainty reported in Chapter 5 are added in quadrature and taken as the systematic uncertainty on the selection efficiency. The QCD background uncertainty is derived by fitting both the data-driven template and the template from simulation. The full difference on the resulting cross section is taken as the systematic uncertainty. Considering the severe improvement when exchanging the simulated template by the data-driven one, the estimate of the systematic uncertainty due to the QCD background is conservative. The systematic uncertainty associated with the electroweak backgrounds in the fitted electroweak template is determined by varying their weights by $\pm 5\%$ with respect to the $W^{\pm}$ signal and taking the full difference in the resulting cross sections as the systematic uncertainty. The systematic uncertainty due to the modelling of the $\not\!\!E_T$ shape is taken as the difference between the cross section results obtained with the signal template from simulation without pileup and the template after recoil modelling. The uncertainty on the jet energy scale (JES) is estimated by varying the JES by $\pm 4\%$ as suggested in [76]. The uncertainty due to the muon momentum scale has not been studied in the context of this thesis and is taken from [55]. The theoretical uncertainty has been discussed in Chapter 5.

The total experimental uncertainty without luminosity amounts to 2.5% and 2.8% for the W^+ and W^- cross sections, respectively. It is larger than the uncertainty on the acceptance, which is of

	systematic uncertainty		
source	W^+ [%]	W^- [%]	W [%]
luminosity	4	4	4
selection efficiency	1.9	1.9	1.9
QCD background	1.4	1.9	1.6
EWK background	0.7	0.8	0.7
$\not\!\!E_T$ shape	0.3	0.3	0.3
JES	< 0.1	< 0.1	< 0.1
muon momentum	0.2	0.3	0.2
total experimental	2.5	2.8	2.6
theoretical	1.2	1.4	1.1

Table 8.5: Breakdown of the systematic uncertainties on the $W^{\pm}$ and the full W cross sections in percent.

theoretical nature, by about a factor 2. The systematic uncertainties clearly dominate the overall uncertainty. The statistical uncertainty amounts to 3-4 permille. The theoretical uncertainty on the NNLO calculations to be compared with the measurements are about 4-5% for the W^+ and W^- cross sections. The numbers for the $W^{\pm}$ cross sections are summarized in Equations 8.7 and 8.8.

$$\sigma_{pp \to W^+ + X} \cdot \mathrm{BR}\,(W \to \mu\nu) = 5.89 \pm 0.02\ (\mathrm{stat}) \pm 0.15\ (\mathrm{exp}) \pm 0.07\ (\mathrm{theo}) \pm 0.24\ (\mathrm{lumi})\ \mathrm{nb} \quad (8.7)$$

$$\sigma_{pp \to W^- + X} \cdot \mathrm{BR}\,(W \to \mu\nu) = 4.10 \pm 0.02\ (\mathrm{stat}) \pm 0.11\ (\mathrm{exp}) \pm 0.06\ (\mathrm{theo}) \pm 0.16\ (\mathrm{lumi})\ \mathrm{nb} \quad (8.8)$$

The results are in agreement with the NNLO predictions 6.15±0.29 nb and 4.29±0.23 nb. As in the case of the Z cross section, the measured cross sections are smaller than the theory predictions.

The fit to the full W yield including both charges gives 142828 signal events. The resulting cross section is given in Equation 8.9 and is found to agree with the theoretical prediction of 10.44 ± 0.52 nb.

$$\boxed{\sigma_{pp \to W + X} \cdot \mathrm{BR}\,(W \to \mu\nu) = 9.97 \pm 0.03\ (\mathrm{stat}) \pm 0.26\ (\mathrm{exp}) \pm 0.10\ (\mathrm{theo}) \pm 0.40\ (\mathrm{lumi})\ \mathrm{nb}} \quad (8.9)$$

The individual inclusive cross sections are compared to the official CMS results [55] and the theoretical prediction in Figure 8.3.

8.3 Results Cross Section Ratios

The measurements of the ratios of inclusive cross sections W^+/W^- and W/Z are an important test of the standard model at early LHC data taking. The dominant experimental uncertainty associated with the luminosity cancels in the ratios, allowing for a more stringent test of the theoretical predictions than the individual inclusive cross section values.

For the discussion of the systematic uncertainties it is instructive to decompose the cross section ratios into three factors:

$$\frac{\sigma_{W^+}}{\sigma_{W^-}} = \frac{N_{W^+}}{N_{W^-}} \frac{\epsilon_{W^-}}{\epsilon_{W^+}} \frac{A_{W^-}}{A_{W^+}} \quad (8.10)$$

$$\frac{\sigma_W}{\sigma_Z} = \frac{N_W}{N_Z} \frac{\epsilon_Z}{\epsilon_W} \frac{A_Z}{A_W}\,. \quad (8.11)$$

The first term involves the yields of selected events and comprises the statistical uncertainty and the uncertainty associated with the background estimation as the leading systematic uncertainty on this factor. The latter are reduced in the case of the W^+/W^- cross section ratio

compared to the individual cross section measurements. The systematic uncertainties on the overall efficiency factors cancel to some extent for both cross section ratios. The systematic uncertainties on the acceptance ratios are given in Table 5.6 and are found to be larger than for the individual cross section measurements.

The systematic uncertainties on the W^+/W^- cross section ratio are determined as follows: The influence of QCD background is carried out as for the individual cross section measurements and the ratio is determined for the different background shapes used in the fit. The full difference is taken as the systematic uncertainty due to the QCD background. The difference of the individual systematics associated with the electroweak backgrounds for the W^+ and W^- measurements is used as the corresponding systematic uncertainty on the ratio. The treatment of the $\not\!\!E_T$ shape uncertainty is carried out by determining the ratios for the non-pileup simulated signal shape and the signal template after recoil modelling and taking the full difference as the systematic uncertainty. For the uncertainty on the efficiency factor the full difference between the data-driven efficiency measurements for the different muon charges is taken. The systematic uncertainty associated with muon momentum scale and resolution is quoted from [55].

In the case of the W/Z cross section ratio the background and $\not\!\!E_T$ shape uncertainties are directly propagated from the W cross section measurement. When the different muon kinematics in $W \to \mu\nu$ and $Z/\gamma^* \to \mu\mu$ events are neglected, the factor ϵ_Z/ϵ_W takes the form:

$$\frac{\epsilon_Z}{\epsilon_W} \approx \epsilon_{Reco}\ \epsilon_{Iso}\ \frac{1-(1-\epsilon_{Trigger})^2}{\epsilon_{Trigger}}\ . \tag{8.12}$$

This factor is varied within the systematic uncertainties assigned to the efficiencies $\epsilon_{Reco} \cdot \epsilon_{Iso}$ and $\epsilon_{Trigger}$ in Chapter 5, 1% and 1.5%, respectively. Half the difference of the results obtained by varying ϵ_Z/ϵ_W by $\pm 1\sigma$ is added to the background uncertainty on the efficiency factor in quadrature.
The systematic uncertainties on the cross section ratios are reported in Table 8.6.

source	syst. uncertainty $\frac{\sigma_{W^+}}{\sigma_{W^-}}$ [%]	syst. uncertainty $\frac{\sigma_W}{\sigma_Z}$ [%]
selection efficiency	0.5	0.6
QCD background	0.4	1.6
EWK background	0.1	0.7
$\not\!\!E_T$ shape	0.1	0.3
muon momentum	< 0.1	0.4
total experimental	0.7	1.9
theoretical	2.0	2.1

Table 8.6: Breakdown of the systematic uncertainties on the W^+/W^- and W/Z inclusive cross section ratios in percent.

The results on the inclusive cross section ratios read:

$$\frac{\sigma_{pp \to W^+ + X}}{\sigma_{pp \to W^- + X}} = 1.435 \pm 0.008\ (\text{stat}) \pm 0.010\ (\text{exp}) \pm 0.029\ (\text{theo}) \tag{8.13}$$

$$\frac{\sigma_{pp \to W+X} \cdot \text{BR}\,(W \to \mu\nu)}{\sigma_{pp \to Z/\gamma^*+X} \cdot \text{BR}\,(Z/\gamma^* \to \mu\mu)} = 10.44 \pm 0.10\ (\text{stat}) \pm 0.20\ (\text{exp}) \pm 0.22\ (\text{theo})\ . \tag{8.14}$$

The measurements agree with the theoretical predictions of 1.43 ± 0.04 and 10.74 ± 0.04 for the W^+/W^- and W/Z cross section ratios, respectively. A comparison with the official CMS results [55] and the theoretical prediction is shown in Figure 8.3.

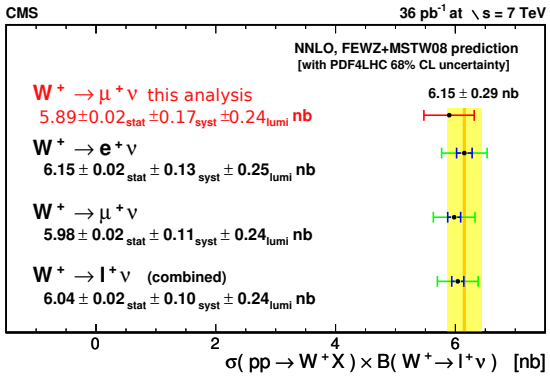

(a) Result inclusive $W^+ \to \mu\nu$ cross section.

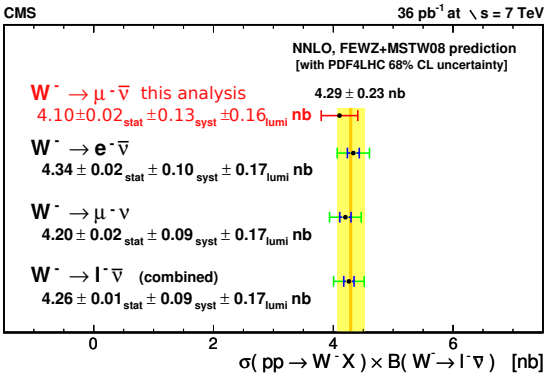

(b) Result inclusive $W^- \to \mu\nu$ cross section.

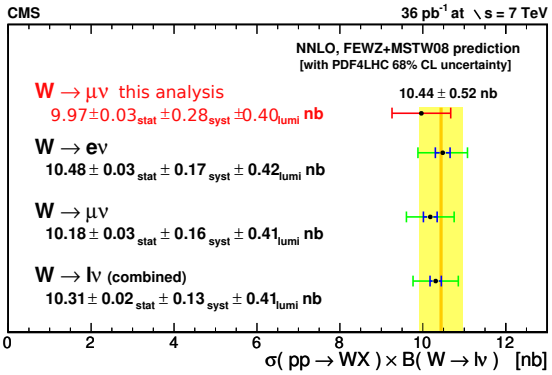

(c) Result inclusive $W \to \mu\nu$ cross section.

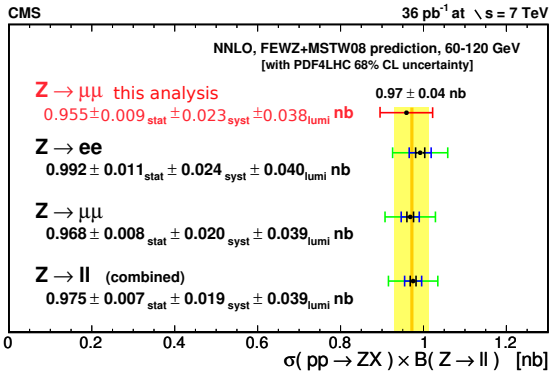

(d) Result inclusive $Z/\gamma^* \to \mu\mu$ cross section.

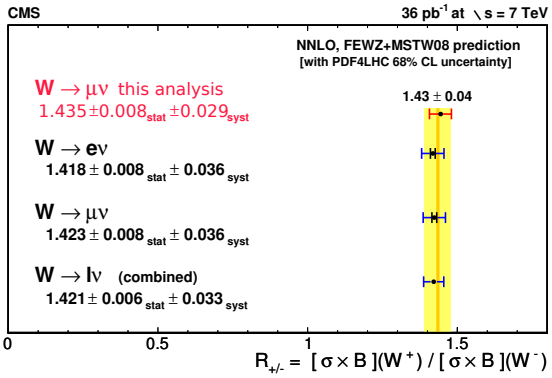

(e) W^+/W^- cross section ratio.

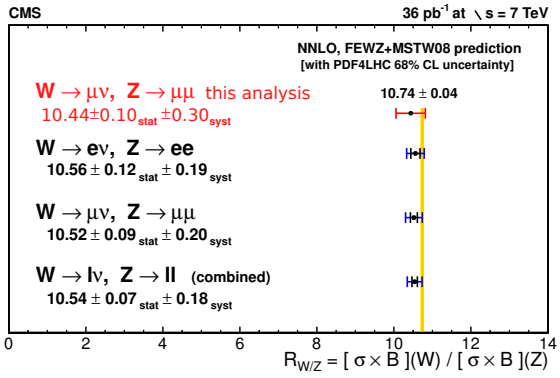

(f) W/Z cross section ratio.

Figure 8.3: Comparison of the results on the inclusive cross sections measurements (red) to the official CMS results and the theoretical prediction (orange line). The plots are taken from [55]. The uncertainties in the plot are determined by adding the systematical uncertainties (without luminosity) in quadrature and adding the result to the statistical uncertainty and the uncertainty on the luminosity.

Chapter 9

W Mass Determination

9.1 Motivation

In the context of renormalization, tree-level relations between Standard Model parameters are modified. The renormalization procedure introduces additional terms in the tree-level relations (depending on the renormalization scheme) that are referred to as radiative corrections. The mass of the W boson can be expressed at tree-level as a function of the Fermi constant G_F, the fine-structure constant α, and the mass of the Z boson M_Z. When higher-order corrections are included, the relation is modified by a radiative correction Δr [77]:

$$M_W^2 = \frac{M_Z^2}{2}\left(1 + \sqrt{1 - 4\frac{\pi\alpha}{\sqrt{2}G_F M_Z^2}\frac{1}{1-\Delta r}}\right) . \tag{9.1}$$

The radiative correction Δr exhibits a dependence on both the mass of the top quark, and the mass of the Higgs boson. Precise measurements of the W mass, the top mass, and (if it exists) the Higgs mass can be used to test the Relation 9.1 and therefore the Standard Model at loop level.

9.2 Introduction

In order to determine the mass of the W boson M_W the distribution to be fitted has to be chosen. The process $W \to \mu\nu$ provides three obvious options:

- Distributions of the decay products that exhibit a Jacobian peak signature.
  - The $\not{E}_T$ distribution associated with the neutrino in the final state. The $\not{E}_T$ distribution is sensitive to the entire event topology. This includes the underlying event and pileup. An accurate modelling of the hadronic recoil in W events is necessary to avoid a bias in the M_W measurement.
  - The p_T distribution of the muon. As a physics object, the muon with its clear signature in the detector, the reliable tagging and triggering in the muon system and the precise transverse momentum measurement in the tracker is the natural candidate to provide the distribution used for the fit. However, the kinematics of $W \to \mu\nu$ production have to be considered in the choice of the distribution.

  Both $\not{E}_T$ and muon p_T are sensitive to a boost of the W in the transverse plane, i.e. to the W p_T distribution. This sensitivity to the W kinematics translates into a sensitivity of the W mass fit to the muon momentum scale and resolution and the $\not{E}_T$ scale and resolution from the experimental point of view.

- The transverse mass distribution M_T that also exhibits a Jacobian peak. The virtue of this distribution is that it is less sensitive to the W p_T. It is therefore the most characteristic distribution of the W boson at hadron colliders and has a smaller QCD background contamination than $\not\!\!E_T$ and muon p_T.

For the studies on the W mass presented here, the M_T distribution is chosen. Both the $\not\!\!E_T$ and muon p_T distributions require an investigation of the W p_T on data, which involves the hadronic recoil in W events on data. Since only the hadronic recoil in Z data events has been used for the hadronic recoil modelling in this thesis and the hadronic recoil in W events has only been used for cross checks, the distribution with the smallest dependency on the W p_T, i.e. M_T, is chosen. Also fits to the M_T distributions yield the smallest systematic uncertainty on M_W in the detailled analyses performed by D0 [78] and CDF [79] at TEVATRON.

9.3 Fit Method

Compared to the cross section measurement, the priority of the selection is shifted from high signal efficiency to high purity. For simplicity only selection criteria that are expected to show a small correlation with M_T are tightened. Two cuts in the selection of W events described in the context of the cross section measurement are tightened, mainly in order to reject QCD events:

- The muon isolation criterion is changed from $I_{rel} < 0.15$ to $I_{rel} < 0.05$.
- The very loose cut on the transverse impact parameter |d0| is changed from |d0| < 0.2 cm (cosmics rejection) to |d0| < 0.01 cm (cosmics rejection and QCD rejection).

Apart from the choice of the M_T fit window no $\not\!\!E_T$-based cuts are applied.

Fitting the W mass relies on the exact modelling of both the hard process and the underlying event involving pileup. Including all of the information necessary in an analytic function that fits to the data is complicated. Instead simulated distributions are used and the hadronic recoil is modelled as described in Section 6.3. As before, the NLO generator POWHEG is used for the signal simulation, interfaced with PYTHIA for parton showering. The generation of simulated samples for each M_W input value is time-consuming and unnecessary at the early stage of this analysis. Instead, the POWHEG samples for W^+ and W^- from the official production are combined to a W sample with the numbers of W^+ and W^- events according to the W^+/W^- inclusive cross section ratio and then a reweighting of the distribution to different values of M_W is carried out. The event weights $w^{in}_{M_W}$ are defined as the ratio of the relativistic Breit-Wigner functions for the chosen input W mass M^{in}_W and the default value $M^{MC}_W = 80.45$ GeV used in the sample production:

$$w^{in}_{M_W} = \frac{\left(\hat{s} - \left(M^{MC}_W\right)^2\right)^2 + \left(M^{MC}_W\right)^2 \Gamma^2_W}{\left(\hat{s} - \left(M^{in}_W\right)^2\right)^2 + \left(M^{in}_W\right)^2 \Gamma^2_W} \,, \tag{9.2}$$

with the effective center-of-mass energy $\hat{s} \equiv M_{\mu\nu}$ evaluated event by event. The invariant mass $M_{\mu\nu}$ is calculated with the muon state vector at generator level before final state radiation. The spacing between the input masses M^{in}_W is 25 MeV, smaller than the statistical and systematic uncertainties on the W mass. The principle of this reweighting is illustrated in Figure 9.1.

The signal samples after reweighting are combined with the electroweak background samples in the same fashion as for the cross section fits. The simulation including pileup is used for the backgrounds. The M_T range used for the fit is 55 GeV $< M_T <$ 95 GeV ensuring the rejection of QCD to a negligible level (see Figure 8.2) compared to other sources of systematic uncertainty and more than 400 data events per 1 GeV transverse mass bin. A binned likelihood fit is carried out with RooFit [67] with a binning of 1 GeV, well below the experimental resolution of M_T. For each input W mass the χ^2 is extracted and the result of the fit M^{fit}_W is taken as the minimum of

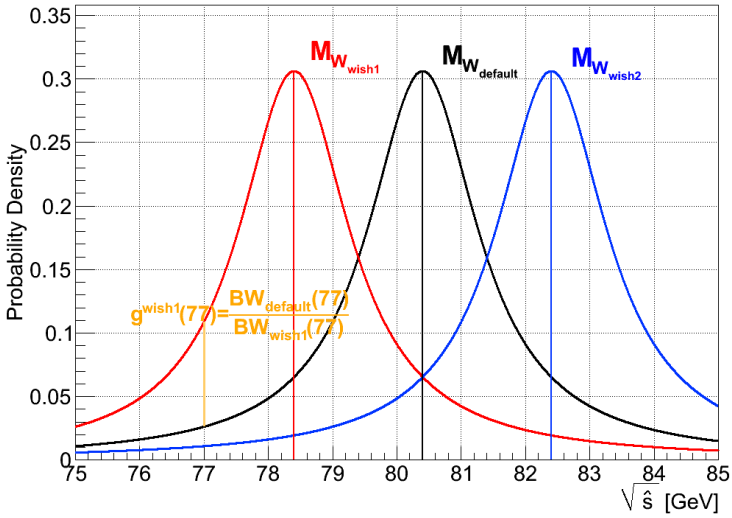

Figure 9.1: Principle of the reweighting method by courtesy of Dipl. Phys. Metin Ata.

the fitted χ^2 parabola, which also gives an estimate of the statistical uncertainty via $\chi^2\left(M_W^{fit} \pm \sigma_{stat}^{M_W}\right) = \chi^2_{min} + 1$.

9.4 Leading Systematic Uncertainties

Before turning to the result of the fit a study of the expected leading sources of systematic uncertainties and potential bias, the hadronic recoil modelling and the muon momentum scale, are discussed.

9.4.1 Muon Momentum Scale

Detailed studies of the muon momentum scale and calibration techniques in CMS are reported in [37]. One result is that the bias due to the muon momentum scale in the data used for this thesis is different for the low p_T range 1 GeV $< p_T^\mu <$ 10 GeV and the intermediate p_T range 20 GeV $< p_T^\mu <$ 100 GeV, because the latter is more sensitive to effects of misalignement. Therefore an estimate on the muon momentum scale uncertainty on the W mass with the high J/ψ statistics is not feasible.

Instead of using a calibrated muon momentum scale, the following ad hoc approach utilizing Z events is used: The fit method described in the previous section is used on the Z simulated sample and the invariant mass distribution after the standard Z selection in data is fitted. The resulting mass M_Z^{fit} is compared to the world average value of $M_Z = 91.1876 \pm 0.0021$ GeV [8]. The result of the fit is shown in Figure 9.2.

The fit result reads:

$$M_Z^{fit} = 91.132 \pm 0.028 \text{ (stat) GeV} . \tag{9.3}$$

The world average lies within 2σ of the statistical uncertainty. For the estimate of the systematic uncertainty, the full difference between the world average and the fit result is interpreted as a shift due to the muon momentum scale and half of it is propagated as the systematic uncertainty on the W mass due to the muon momentum scale ($\approx$ 30 MeV). The muon momentum resolution is tested by a Voigtian fit (non-relativistic Breit-Wigner folded with a Gaussian) to the data with the width of the Breit-Wigner fixed to the Z width. The fit is performed to both the simulation and the data and the results on the Gaussian width that is associated with the muon momentum

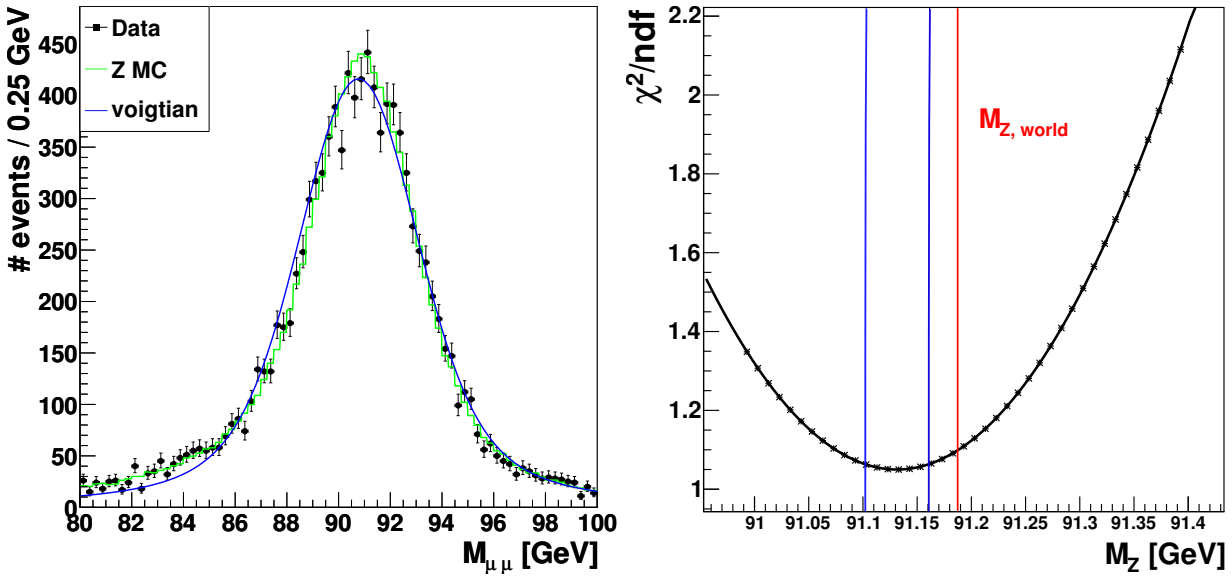

Figure 9.2: Left: Best fit of the Z simulation (green) to the Z selected data. For comparison, the result of a Voigtian fit with its bias to a lower peak position due to QED final state radiation is also shown. Right: The χ^2/ndf parabola of the fit (different M_Z templates) with the world average value (red) and the statistical uncertainties on the minimum (blue).

resolution are 1.71 ± 0.01 GeV and 1.77 ± 0.04 GeV, respectively. The simulation reproduces the resolution observed in data well. In total an uncertainty of 50 MeV due to the muon momentum scale and resolution is assigned to the W mass fit result.

9.4.2 Hadronic Recoil Model

The W mass fit is sensitive to the hadronic recoil in W events. Considering that a modelling of the underlying event and pileup that increases with the rising number of events per bunch and reduced spatial dimension of the beams at start-up of the accelerator is challenging, the hadronic recoil is expected to be the dominant source of systematic uncertainty on the W mass. This will be quantified in the following using three different methods to model the hadronic recoil:

- Extracting the hadronic recoil from Z events on data. This approach involves the recoil distributions of the components U_1 and U_2 binned in Z p_T.
  - Gaussian fits to U_1 and U_2. This method provides a method of evaluating the systematic uncertainties associated with the recoil modelling by varying the recoil model within its uncertainties and thereby propagating the statistical uncertainties on the fit parameters (Z statistics) to the desired quantity. One disadvantage of this method is the overestimated width of the recoil as discussed in Section 6.3. This method is referred to as the Gaussian method in the following.
  - Instead of fitting the recoil distributions and parameterizing the recoil model, the distributions of U_1 and U_2 can be taken directly from Z events. The recoil is then mixed into the simulation with random numbers diced according to these histograms. This approach is called the direct extraction method in the following.
- Using the vertex-reweighted pileup simulation. The study of systematic uncertainties with this method would involve a variation of the input parameters for the pileup in the simulation and has not been carried out in the context of this thesis.

The results of all three methods are compared. The Gaussian method is used to obtain the systematic uncertainty on M_W due to the hadronic recoil.
The two methods that exploit Z events are tested on the simulation in order to detect biases of the recoil modelling on M_W. The overestimated width of the Gaussian hadronic recoil model enhances the edge of the Jacobian and leads to signal templates the shape of which is biased towards higher M_W. The fit result M_W^{fit} is then expected to be biased towards a smaller W mass. This qualitative assumption is tested and quantified on the simulation.
For this purpose the recoil modelling is run on the W simulated sample where the vector boson p_T necessary for the modelling is available at generator level and the resulting recoil parameterization is used to recalculate $\not\!\!E_T$. Then the W mass reweighting is carried out and the fit procedure is applied to the original M_T distribution in the simulation.

recoil model	M_W^{fit} [GeV]	ΔM_W^{recoil} [GeV]
Gaussian	80.35	−0.10
direct extraction	80.36	−0.09

Table 9.1: Fit results on the W mass obtained from a closure test of the fit of the recoil-modelled simulation to the original distribution in the simulation. The result of the fit on the data is corrected for the shifts ΔM_W^{recoil} with respect to the input W mass used for simulation of 80.45 GeV.

For both methods involving Z events a bias towards lower values of the fit result M_W^{fit} with respect to the input W mass is observed. The results and shifts in the W mass, ΔM_W^{recoil}, are reported in Table 9.1. The results obtained from the fit to the data are corrected for these shifts found in the simulation.
The minimum of the χ^2/ndf is reduced by a factor of 0.35 when changing from the Gaussian model to the direct extraction method. The shifts reported in Table 9.1 provide a measure of the systematic uncertainty due to recoil modelling expected from simulation of approximately 100 MeV.

9.5 Results of the W Mass Fit

The results of the W mass fit for the three different recoil models are summarized in Table 9.2. The associated best fit templates are compared to the data in Figures 9.3 (a)-(c) and a comparison of the χ^2/ndf parabolae is given in Figure 9.3 (d).

recoil model	M_W^{fit} [GeV]	M_W^{fit} [GeV] corrected	$\chi^2/ndf\ \vert_{min}$	χ^2 prob. [%]
Gaussian	80.330 ± 0.046 (stat)	80.430 ± 0.046 (stat)	1.56	13
direct extraction	80.336 ± 0.046 (stat)	80.426 ± 0.046 (stat)	1.09	32
pileup	80.571 ± 0.045 (stat)	–	1.24	15

Table 9.2: Fit results for the different recoil models. The corrected values in the third column include the shifts from Table 9.1.

All three recoil models show a reasonable agreement with the data (χ^2 probability $> 10\%$) and the fit results for the W mass lie within approximately 150 MeV. As described in the following, this difference is covered by the systematic uncertainties on the recoil modelling that are derived independently from the results in Table 9.2. Moreover the residuals of the fit with the simulation including pileup in Figure 9.3 (c) show that in this case the fitted template overestimates the distribution in the peak region 70 GeV $< M_T <$ 85 GeV except for the two bins in the range 74 GeV $< M_T <$ 76 GeV which are interpreted as a statistical fluctuation upward in the data. This points towards an underestimated width of the recoil in the simulation including pileup (after reweighting to the good vertex distribution observed in data), which would bias the result on the W mass to a higher value.

As shown by the residuals in Figure 9.3 (b), the Gaussian recoil model overestimates the width in the peak region, smearing events out of the region 71 GeV $< M_T <$ 82 GeV into the adjacent bins. This shortcoming of the data-driven recoil modelling is not present in the case of the direct extraction. All in all, the best agreement between the fit and the data is achieved with the direct extraction method and the associated result is taken as the final result.

The systematic uncertainties are evaluated as follows:

- The uncertainty due to the hadronic recoil modelling is derived based on the variation of the fit parameters using the Gaussian recoil model as described in Section 6.3. The uncertainties split into a contribution associated with the mean and the width of the hadronic recoil read:

$$\Delta_{M_W}^{width} = \frac{1}{2}\,|M_W^{width,up} - M_W^{width,down}| \approx 78 \text{ MeV} \tag{9.4}$$

$$\Delta_{M_W}^{mean} = \frac{1}{2}\,|M_W^{mean,up} - M_W^{mean,down}| \approx 86 \text{ MeV} \tag{9.5}$$

$$\Rightarrow \Delta_{M_W}^{recoil} = \sqrt{\left(\Delta_{M_W}^{width}\right)^2 + \left(\Delta_{M_W}^{mean}\right)^2} \approx 116 \text{ MeV}\ . \tag{9.6}$$

- The uncertainty due to muon momentum scale and resolution is given in Section 9.4 and amounts to 50 MeV.

- The fitted W mass depends on the choice of the M_T range used in the fit. The fit is performed in a broader range 50 GeV $< M_T <$ 100 GeV and a tighter range 40 GeV $< M_T <$ 90 GeV and half the difference is taken as the uncertainty associated with the choice of the fitted M_T range (and the efficiency of the M_T cut). The uncertainty amounts to 29 MeV.
  The stability of the fit result under a variation of the fit range is tested further by including the W M_T tail up to 125 GeV (> 10 data events per bin). The result differs from the value reported above by -26 MeV and the agreement between the fit and the data does not change significantly, $\chi^2/ndf = 1.17$. A corresponding variation in the low M_T region is not possible without further cuts because of the QCD background.

- The influence of the jet energy scale is determined by a variation of $\pm 4\%$. The uncertainty of 20 MeV is smaller than the recoil uncertainty, which is explained by the fact that the hadronic energy in W events is typically unclustered rather than resulting in hard jets. This jet energy scale contribution is not included in the total systematic uncertainty since it is part of the hadronic recoil uncertainty.

- The total acceptance factors $A \cdot \epsilon$ of the electroweak backgrounds are varied by $\pm 5\%$ and half the difference, 12 MeV, is taken as the systematic uncertainty.

- The PDF uncertainty is not evaluated because it is expected to be of the order of the uncertainties derived in the context of the measurements performed at TEVATRON [78], [79]. An uncertainty of 15 MeV is assigned.

- As another theoretical uncertainty, the difference between the results obtained with the NLO generator POWHEG and the LO generator PYTHIA is taken into account. It amounts to 8 MeV. This does not include uncertainties from the parton showering because the POWHEG samples are interfaced with PYTHIA for the parton showering in the simulated samples used. The agreement between the simulation and the data declines when using the PYTHIA sample instead of POWHEG. The χ^2/ndf increases by a factor of about 1.4.

A breakdown of the systematic uncertainties is given in Table 9.3.

The systematic uncertainty is dominated by the uncertainty associated with the hadronic recoil model. This result is supported by cross checks performed with the hadronic recoil distributions in W events, which suggest that all the recoil models considered in this thesis leave room for improvement. A more complex parameterization of the hadronic recoil that allows for a separate

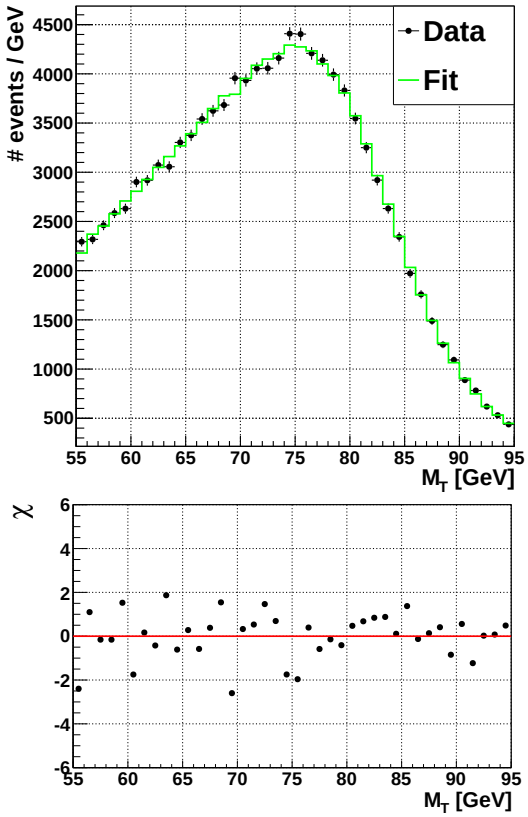

(a) Recoil model: Direct extraction.

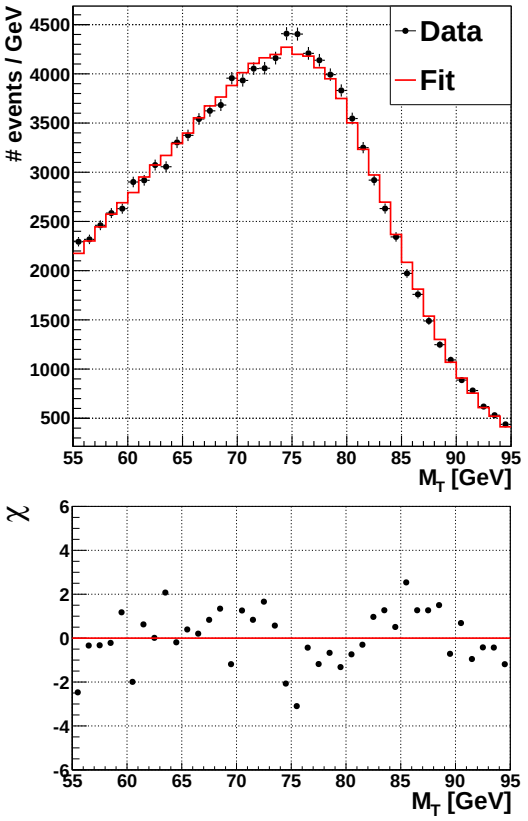

(b) Recoil model: Gaussian.

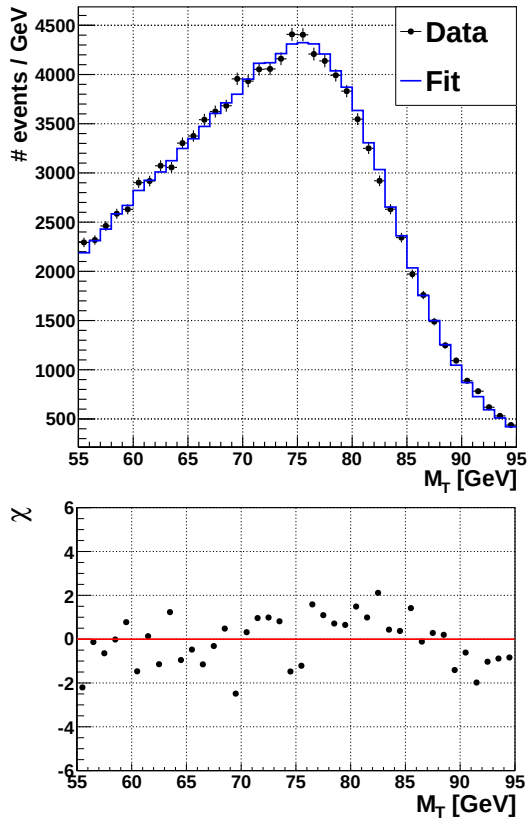

(c) Recoil model: Pileup with vertex reweighting.

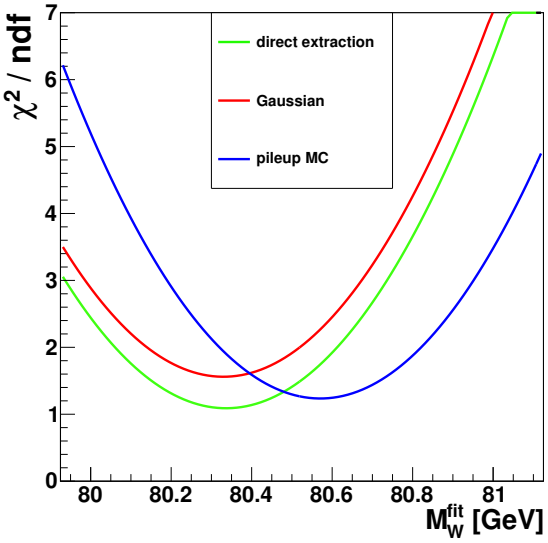

(d) χ^2/ndf comparison for the different recoil models.

Figure 9.3: (a)-(c): Best fit result for the three different recoil models. The residuals are defined as $\chi = \frac{N_{fit}-N_{data}}{\sigma_{data}}$. (d): Comparison of the χ^2/ndf parabolae for the different recoil models.

source	syst. uncertainty on M_W [MeV]
recoil model	116
muon momentum	50
M_T range	29
background	12
theory	17
total	131

Table 9.3: Breakdown of the systematic uncertainties on the W mass in MeV.

treatment of the soft and hard components in the hadronic energy would be an option. Judging from early measurements performed at the TEVATRON [80], a reduction of the recoil systematic uncertainty to the level of the uncertainty associated with the muon momentum could be feasible with the data collected by CMS in 2010.

The result of the W mass fit reads:

$$M_W = 80.426 \pm 0.046 \text{ (stat)} \pm 0.131 \text{ (syst) GeV} . \tag{9.7}$$

It is found to be in agreement with the world average of 80.399 ± 0.023 GeV [8]. The result is compared to the measurements performed at LEP [81] and TEVATRON [82] in Figure 9.4.

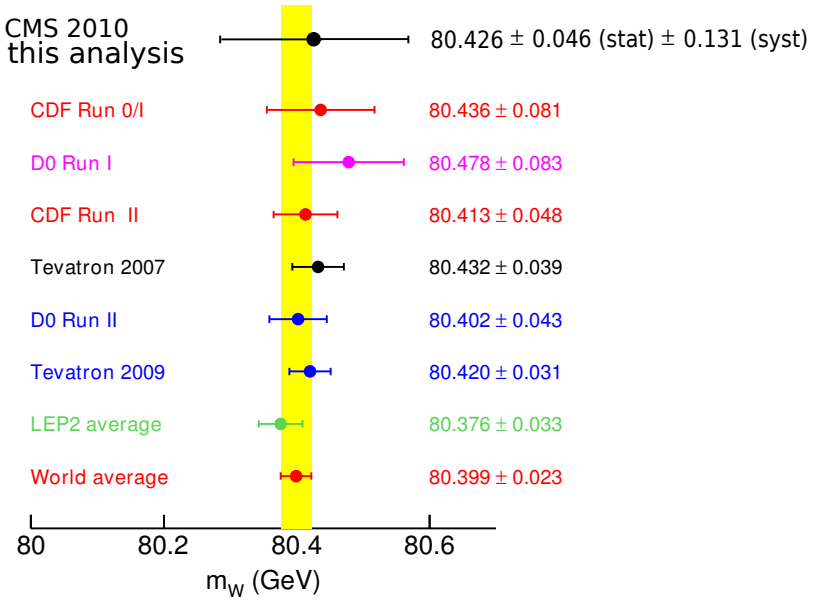

Figure 9.4: Comparison of the result of the W mass fit to the measurements dominating the world average [82].

Chapter 10

Conclusions

In the context of this thesis a measurement of the inclusive W and Z cross sections in the muon channel in proton-proton collisions at a center-of-mass energy of $\sqrt{s} = 7$ TeV has been performed. The results agree with the Standard Model predictions within the 68% confidence level of the uncertainties associated with the measurement. Furthermore, the cross section results are in agreement with the official results derived within the electroweak physics group of CMS, that are reported in [55]. The LHC is the first accelerator to reach a center-of-mass energy of $\sqrt{s} = 7$ TeV and therefore the observed agreement between theory and experiment in the vector boson production establishes an important aspect of the Standard Model in a new energy regime.
The begin of the work on this thesis coincided with the start of collision-data-taking at the LHC. In this thesis data-driven methods have been used whenever possible. The single-muon reconstruction, isolation and trigger efficiencies are determined in order to measure the W and Z cross sections, providing a test of the detector simulation. The efficiencies determined on the data are found to agree with those from simulation at the level of 1% except for the trigger efficiency which exhibits a discrepancy of about 3%. Studies of the missing transverse energy $\not\!\!E_T$ in Z events underline the importance of pileup for analyses at the LHC. The agreement between the missing transverse energy in the simulation and the data is improved by a data-driven hadronic recoil model that also allows for a determination of the W mass including the leading systematic uncertainty.
The result on the W mass of 80.426 ± 0.046 (stat) ± 0.131 (syst) GeV is consistent with the established measurements and the world average 80.399 ± 0.023 GeV [8]. However, the hadronic recoil modelling and the corresponding leading systematic uncertainty leave room for improvement. The methods employed for the determination of the W mass are suitable to set an early reference point. Neither the amount of data collected by CMS in 2010 nor the analysis methods used in this thesis do suffice to reduce the systematic uncertainty on the W mass to the level of today's most precise measurements [81, 82]. An outlook of how the systematic uncertainty on the W mass may be reduced to the level of ~ 10 MeV is given in [83, 84].

Appendix

Appendix A

Luminosity Measurement in CMS

The instantaneous (peak) luminosity $\mathcal{L}$ is a machine parameter which is defined as [23, 24]:

$$\mathcal{L} = N_1 N_2 f n_b \int dx\ dy\ \rho_1(x,y)\rho_2(x,y) \equiv \frac{N_1 N_2 f n_b}{A_{eff}}\ , \tag{A.1}$$

with the number of hadrons per bunch N_1 and N_2 in the two colliding bunches and the number of bunches n_b per beam, the orbit frequency f and the transverse beam profiles $\rho_1(x,y)$ and $\rho_2(x,y)$, which define the effective area A_{eff}. In the case of Gaussian beam profiles and assuming $\rho_1 = \rho_2$, the effective are is given by $A_{eff} = 4\pi\sigma_x\sigma_y$. For a given process with cross section σ, the event rate is given by:

$$\frac{dN}{dt} = \sigma\mathcal{L}\ . \tag{A.2}$$

Different methods are employed to measure the luminosity with the CMS detector [23]:

- The luminosity can be measured online, i.e. without a time delay between data taking and the luminosity determination. This is done with the energy towers in the HF. The average number of empty calorimeter towers per bunch crossing is used to determine the average number of interactions per bunch crossing, which depends on the luminosity. An alternative is the knowledge of the relationship between the average transverse momentum per calorimeter tower and the luminosity, which can be approximated to be linear when restricting the η range in the HF [23].

- The luminosity can be determined offline when access to the full reconstruction is available. This has the virtue of better background identification and rejection. One offline method uses the coincidence of energy deposits above 1 GeV within $|t_{HF}| < 8$ ns in the forward and backward HF. The other method is based on tracker information and the reconstruction of vertices.

All the above methods can be used to measure the time dependence of the associated signals and thus relative changes of the luminosity over time. In order to determine the absolute luminosity, the effective cross sections $\sigma_{eff} = \epsilon \cdot \sigma$ for the signals have to be known. The effective cross sections involve theoretical input and the corresponding uncertainties of 10-20% [23] have to be propagated to the absolute luminosity determination.
In order to avoid these uncertainties, a method which does not depend on theoretical input has to be employed to measure the luminosity. According to Equation A.1 the beam current of the LHC and the effective area A_{eff} at the interaction point of the CMS detector have to be measured.
Van der Meer scans [85] are carried out to determine A_{eff}. The beam profiles are parameterized (for a single Gasussian model σ_x, σ_y) and the luminosity can then be expressed as a function of a displacement of the beams in the x-z and y-z planes, Δx and Δy, and the beam profile parameters (σ_x, σ_y). Measurements of the luminosity with the HF and vertex methods as a function of known displacements Δx and Δy are carried out around the luminosity maximum $\mathcal{L}_0$ for the x and y directions separately. The beam parameters and thus the effective area A_{eff} are extracted from

a fit to the luminosity curves in Δx and Δy (Figure A.1).
The beam current measurement also includes relative measurements and measurements that provide an absolute normalization. The relative beam current measurements can be carried out bunch-by-bunch with Fast Beam Current Transformers (FBCTs) and the normalization involves a measurement of the total circulating current with DC transformers [86].
The systematic uncertainty on the absolute normalization of the luminosity dominates the uncertainty on the luminosity that has to be considered in physics analyses. The uncertainty on the luminosity has been determined to be 4% [24].

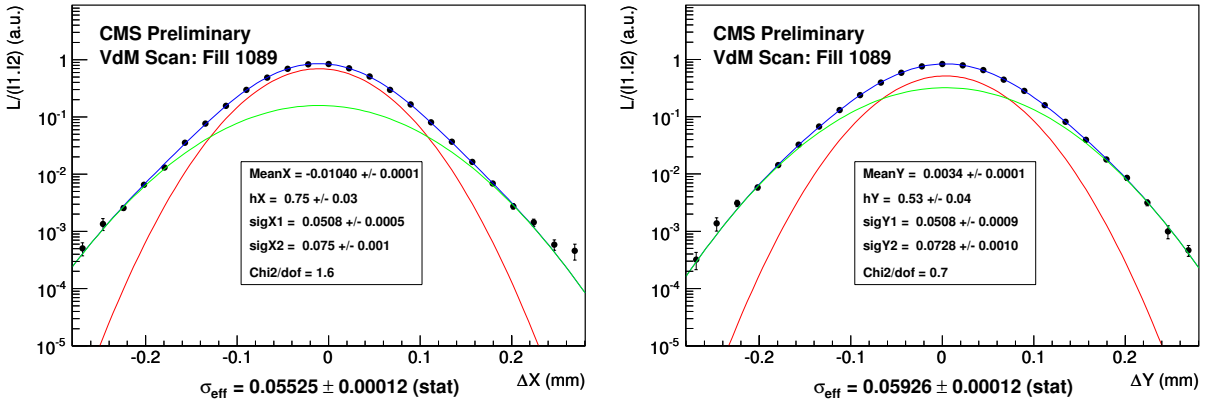

(a) Scan in x.

(b) Scan in y.

Figure A.1: Van der Meer scans in the LHC fill 1089 [23]. The beam profiles are parameterized by a sum of two Gaussians, which leads to a double-Gaussian dependence of the luminosity on Δx and Δy, respectively. The luminosity dependence on x and y is shown for the full model (blue). The contributions of the single Gaussians (red and green) are also shown.

Appendix B

Kalman Filtering

This short introduction to Kalman filtering is a summary of the corresponding chapter in [42] with some minor changes.
The task of track finding is a mapping $\boldsymbol{F}$ of all n coordinates $\boldsymbol{c}$ (including all the measurements $\{m_k\}$, $0 < k < n$) to a state vector $\boldsymbol{p}$, which includes the estimated track coordinates and the momentum at a given reference plane (for example $r = const.$, $z = const.$). [1] Most interesting for analysis is the state vector $\boldsymbol{p}$ at the origin of the interaction $\boldsymbol{p_I}$, i.e. the starting point of the track and the initial momentum vector of the particle. A good algorithm yields a mapping $\boldsymbol{F}$ without bias and with minimum variance ($\boldsymbol{p}$ is the estimated state vector, $\boldsymbol{p^t}$ is the true state vector):

$$\begin{aligned} \boldsymbol{p} &= \boldsymbol{F}(\boldsymbol{c}) && \text{(B.1)} \\ \langle \boldsymbol{p} \rangle &= \boldsymbol{p^t} && \text{(B.2)} \\ \sigma^2(\boldsymbol{p_i}) &= \langle (\boldsymbol{p_i} - \boldsymbol{p_i^t})^2 \rangle \rightarrow \min . && \text{(B.3)} \end{aligned}$$

One approach to track fitting is a global fit based on all hits associated with the track (and the corresponding uncertainties) and the Least Square Method (LSM). Algorithms based on this approach need to evaluate and invert the covariance matrix associated with the measured coordinates $\boldsymbol{c}$, which is feasible in the case of uncorrelated uncertainties (diagonal covariance matrix). If multiple scattering gives a significant contribution to the overall uncertainty, correlated errors are important and global fitting becomes complicated. The computing time for the inversion of the $n \times n$ covariance matrix scales with the number of measurements n as n^3.
When the assumption of a diagonal covariance matrix is not applicable, recursive track fitting algorithms based on the least square method (Kalman filters) are more powerful than the global approach. The recursion starts from a seed state $\boldsymbol{p_{1|1}}$ estimated from the measurements in one detector layer. The state vector at detector layer k is denoted $\boldsymbol{p_k}$. It is given by two terms. The first term is a deterministic function $\boldsymbol{f_k}$, which includes the influence of the magnetic field on the trajectory (and energy loss) and relates it to the state vector $\boldsymbol{p_{k-1}}$ in the previous detector layer. The second term introduces an additional random deviation $\boldsymbol{\delta_k}$, for example due to multiple scattering:

$$\begin{aligned} \boldsymbol{p_k} &= \boldsymbol{f_k}\left(\boldsymbol{p_{k-1}}\right) + \boldsymbol{\delta_k} \ , \ \langle \boldsymbol{\delta_k} \rangle = 0 && \text{(B.4)} \\ \boldsymbol{p_k} &\approx \boldsymbol{F_k p_{k-1}} + \boldsymbol{\delta_k} \ . && \text{(B.5)} \end{aligned}$$

This recursive equation is called the system equation or propagator. The second equation necessary for the algorithm is the measurement equation, which maps the state vectors at each detector layer

[1] In practice, the set of all measurements assigned to one track is not given when the track fitting algorithm starts. In iterative algorithms that propagate from one detector layer to the next, the next detector layer with hits likely to belong to the track segment already reconstructed has to be determined first. This process is called *navigation*. During this iterative process, several tracks sharing hits are build. This introduces ambiguities which have to be resolved based on some track quality criteria (χ^2 for example).

to the measurements $\boldsymbol{m_k}$. The uncertainty of the measurement $\boldsymbol{\epsilon_k}$ is treated seperately:

$$\begin{aligned} \boldsymbol{m_k} &= \boldsymbol{h}_k\left(\boldsymbol{p_k}\right) + \boldsymbol{\epsilon_k}\ ,\ \langle \boldsymbol{\epsilon_k} \rangle = 0 & \text{(B.6)} \\ \boldsymbol{m_k} &\approx \boldsymbol{H_k p_k} + \boldsymbol{\epsilon_k}\ . & \text{(B.7)} \end{aligned}$$

The covariance matrices of $\boldsymbol{\delta_k}$ and $\boldsymbol{\epsilon_k}$ have to be known.
The estimate of the state vector $\boldsymbol{p_k}$ in layer k can be based on different sets of measurements $\{m_1, ..., m_j\}$ (notation $\boldsymbol{p_{k|j}}$). There are three distinct cases for the state vector estimate:

1. $k > j$: prediction
2. $k = j$: filtering
3. $k < j$: smoothing

The Kalman filter works in two steps: The prediction step gives an estimate of $\boldsymbol{p_{k|k-1}}$ and its covariance matrix $\boldsymbol{C_{k|k-1}}$ based on the known estimates $\boldsymbol{p_{k-1|k-1}}$ and $\boldsymbol{C_{k-1|k-1}}$.

$$\begin{aligned} \boldsymbol{p_{k|k-1}} &= \boldsymbol{F_k p_{k-1|k-1}} & \text{(B.8)} \\ \boldsymbol{C_{k|k-1}} &= \boldsymbol{F_k C_{k-1|k-1} F_k^T} + \mathbf{cov}\left(\boldsymbol{\delta_k}\right) & \text{(B.9)} \end{aligned}$$

The second step is the filtering, i.e. building a least square estimator for the state vector $\boldsymbol{p_k}$ from the predicted $\boldsymbol{p_{k|k-1}}$ and the measurement $\boldsymbol{m_k}$ and minimizing it. The result for $\boldsymbol{p_{k|k}}$ and its covariance matrix are:

$$\begin{aligned} \boldsymbol{p_{k|k}} &= \boldsymbol{p_{k|k-1}} + \boldsymbol{K_k}\left(\boldsymbol{m_k} - \boldsymbol{H_k p_{k|k-1}}\right) & \text{(B.10)} \\ \boldsymbol{K_k} &= \boldsymbol{C_{k|k-1} H_k^T}\left(\mathrm{cov}\left(\boldsymbol{\epsilon_k}\right) + \boldsymbol{H_k C_{k|k-1} H_k^T}\right)^{-1} & \text{(B.11)} \\ \boldsymbol{C_{k|k}} &= \left(\mathbf{1} - \boldsymbol{K_k H_k}\right)\boldsymbol{C_{k|k-1}}\ . & \text{(B.12)} \end{aligned}$$

The estimate of the state vector after filtering, $\boldsymbol{p_{k|k}}$, is given by the the predicted state vector $\boldsymbol{p_{k|k-1}}$ plus an additional term that quantifies the influence of the additional measurement $\boldsymbol{m_k}$ which is now included. The Kalman filtering is based on a linear least square estimator with a χ^2 test statistic that serves as a quality parameter for a filtered track (or for a filtered state vector at a given detector layer).

After a filtering step, the previous estimates of the state vector can be refined including the information from measurements in successive detector layers. This process is called smoothing and is schematically described by the following equation:

$$\boldsymbol{p_{k|j}} = \boldsymbol{p_{k|k}} - \boldsymbol{A_k}\left(\boldsymbol{p_{k+1|k}} - \boldsymbol{p_{k+1|j}}\right)\ ,\ j > k\ . \qquad \text{(B.13)}$$

Some features of the Kalman filter with smoothing are summarized below:

- Since the track fit is decomposed into n stages, it can be used for both track fitting and track finding. The necessary seed state can be estimated from pattern recognition.
- The matrices that have to be inverted (Equation B.11) are smaller than in the case of the global fit.
- Single measurements can easily be removed from the smoothed estimate at some detector layer. This can help with the decision on hit removal and ambiguities.

Appendix C

PDF Uncertainties

This summary is based on [20].
The global fit to the data has a global minimum at $\chi^2_{min} = \chi^2_{global}\,(a^0_1, ..., a^0_n)$ with $\{a_1, ..., a_n\}$ being the set of PDF parameters. Under the assumption that χ^2_{global} is quadratic in the neighbourhood of the global minimum, the behaviour of the fit close to the global minimum is defined by the Hessian matrix H:

$$\Delta\chi^2_{global} = \chi^2_{global} - \chi^2_{min} = \sum_{i,j=1}^{n} H_{ij}\left(a_i - a^0_i\right)\left(a_j - a^0_j\right) \tag{C.1}$$

$$H_{ij} = \frac{1}{2}\frac{\partial^2\chi^2_{global}}{\partial a_i \partial a_j}|_{min}\ . \tag{C.2}$$

With the tolerance $T = \left(\Delta\chi^2_{global}\right)^{\frac{1}{2}}$ for the confidence level under consideration, the error propagation formula propagating the PDF's experimental uncertainties on an observable X takes the standard form:

$$\Delta X = T\sqrt{\sum_{i,j=1}^{n}\frac{\partial X}{\partial a_i}C_{ij}\frac{\partial X}{\partial a_j}}\ , \tag{C.3}$$

with the covariance matrix $C \equiv H^{-1}$. The PDF uncertainties on the acceptance given below correspond to a confidence level of 68%, i.e. $T = 1$.
Formula C.3 does not serve as a feasible approach to the evaluation of PDF uncertainties because the derivatives of the observable X with respect to the PDF parameters is usually not known. This problem can be overcome by a diagonalization of the covariance matrix C in the PDF parameter space. Since the covariance matrix C is symmetric, it has a set of orthonormal eigenvectors $\{\vec{v}_1, ..., \vec{v}_n\}$ with associated eigenvalues $\{\lambda_1, ..., \lambda_n\}$. Expressing the old basic set of parameters in the new set of eigenvectors yields:

$$a_i - a^0_i = \sum_{k=1}^{n}\sqrt{\lambda_k}z_k v_{ik}\ . \tag{C.4}$$

An T takes the form of a hypersphere boundary in the PDF parameter space after transformation:

$$T^2 = \Delta\chi^2_{global} = \sum_{i,j=1}^{n}\sum_{k=1}^{n}\sum_{h=1}^{n} H_{ij}z_k z_h\sqrt{\lambda_k\lambda_h}v_{ik}v_{jh} \tag{C.5}$$

$$= \sum_{h=1}^{n}\sum_{i,j=1}^{n} H_{ij}z_k^2\lambda_k v_{ik}v_{jk} \tag{C.6}$$

$$= \sum_{k=1}^{n}\sum_{i,j=1}^{n} C^{-1}_{ij}z_k^2\lambda_k\lambda_k^{-1}C_{ij} \tag{C.7}$$

$$= \sum_{k=1}^{n} z_k^2\ . \tag{C.8}$$

In addition to the central PDF S_0, n pairs of PDFs $S_k^{\pm}$ that span this hypersphere can then be built with parameter values[1]:

$$a_i(S_k^{\pm}) = a_i^0 \pm T\sqrt{\lambda_k} v_{ik} \ . \tag{C.9}$$

It can be shown that with this set of $2n$ 'error PDFs', the error propagation formula C.3 reduces to:

$$\Delta X = \frac{1}{2}\sqrt{\sum_{k=1}^{n}\left[X\left(S_k^{+}\right) - X\left(S_k^{-}\right)\right]^2} \ . \tag{C.10}$$

Alternatively, asymmetric uncertainties can be used:

$$(\Delta X)_+ = \sqrt{\sum_{k=1}^{n}\{\max[X(S_k^{+}) - X(S_0),\ X(S_k^{-}) - X(S_0),\ 0]\}^2} \tag{C.11}$$

$$(\Delta X)_- = \sqrt{\sum_{k=1}^{n}\{\max[X(S_0) - X(S_k^{+}),\ X(S_0) - X(S_k^{-}),\ 0]\}^2} \ . \tag{C.12}$$

This procedure is illustrated in Figure C.1.

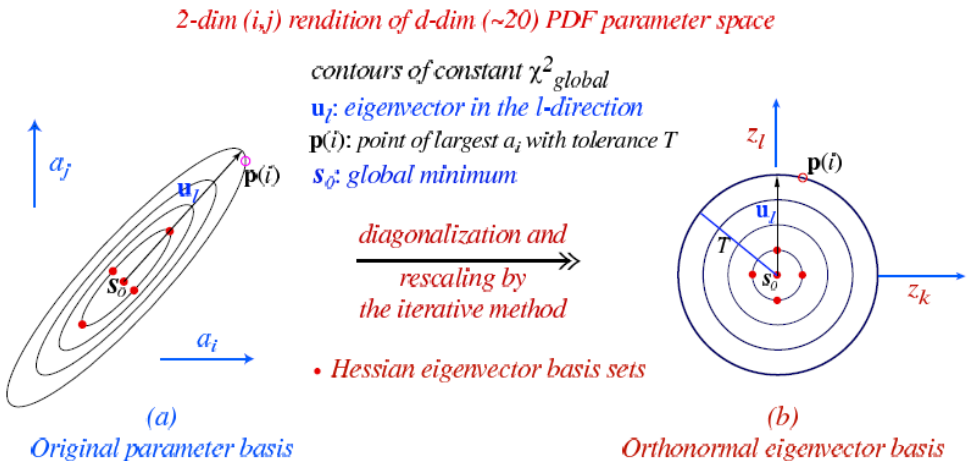

Figure C.1: Two dimensional illustration of the transformation from the basic set of PDF parameters $a_1, ..., a_n$ to the orthonormal basic set [87].

[1] In this formula the quadratic approximation is assumed for simplicity.

List of Figures

List of Tables

Bibliography

[1] A. Pich. Aspects of Quantum Chromodynamics. *arXiv:hep-ph/0001118*, 2000.

[2] S. L. Glashow. *Nucl. Phys.*, 22:579, 1961.

[3] S. Weinberg. *Phys. Rev. Lett.*, 19:1264, 1967.

[4] A. Salam. Weak and Electromagnetic Interactions. In N. Svartholm, editor, *Elementary Particle Theory, Proceedings of the 1968 Nobel Symposium*, page 367. Almquist and Wiksells, Stockholm, 1968.

[5] G. 't Hooft. *Nucl. Phys. B*, 33:173, 1971.

[6] A. Pich. The Standard Model of Electroweak Interactions. *Report CERN-2006-003, ed. R. Fleischer, arXiv:hep-ph/0502010*, 2007.

[7] R. Feynman. *Elementary Particles and the Laws of Physics, The 1986 Dirac Memorial Lectures*. Cambridge University Press, 1987.

[8] K. Nakamura et al. (Particle Data Group). *J. Phys. G*, 37, 075021, 2010.

[9] J. Goldstone. *Nuov. Cim.*, 19:154, 1961.

[10] R. K. Ellis et al. Perturbation Theory and the Parton Model in QCD. *Nucl. Phys. B*, 152: 285, 1979.

[11] V. N. Gribov and L. N. Lipatov. *Sov. J. Nucl. Phys.*, 15:438, 1972.

[12] G. Altarelli and G. Parisi. *Nucl. Phys. B*, 126:298, 1977.

[13] Yu. L. Dokshitzer. *Sov. Phys. JETP*, 46:641, 1977.

[14] A. Das. *Lectures on Quantum Field Theory*. World Scientific Publishing, 2008.

[15] P. W. Higgs. *Phys. Rev.*, 145:1156, 1966.

[16] T. W. B. Kibble. *Phys. Rev.*, 155:1554, 1967.

[17] R. K. Ellis, W. J. Stirling, and B. R. Webber. *QCD and Collider Physics*. Cambridge University Press, 1996.

[18] Q_T Resummation Portal at Michigan State University. http://hep.pa.msu.edu/resum/index.html.

[19] C.-P. Yuan C. Balázs. Soft gluon effects on lepton pairs at hadron colliders. *Phys. Rev. D*, 56:5558, 1997.

[20] A. D. Martin, W. J. Stirling, R. S. Thorne, and G. Watt. Parton distributions for the LHC. *arXiv:0901.0002v3 [hep-ph]*, 2009.

[21] MSTW PDFs: PDF benchmarking for LHC processes. http://projects.hepforge.org/mstwpdf/pdf4lhc.

[22] A. Buckley et al. General-purpose event generators for LHC physics. *arXiv:1101.2599v1 [hep-ph]*, 2011.

[23] CMS Collaboration. Measurement of CMS luminosity. *CMS PAS*, EWK-2010-004, 2010.

[24] CMS Collaboration. Absolute luminosity normalization. *CMS DPS*, 2011-002, 2011.

[25] L. Evans and P. Bryant (editors). LHC Machine. *JINST*, 3 S08001, 2008.

[26] CMS Collaboration. The CMS experiment at the CERN LHC. *JINST*, 3 S08004, 2008.

[27] ATLAS Collaboration. The ATLAS Experiment at the CERN Large Hadron Collider. *JINST*, 3 S08003, 2008.

[28] M. Spiropulu and S. Stapnes. LHC's ATLAS and CMS Detectors. In G. Kane and A. Pierce, editors, *Perspectives on LHC Physics*, page 25. World Scientific Publishing, 2008.

[29] ALICE Collaboration. The ALICE Experiment at the CERN Large Hadron Collider. *JINST*, 3 S08002, 2008.

[30] LHCb Collaboration. The LHCb Detector at the LHC. *JINST*, 3 S08005, 2008.

[31] CERN webpage, The accelerator complex. http://public.web.cern.ch/public/en/Research/AccelComplex-en.html.

[32] CMS Collaboration. The CMS Tracker System Project, Technical Design Report. *CERN-LHCC-98-006*, 1998.

[33] CMS Collaboration. The Electromagnetic Calorimeter Project, Technical Design Report. *CERN-LHCC-97-033*, 1997.

[34] CMS Collaboration. The Hadron Calorimeter Project, Technical Design Report. *CERN-LHCC-97-031*, 1997.

[35] J. Alexander. Hadronic calorimetry in CMS and ATLAS. https://wiki.lepp.cornell.edu/lepp/pub/CMS/ParticlePhysicsDetectors/hcal.pdf.

[36] CMS Collaboration. The CMS Muon Project, Technical Design Report. *CERN-LHCC-97-032*, 1997.

[37] CMS Collaboration. Performance of muon reconstruction and identification in pp collisions at $\sqrt{s} = 7$ TeV. *CMS PAS*, MUO-10-004, 2011.

[38] G. Abbiendi et al. Muon Reconstruction in the CMS Detector. *CMS Note*, 2008/097, 2009.

[39] CMS Collaboration. Performance of CMS muon reconstruction on cosmic-ray events. *JINST*, 5 T03022, 2010.

[40] CMS Collaboration. The Trigger and Data Acquisition Project, Technical Design Report. *CERN-LHCC-2000-38*, 2000.

[41] Worldwide LHC Computing Grid. http://lcg.web.cern.ch/lcg.

[42] R. Frühwirth et al. *Data Analysis Techniques for High-Energy Physics*. Cambridge University Press, 2000.

[43] CMS Collaboration. The Computing Project, Technical Design Report. *CERN-LHCC-2005-023*, 2005.

[44] CMSSW Application Framework. https://twiki.cern.ch/twiki/bin/view/CMSPublic/WorkBookCMSSWFramework.

[45] The ROOT Team. *The ROOT Users Guide*, v5.26 edition, 2007. http://root.cern.ch/drupal/content/users-guide.

[46] C. Magass et al. Aachen 3A Susy Analysis. https://twiki.cern.ch/twiki/bin/viewauth/CMS/Aachen3ASusy.

[47] Fall 2010 CMS MonteCarlo Production (7 TeV). https://twiki.cern.ch/twiki/bin/viewauth/CMS/ProductionFall2010.

[48] T. Sjostrand, S. Mrenna, and P. Skands. PYTHIA 6.4 Physics and Manual. *JHEP*, 605:26, 2006. arXiv:hep-ph/0603175v2.

[49] S. Frixione, P. Nason, and C. Oleari. Matching NLO QCD computations with Parton Shower simulations: the POWHEG method. *arXiv:0709.2092v1 [hep-ph]*, 2007.

[50] S. Frixione, P. Nason, C. Oleari, and E. Re. NLO vector-boson production matched with shower in POWHEG. *JHEP*, 807:60, 2008. arXiv:0805.4802v1 [hep-ph].

[51] GEANT4 Collaboration. GEANT4-a simulation toolkit. *Nucl. Inst. Meth. A*, 506:250, 2003.

[52] Reference cross sections at sqrt(s)=7 TeV. https://twiki.cern.ch/twiki/bin/viewauth/EWKVBTF.

[53] CMS Collaboration. Muon Identification in CMS. *CMS AN*, 2008/098, 2008.

[54] CMS Collaboration. Performance of Muon Identification in pp Collisions at $\sqrt{s} = 7$ TeV. *CMS PAS*, MUO-10-002, 2010.

[55] CMS Collaboration. Measurement of Inclusive W and Z Cross Sections in pp Collisions at $\sqrt{s} = 7$ TeV. *CMS PAS*, EWK-10-005, 2011.

[56] CMS EWK webpage. W and Z candidates with first LHC collisions at 7 TeV. https://twiki.cern.ch/twiki/bin/viewauth/CMS/WandZCandidates.

[57] CMS Collaboration. Measurement of the B+ Production Cross Section in pp Collisions at $\sqrt{s} = 7$ TeV. *Phys. Rev. Lett.*, 106:112001, 2011.

[58] CMS Collaboration. Measurement of the B0 Production Cross Section in pp Collisions at $\sqrt{s} = 7$ TeV. *arXiv:1104.2892v1 [hep-ex],CERN-PH-EP-2011-034*, 2011.

[59] C. Magass. *Bestimmung des inklusiven Wirkungsquerschnitts für Elektronproduktion bei Proton-Antiproton-Kollisionen.* Diploma thesis, RWTH Aachen University, Aachen, Germany, 2003. http://web.physik.rwth-aachen.de/~hebbeker/theses.

[60] CMS Collaboration. Measurement of the Inclusive W and Z Cross Section in *pp* Collisions at $\sqrt{s} = 7$ TeV: Update with full 2010 statistics. *CMS Note*, EWK 2010-395, 2010.

[61] W. Giele et al. The QCD/SM Working Group: Summary Report. *arXiv:hep-ph/0204316v1*, 2002.

[62] Hung-Liang et al. Lai. New parton distributions for collider physics. *Phys. Rev. D*, 82:074024, 2010.

[63] The Les Houches Accord PDF Interface. http://projects.hepforge.org/lhapdf/.

[64] H1 and ZEUS Collaborations. Combined Measurement and QCD Analysis of the Inclusive $e^{\pm}p$ Scattering Cross Sections at HERA. *JHEP*, 1001:109, 2010. arXiv:0911.0884v2 [hep-ex].

[65] G. Bauer et al. Acceptance uncertainties for inclusive W and Z cross section measurements. *CMS Note*, 2011/055, 2011.

[66] G. Cowan. *Statistical Data Analysis*. Oxford University Press, 1998.

[67] W. Verkerke and D. Kirkby. *RooFit Users Manual*, v2.07 edition, 2006. http://roofit.sourceforge.net.

[68] CMS Collaboration. Performance of Track-Corrected Missing E_T in CMS. *CMS PAS*, JME-09-010, 2009.

[69] CMS Collaboration. Jet Performance in pp Collisions at $\sqrt{s} = 7$ TeV. *CMS PAS*, JME-10-003, 2010.

[70] CMS Collaboration. Missing E_T Performance in CMS. *CMS PAS*, JME-07-001, 2007.

[71] CMS Collaboration. Particle-Flow Event Reconstruction in CMS and Performance for Jets, Taus and E_T^{miss}. *CMS PAS*, PFT-09-001, 2009.

[72] CMS Lumi Group, The official CMS Luminosity Calculation. https://twiki.cern.ch/twiki/bin/viewauth/CMS/LumiCalc.

[73] G. Bauer et al. Modeling of $W \to l\nu$ $\not\!\!E_T$ with Boson Recoil. *CMS Note*, 2010/332, 2010.

[74] M. Cepeda et al. Data Driven Methods for QCD Background Estimation in Electroweak muon analysis: the ABCD and Template methods. *CMS Note*, 2008/113, 2008.

[75] W. Adam et al. Statistics and extensions of the ABCD method for data-driven background estimates. *CMS Note*, 2009/166, 2009.

[76] CMS Collaboration. Determination of the Jet Energy Scale in CMS with pp Collisions at $\sqrt{s} = 7$ TeV. *CMS PAS*, JME-10-010, 2010.

[77] The ALEPH, DELPHI, L3, OPAL, SLD Collaborations, the LEP Electroweak Working Group, the SLD Electroweak and Heavy Flavour Groups. Precision Electroweak Measurements on the Z Resonance. *Phys. Rept.*, 427:257, 2006.

[78] D0 Collaboration. Measurement of the W Boson Mass. *Phys. Rev. Lett.*, 103:141801, 2009.

[79] CDF Collaboration. First run II measurement of the W boson mass at the Fermilab Tevatron. *Phys. Rev. Lett. D*, 77:112001, 2008.

[80] Randy Thurman-Keup. The Measurement of the Mass of the W Boson from the Tevatron. *CDF/PUB/ELECTROWEAK/PUBLIC/4676*, 1998.

[81] The LEP Collaborations: ALEPH, DELPHI, L3, OPAL and the LEP Electroweak Working Group. A Combination of Preliminary Electroweak Measurements and Constraints on the Standard Model. *arXiv:hep-ex/0612034*, 2006.

[82] Tevatron Electroweak Working Group. Updated Combination of CDF and D0 Results for the Mass of the W Boson. *arXiv:0908.1374v1 [hep-ex]*, 2009.

[83] V. Büge et al. Prospects for the precision measurement of the W mass with the CMS detector at the LHC. *CMS Note*, 2006/033, 2006.

[84] N. Besson et al. Re-evaluation of the LHC potential for the measurement of m_W. *Eur. Phys. J. C*, 57:627, 2008. arXiv:0805.2093v2 [hep-ex].

[85] S. Van der Meer. Calibration of the effective beam height in the ISR. *CERN-ISR-PO/68-31*, 1968.

[86] D. Belorhad et al. Commissioning and First Performance of the LHC Beam Current Measurement Systems. In *Proceedings of the International Particle Accelerator Conference*. MOPE059, Kyoto, 2010.

[87] J. Pumplin et al. New Generation of Parton Distributions with Uncertainties. *JHEP*, 207: 12, 2002. arXiv:hep-ph/0201195v3.

Danksagung

Zunächst möchte ich meinen Eltern danken, die durch ihre Unterstützung in jeglicher Hinsicht diese Arbeit erst ermöglicht haben.
Im Zusammenhang mit dem Entstehen der Arbeit am Institut danke ich Prof. Thomas Hebbeker für das Angebot in seiner Gruppe zu arbeiten und die Betreuung sowie die Möglichkeit, den Physikbetrieb auch außerhalb des Aachener Physikzentrums (und des Internets) auf Konferenzen und der Herbstschule in Maria Laach kennen zu lernen. Vielen Dank an Prof. Christopher Wiebusch für das Übernehmen der Zweitkorrektur.
Ein besonders herzliches Dankeschön richte ich an Carsten Magass, der für mich sowohl bezüglich der W und Z Bosonen als auch bezüglich diverser Softwarefragen meist der erste - und aufgrund sofortiger Hilfestellung häufig auch gleich der letzte - Ansprechpartner war. Für lehrreiche Unterhaltungen, Anregungen und das Korrekturlesen danke ich Arnd Meyer, Kerstin Höpfner und Markus Merschmeyer. Ganz allgemein bedanke ich mich beim gesamten Institut für die angenehme Arbeitsatmosphäre und die (u.a. im IT-Bereich) sehr guten Arbeitsbedingungen. Metin Ata danke ich für die gute Nachbarschaft und die vielseitige Unterstützung. Paul Papacz stand bei allerlei Softwareproblemen helfend zur Seite.
Ich danke der Studienstiftung des deutschen Volkes für die Unterstützung und insbesondere meinen Vertrauensdozenten Prof. Albrecht Böhm, der mich schon früh im Studium für die Teilchenphysik begeistern konnte, und Prof. Markus Morgenstern.

I would like to thank the CMS collaboration for the high-quality data delivered from day one of collision-data taking. It is truly a pleasure for a physics student to start his scientific work at the startup of such a major experiment.

Mit der Abgabe der Diplomarbeit versichere ich hiermit schriftlich, dass ich die Arbeit selbständig verfasst und keine anderen als die angegebenen Quellen und Hilfsmittel benutzt sowie Zitate kenntlich gemacht habe.

Aachen, den 31.05.2011 Andreas Güth